

MASS LOSS AND PREPROCESSING OF GALAXIES
IN GROUPS

MASS LOSS AND PREPROCESSING OF GALAXIES
TRAVERSING GROUP ENVIRONMENTS

BY GANDHALI D. JOSHI

B.A.Sc. UNIVERSITY OF WATERLOO, 2011

M.Sc. UNIVERSITY OF WATERLOO, 2013

A Thesis Submitted to the School of Graduate Studies in Partial Fulfilment of the
Requirements for the Degree Doctor of Philosophy

DOCTOR OF PHILOSOPHY (2017) McMaster University
(Physics and Astronomy) Hamilton, Ontario

TITLE: Mass Loss and Preprocessing of Galaxies Traversing Group Environments

AUTHOR: Gandhali D. Joshi

SUPERVISOR: Professor Laura C. Parker & Professor James Wadsley

NUMBER OF PAGES: xvi, [158](#)

Abstract

Groups and clusters of galaxies are environments that can significantly influence the evolution of galaxies within them. On average, as galaxies are accreted onto these structures, blue, spiral, star-forming galaxies are transformed into red, elliptical, quiescent galaxies. A number of physical environmental processes can affect the various components of galaxies and each process leaves a signature on their dark matter, gas and stellar content. Additionally, a natural result of the hierarchical growth of structure in the Universe is that more massive clusters accrete smaller groups of galaxies, which may already have exerted an environmental influence on their members. These galaxies may therefore be preprocessed in smaller groups before their final accretion. The implication of preprocessing is that some of the environmental effects attributed to clusters may in fact be established in the group environment.

In this thesis, we concentrate on the final masses and mass loss experienced by galaxies in dense environments and the degree to which they are preprocessed. Using galaxy analogues in a dark matter simulation, we investigate the phenomena of mass segregation and mass loss occurring in groups and clusters and find that tidal effects dominate their halo mass evolution. A large fraction of these galaxy analogues are preprocessed, resulting a large proportion of their total mass loss occurring *before* they are accreted by their final host haloes. We also conduct a high-resolution hydrodynamical simulation of a galaxy group to study the detailed mass loss of individual galaxies in dark matter, gas and stars. We find, again, that tidal stripping dominates the mass loss experienced by these galaxies and that it removes large amounts of dark matter and diffuse gas, while leaving most of their stellar content intact. This differential mass loss results in these galaxies having significantly different stellar mass-to-halo mass (SMHM) relations compared to field galaxies or galaxies that were accreted individually. This work stresses the important role preprocessing plays in galaxy evolution within dense environments and emphasizes the challenges of using galaxy observations containing mixed populations to constrain the effects of evolutionary mechanisms.

Acknowledgements

The last four years have been a turning point in my life and they would have gone a very different way if not for the army of people who have helped me along the way.

First and foremost, I'd like to thank my supervisors, Laura Parker and James Wadley, for their constant enthusiasm, support and patience. You were always quick to cheer when things were going well, but unwaveringly encouraging when they weren't. Thank you for always being someone I could come to for advice, not just about work, but about career and life as well. Thank you for allowing me to travel to amazing places for conferences, for giving me all of the resources I could want for and most of all, for being the best examples and role models of who a scientist should be. These last four years have been a fantastic experience thanks to you and I've learned valuable lessons working with you.

I also want to thank all my friends at Mac – Angus, Alex, Ben K., Corey, Rachel, Aaron, Rory, Kaz, Max, Tara P., Matt, Ian, Fraser, Peter, Ashley, Nathan, Sarah, Ben P., Sara, Alannah, Tara P., Tessa, Niloufar, Aisha, Jessica, Mel, Jasper and Joey (I'm so sorry if I've left someone out!) – I couldn't have asked for a better group of friends. I'm so going to miss our 'coffee' walks, GWIPA breakfasts, softball, and just random chats that would start at marking labs and invariable end with life and the meaning of it all. I'd especially like to thank Gwen and Sam – you've been like sisters to me. I've shared all our ups and downs with you and I now know I need a Sam and a Gwen at all times.

Karthik, you've been best friend and my rock for the last eleven years.

And finally to my family. Thank you to my extended family here in Canada, my aunt and uncle and cousins – you have been home for the last eleven years and my support system throughout university. And to my family in Muscat, Mom, Dad, and my sister – despite being two continents away, you have always been here for me. Mom and Dad, thank you for instilling a love of learning and for always encouraging me to reach higher. My sister and I spent many an hour chatting away – thank you for always being the same and for being my partner in crime.

CONTENTS

Abstract	iii
Acknowledgements	v
List of Figures	xii
List of Tables	xiii
List of Abbreviations	xv
Co-authorship	xvii
1 Introduction	1
1.1 Cosmological context	2
1.2 Characterizing Galaxies	6
1.2.1 Intrinsic properties	6
1.2.2 Environments	12
1.3 Galaxy Evolution	15
1.3.1 Internal processes	15
1.3.2 Environmental processes	16
1.4 Simulating the Universe	21
1.4.1 Dark matter simulations	22
1.4.2 Hydrodynamical simulations	23
1.5 Halo finding	24

1.6	This thesis	27
2	Uncovering mass segregation with galaxy analogues in dark-matter simulations	39
2.1	Introduction	41
2.2	Methods	45
2.2.1	Simulation	45
2.2.2	Halo finding	47
2.3	Mass functions	50
2.3.1	Distinct haloes	52
2.3.2	Subhaloes	55
2.3.3	Dependence on parent mass	56
2.4	Radial distributions of subhaloes	56
2.5	Galaxy analogues	59
2.6	Mass segregation	63
2.7	Discussion	68
2.7.1	Detecting substructure	68
2.7.2	Mass segregation	69
2.8	Summary	74
2.9	Appendices	79
2.9.1	MFs of subhaloes	79
2.9.2	Radial distributions of subhaloes	81
2.9.3	Radial distributions of galaxy analogues	83
3	Preprocessing, mass-loss and mass segregation of galaxies in dark-matter simulations	85
3.1	Introduction	87
3.2	Methods	90
3.2.1	Simulation	90
3.2.2	Galaxy analogues	91
3.3	Mass segregation	92
3.3.1	Comparing $M_{z=0}$ and M_{peak}	92
3.3.2	Comparing to observational results	95
3.4	The role of preprocessing	97
3.5	Discussion	105

3.5.1	Mass segregation	105
3.5.2	Preprocessing	106
3.6	Summary	108
4	The trajectories of galaxies in groups: mass loss and preprocessing	113
4.1	Introduction	115
4.2	Methods	117
4.2.1	Simulation	117
4.2.2	Halo finding and galaxy properties	121
4.3	Evolution of galaxy properties	126
4.4	Radial trajectories	132
4.5	Mass loss mechanisms	137
4.6	Implications for galaxy properties	140
4.7	Summary	143
5	Summary and future work	149
5.1	Thesis summary	150
5.2	Implications	153
5.3	Future directions	155

LIST OF FIGURES

1.1	Colour-mass diagram from Schawinski et al. (2014)	11
1.2	Examples of galaxy groups and clusters.	13
1.3	Environmental dependence of quenched fraction from Wetzel et al. (2012)	14
1.4	Schematic of galaxy analogue selection	26
1.5	Schematic of single vs. grouped galaxies	28
2.1	Comparison of large-scale structure at three resolutions	46
2.2	Comparison of halo/subhalo mass functions	53
2.3	Results of power-law fits to halo/subhalo mass functions	54
2.4	Radial distribution of subhaloes	57
2.5	Radial distributions of galaxy analogues	61
2.6	Comparison of AHF and ROCKSTAR subhalo hierarchies	62
2.7	Radial trends of average analogue mass and fractional mass	64
2.8	Radial trends of average analogue mass and fractional mass in parent mass bins	66
2.9	Mass segregation when excluding most massive analogues	70
2.10	Mass segregation when averaging over $\log M_{\text{analogue}}$	71
2.11	Comparison of AHF and ROCKSTAR halo/subhalo mass functions in parent mass bins	79
2.12	Radial distributions of subhaloes in parent halo mass bins	82
2.13	Radial distributions of galaxy analogues in parent halo mass bins	84
3.1	Average present-day mass and peak mass versus halocentric radius	93

3.2	Comparison with observed stellar mass radial trends	96
3.3	Galaxy mass loss from peak to $z = 0$ versus halocentric radius	99
3.4	Galaxy mass loss from peak to crossing and crossing to $z = 0$ versus halocentric radius	100
3.5	Galaxy mass loss since crossing versus time since crossing	102
3.6	Galaxy mass loss from peak to crossing versus time from peak to crossing	103
3.7	Mass loss of individual galaxy as a function of halocentric radius over time	107
4.1	Particle distribution and galaxy positions around the main group . . .	120
4.2	Average galaxy (physical) tidal radius as a function of time	127
4.3	Average mass of the galaxies in dark matter, gas and stars as a function of time	128
4.4	Average mass of the galaxies in cold and hot gas as a function of time	129
4.5	Average sSFRs of the galaxies as a function of time	130
4.6	Mass in dark matter, gas and stars for individual single and grouped galaxies as a function of distance from the group centre	133
4.7	Mass in dark matter, gas and stars, normalized by corresponding values at z_{peak} , for individual single and grouped galaxies as a function of distance from the group centre	134
4.8	sSFRs for individual single and grouped galaxies as a function of dis- tance from the group centre	135
4.9	sSFRs for individual single and grouped galaxies as a function of time	135
4.10	Ratio of gas mass to dark matter mass as a function of distance from the main group	138
4.11	Ram pressure acting on each galaxy as a function of distance from the main group	138
4.12	Stellar fractions of the galaxies vs. total mass	141
4.13	Gas fractions of the galaxies vs. stellar mass	142

LIST OF TABLES

2.1	Numbers of haloes identified by both halo finders	51
2.2	Results of linear fits to mass segregation trends	67
2.3	Results of power-law fits to mass functions	80
4.1	Galaxy properties for the never accreted, singly-accreted and group-accreted samples at the final redshift	124
4.2	Galaxy properties for the never accreted, singly-accreted and group-accreted samples at peak total mass	125

LIST OF ABBREVIATIONS

AGN Active galactic nucleus (nuclei)

AMR Adaptive mesh refinement

CDM Cold dark matter

FOF Friends-of-friends

ICM Intra-cluster medium

IC Initial conditions

IGM Intra-group medium

ISM Interstellar medium

LIRG Luminous Infrared Galaxy

MF Mass function

NFW Navarro-Frenk-White

SDSS Sloan Digital Sky Survey

SED Spectral energy distribution

SFR Star formation rate

SF Star forming (formation)

SMHM Stellar mass-to-halo mass

SO Spherical overdensity

SPH Smoothed particle hydrodynamics

sSFR Star formation rate

SZ Sunyaev Zel'dovich

ULIRG Ultra Luminous Infrared Galaxy

Co-authorship

Chapters 2, 3 and 4 of this thesis contain original scientific research written by myself, Gandhali D. Joshi. Chapter 2 has been published as a peer reviewed journal article in the Monthly Notices of the Royal Astronomical Society (MNRAS). The reference to this work is: *Joshi, Gandhali J., Parker, Laura C., Wadsley, James, 2016, MONTHLY NOTICES OF THE ROYAL ASTRONOMICAL SOCIETY, Volume 462, Issue 1, p. 761-777*. The work was co-authored with my co-supervisors Dr. Laura Parker and Dr. James Wadsley. Chapter 3 has also been published as a peer reviewed journal article in MNRAS. The reference to this work is: *Joshi, Gandhali J., Wadsley, James, Parker, Laura C., 2017, MONTHLY NOTICES OF THE ROYAL ASTRONOMICAL SOCIETY, Volume 468, Issue 4, p. 4625-4634*. This work was also co-authored with my co-supervisors Dr. James Wadsley and Dr. Laura Parker. Chapter 4 is in preparation and will shortly be submitted for publication in MNRAS. The author list for this work is: *Joshi, Gandhali J., Parker, Laura C., Wadsley, James W., Keller, Benjamin, W.* This work was also co-authored with my co-supervisors Dr. Laura Parker and Dr. James Wadsley. The fourth author, Dr. Ben Keller, wrote and tested the modifications made to the code MUSIC that was used to generate the initial conditions for the zoom-in simulation in Chapter 4. I hereby grant an irrevocable, non-exclusive license to McMaster University and Library and Archives Canada to reproduce the material as part of this thesis.

CHAPTER 1

INTRODUCTION

1.1 Cosmological context

Our current best model of the Universe is the Λ CDM model of cosmology. According to this model, the Universe is spatially flat and is comprised of three primary components – matter, radiation and dark energy. The matter component consists of over 80% dark matter – the invisible matter that affects the motion of all objects and the expansion of the Universe itself – with the rest being baryonic matter. The dark energy component is consistent with a cosmological constant, Λ , and is responsible for the acceleration of the expansion of the Universe. The precise proportion of the energy density contributed by each of the three components is an important factor in determining the structure of the Universe. The amount of energy contributed by each component is described by its density parameter,

$$\Omega_i(z) = \frac{\rho_i(z)}{\rho_c(z)} \quad (1.1)$$

where ρ_i is the density of the component, ρ_c is the critical density of the Universe and z is the cosmological redshift. Distances to objects in the Universe can be directly calculated using their redshifts, as can the age of the Universe when the light from that object originated. The density parameters for matter and radiation, Ω_m and Ω_r , evolve with redshift as:

$$\Omega_m(z) = \Omega_{m,0}(1+z)^3 \quad \text{and} \quad \Omega_r(z) = \Omega_{r,0}(1+z)^4 \quad (1.2)$$

while the density parameter for Λ , Ω_Λ , is a constant. Ω_m is a combination of dark matter and baryonic matter, each of which has a density parameter Ω_c and Ω_b respectively, which scales with redshift in the same manner as Ω_m . The latest results from the Planck Cosmic Microwave Background experiment find values of $\Omega_\Lambda = 0.692 \pm 0.012$, $\Omega_{m,0} = 0.308 \pm 0.012$, $\Omega_{c,0}h^2 = 0.119 \pm 0.002$, and $\Omega_{b,0}h^2 = 0.0223 \pm 0.0002$, where $h = 0.678 \pm 0.009$ is the Hubble parameter ([Planck Collaboration et al., 2016](#)). Note that in the base Λ CDM model, $\Omega_{r,0}$ is assumed to be negligible compared to $\Omega_{m,0}$ and Ω_Λ .

All conventional cosmological models assume that the Universe is homogeneous on large scales. However, had all three components been distributed perfectly uniformly in the early Universe, they would have remained uniformly distributed and no structure could have formed. Instead, there were minute fluctuations in the density

distribution in the early Universe, that were likely quantum in origin. It is theorized that they grew into macroscopic inhomogeneities during a period of rapid inflation (Guth, 1981; Linde, 1982). Such inhomogeneities in the distribution of matter formed the seeds for structure formation. They can be described at any point in space and at a given redshift as

$$\delta(\mathbf{x}, z) = \frac{\rho_{\mathbf{m}}(\mathbf{x}, z) - \bar{\rho}_{\mathbf{m}}(z)}{\bar{\rho}_{\mathbf{m}}(z)} \quad (1.3)$$

where $\bar{\rho}_{\mathbf{m}}(z)$ is the mean matter density in the Universe at the given redshift. As long as the fluctuations are small, $|\delta| \ll 1$, they can be treated as linear perturbations, i.e. fluctuations on every scale can grow independently. They can then be decomposed into fluctuations on all scales with a power spectrum of the form

$$P = A_{\mathbf{s}} k^{n_{\mathbf{s}}}. \quad (1.4)$$

where k is the wavenumber of the fluctuation, $A_{\mathbf{s}}$ is the amplitude of the fluctuations and $n_{\mathbf{s}}$ is the slope of the power spectrum. $n_{\mathbf{s}} = 1$ corresponds to a scale-invariant power spectrum such that fluctuations on all scales have equal amplitudes. The most recent values for the parameters describing the primordial power spectrum are $\ln(10^{10} A_{\mathbf{s}}) = 3.06 \pm 0.03$ and $n_{\mathbf{s}} = 0.968 \pm 0.006$ (Planck Collaboration et al., 2016). Hence, the description of the structure in the Universe as a ‘cosmic web’ is apt, since fluctuations are seen on all scales, producing objects with a wide range of masses and sizes.

The growth of density fluctuations is linear while $\delta \ll 1$. Once the fluctuations approach $\delta \sim 1$, the growth of the region can break away from the Hubble flow, undergo collapse under self-gravity and virialize, forming what is commonly called a ‘dark matter halo’, containing the dark matter and baryons associated with the region. Since the Universe is continually expanding and these haloes do not exist in isolation, their structure is never truly in equilibrium. Moreover, they also continue to grow by accreting matter. However, over the timescales for most physical processes we are interested in, these haloes can be approximated to be in equilibrium. Dark matter haloes do not have sharp edges – their matter distribution smoothly integrates with the background matter distribution. Nevertheless, we can define a ‘virial radius’ and a ‘virial mass’ based on this process of virialization. The virial theorem states that for a stable, self-gravitating system, $U = -2K$, where K is the net kinetic energy of its constituent particles and U is their potential. The virial radius r_{vir} is then the

radius within which the virial theorem holds. In practice, r_{vir} , is defined as the radius within with the average density is

$$\bar{\rho}(< r_{\text{vir}}) \geq \Delta_c(z)\rho_c(z) \quad (1.5)$$

where Δ_c is the virial overdensity. The value of Δ_c is commonly estimated from a spherical top-hat collapse model (Peebles, 1980) and can be used to identify the properties of collapsed haloes quite well. The virial mass is then the mass contained within the virial radius. The most common functional form used for $\Delta_c(z)$ is the one derived by Bryan & Norman (1998) as an empirical fit from numerical simulations:

$$\Delta_c = 18\pi^2 + 82x - 39x^2 \quad \text{where} \quad x = \frac{\Omega_{\text{m},0}(1+z)^3}{\Omega_{\text{m},0}(1+z)^3 + \Omega_\Lambda} - 1 \quad (1.6)$$

This value asymptotes to ~ 178 at high redshifts, and hence, $\Delta_c = 200$ is often used as a standard definition of virial overdensity.

The standard Λ CDM model then predicts that fluctuations on small scales will have larger amplitudes, and therefore reach $\delta \sim 1$ faster than larger scale fluctuations. Structure therefore grows in a bottom-up, hierarchical manner, where smaller objects such as galaxies collapse first, and larger objects are formed later through the coalescence of smaller structures. The characteristic mass scale of collapsing haloes evolves with redshift. One way to quantify this is through halo mass functions; the form and evolution of halo mass functions is well described by the Press-Schechter formalism (Press & Schechter, 1974). An analysis of the evolution of the halo mass function shows that the galaxy halo mass scale of $\sim 10^{11} - 10^{12}M_\odot$ is dominant at $z \sim 5-3$, the group halo mass of $\sim 10^{13}M_\odot$ scale is important at $z \sim 2-1$ and cluster sized haloes of mass $\sim 10^{14} - 10^{15}M_\odot$ are only now becoming dominant at $z \sim 0$ (e.g. see fig. 2 of Springel et al. (2005) or Mo & White (2002)). In the future, when the Universe is dominated by Λ , density fluctuations will not be able to grow resulting in a freeze-out in terms of the mass distribution of haloes, such that overdensities on large scales will never collapse. Galaxy clusters are therefore likely to be the most massive structures to virialize in the Universe.

As mentioned above, dark matter haloes do not have well defined edges and there are no discontinuities between their density distribution and the background matter density. Modelling the structure of dark matter haloes analytically is not simple.

While the formation of dark matter haloes can be approximately described by the spherical top-hat collapse model, in reality, haloes are triaxial and do not follow such a spherical collapse precisely (Bullock, 2002; Jing & Suto, 2002; Bailin & Steinmetz, 2005; Allgood et al., 2006). Haloes can also contain substructure, which means that their density profiles are not smooth or spherically symmetric. Fortunately, simulations of dark matter haloes have allowed us to determine empirical models for the structure of haloes. Perhaps the most popular of these models is the Navarro-Frenk-White (NFW) model (Navarro et al., 1996), which prescribes the following density profile for a collapsed dark matter halo:

$$\rho_{\text{NFW}}(r) = \frac{\rho_0}{\frac{r}{r_s} \left(1 + \frac{r}{r_s}\right)^2} \quad (1.7)$$

where r_s is a characteristic scale radius and ρ_0 is a normalizing central density. The corresponding mass profile, $M(r)$, diverges at large radii, but the mass within the virial radius is well constrained as:

$$M_{\text{vir}} = \frac{4\pi\rho_0 r_{\text{vir}}^3}{c^3} \left(\ln(1+c) - \frac{c}{1+c} \right) \quad (1.8)$$

where $c = r_{\text{vir}}/r_s$ is the concentration parameter. The NFW profile describes the density profiles of haloes over a wide range of masses.

So far, the growth of structure has been treated in a gravity-only manner, where most baryonic processes that drive galaxy formation have not been incorporated. However, baryonic matter has the ability to cool by radiating away energy and can therefore form dense knots, which dark matter cannot achieve (with the possible exception of the central high density cusps of dark matter haloes). These dense knots of gas can have cooling times short enough for gas to radiate away sufficient heat and condense to the point where star formation can occur and galaxy formation can begin in earnest (Rees & Ostriker, 1977; Silk, 1977). These dense regions can then become the sites for star formation and produce galaxies as we observe them. Dark matter haloes are therefore the backdrop in which galaxy evolution takes place and as the Universe evolves, larger and larger structures form and influence this evolution. The various processes that lead to star formation and the regulation of galaxy properties are discussed in Section 1.3.

1.2 Characterizing Galaxies

Galaxies can be thought of as the smallest building blocks of cosmology; they can be found on their own or as parts of larger structures, which can often be detected as overdensities in the number density of galaxies. Galaxies, as they are observed, are collections of stars, gas and dust, embedded in dark matter haloes. They can be characterized by a number of intrinsic properties as well as by their local environment.

1.2.1 Intrinsic properties

1.2.1.1 Luminosity and colour

Perhaps the most straightforward property of a galaxy to measure is its flux in broad-band filters at a variety of optical wavelengths. If the distance to the galaxy is known, then its luminosity can be calculated from this flux. The luminosity is a direct indicator of the stellar content of the galaxy. Moreover, the galaxy's colour can be obtained by comparing its flux in two distinct filters – colour is defined as the difference between the galaxy's magnitude in a bluer filter and a redder filter, such that higher colour values indicate redder galaxies. Galaxies in the Universe have a bimodal distribution in optical colours, with broadly two populations of red and blue galaxies ([Blanton et al., 2003](#); [Baldry et al., 2004](#); [Blanton & Moustakas, 2009](#)). Their colours tell us something about their current stellar populations. Blue colours indicate the presence of young massive stars that have only been in existence for 10 – 100 Myr. Red colours indicate older populations of low mass stars that are still on the main sequence, as well as post-main-sequence stars.

One complication in this simple bimodality of colours is that some galaxies that are still forming stars can appear red due to high dust content, which obscures the blue light coming from young stars. The dust is in turn heated by absorbing this light, causing it to emit light of its own at longer, i.e. redder, wavelengths. Additionally, the region in colour-space between the red and blue galaxies is not completely devoid of galaxies. These so-called green galaxies are an important third population, and whether they represent a transition between blue and red galaxies or whether they are a unique galaxy type is still a topic of research. For example, the left panel of [Fig. 1.1](#) from [Schawinski et al. \(2014\)](#) (fig. 4 in the paper) shows the colour-mass diagram of galaxies from the Sloan Digital Sky Survey (SDSS). The galaxies occupy

two distinct regions in colour-space, a distinct red sequence at higher (redder) ($u-r$) colours and a blue cloud at lower (bluer) ($u-r$) colours. The figure also shows the green valley region, indicated by the parallel green lines, which is not entirely devoid of galaxies, although it contains fewer galaxies than the two main regions. There is some evidence that such green valley galaxies are transient states for galaxies moving from the blue cloud to the red sequence (e.g. [Wetzell et al., 2013](#); [Schawinski et al., 2014](#); [Rowlands et al., 2017](#)).

1.2.1.2 Composition

Another important characteristic of galaxies is the proportion of their various components, namely dark matter, stars, gas (cold, warm and hot) and to a lesser extent, dust. The relative proportions of each of these components may be indicative of some of the evolutionary processes the galaxy has gone through, assuming that all galaxy haloes begin with the same proportion of baryons to dark matter in the early Universe.

Measuring galaxy masses is not as straightforward as measuring luminosity or colour. Stellar mass can be measured through well-calibrated relations between luminosity in a specific filter and stellar mass (e.g. [Bell & de Jong, 2001](#); [Kauffmann et al., 2003](#)). A more precise method is to observe the galaxy in multiple filters and model its stellar population to match its spectral energy distribution (SED) (e.g. [Bolzonella et al., 2000](#); [Salim et al., 2007](#); [Walcher et al., 2011](#)).

The gaseous component in a galaxy, which is predominantly composed of hydrogen, can be further subdivided into a hot halo gas component, a hot ionized interstellar medium (ISM) component, a warm ionized and warm neutral ISM component, as well as a cold atomic and cold molecular component. Each of these components requires different observational techniques and assumptions to determine their mass. For example, the hot gas component can be observed directly through X-ray emissions (e.g. [Fabbiano, 1989](#); [Civano et al., 2014](#); [Kim & Fabbiano, 2015](#)), although this is hard to do due to the low X-ray luminosities of galaxies. The neutral atomic components can be observed only through the hydrogen 21cm hyperfine transition, e.g. the ALFALFA survey ([Giovanelli et al., 2005](#)), the HIPASS survey ([Meyer et al., 2004](#)) and the THINGS survey ([Walter et al., 2008](#)). Molecular hydrogen cannot be observed directly; instead its properties are inferred by observing heavier tracer molecules, such as CO, and assuming their relative abundance compared to molecular hydrogen (e.g. [Wilson, 1995](#); [Young et al., 1995](#)).

The mass of the dark matter component is perhaps the hardest to measure observationally. One method is to use the galaxy’s kinematics to infer its mass. In general, the visible matter in a galaxy can be decomposed into a disc and a bulge component – the flattened disc component is supported against gravitational acceleration by its rotation around the galactic centre, whereas the bulge component is supported by the dispersion in the random velocities of its constituent stars and gas. For any given galaxy, one of these components will dominate over the other. The motions of the stellar material and gas is dictated by the total mass of the galaxy interior to the position of the stars and gas. For rotationally dominated galaxies, galaxy mass can be determined from their rotation curves, although measurements are limited to the radii at which the tracers can be observed. For dispersion dominated galaxies, the width of spectral absorption lines can be used to determine the galaxy’s mass (see [Binney & Tremaine, 1987](#)). However, both these techniques require resolved spectroscopic observations of the galaxy out to large radii to capture the extent of the dark matter halo. Another method to determine galaxy masses is through the use of observations of weak gravitational lensing (e.g. [Brainerd et al., 1996](#)). Although the lensing signal for individual galaxies is too weak to detect, by stacking the signal from many galaxies, their average mass profiles can be determined.

1.2.1.3 Morphology

A second broad classification of galaxies is based on their morphology. In general, galaxy morphologies can be classified as discy and spiral or spheroidal/elliptical. One of the first attempts to classify galaxies was carried out by Edwin Hubble in the 1920’s, in the classic Hubble tuning fork diagram that classifies galaxies as ‘early-type’ elliptical galaxies, to intermediate S0 galaxies, to ‘late-type’ spiral galaxies, with irregularly shaped galaxies being classified separately. Spiral galaxies are further classified based on the presence or absence of bars. While this classification is still the most popular method of characterizing galaxy morphologies, other attempts have been made to incorporate the presence of rings or to quantify morphologies. The most popular of these is fitting a Sérsic model to the intensity profile of the galaxy using algorithms such as GIM2D ([Simard et al., 2002](#)) and GALFIT ([Peng et al., 2002](#)). Other methods focus on measuring the galaxy’s concentration ([Morgan, 1958](#)) and asymmetry ([Conselice et al., 2000](#)), or the combined CAS (concentration-asymmetry-clumpiness) classification ([Conselice, 2003](#)) that also measures how smooth the light

distribution is. There is a strong correlation between morphology and colour – blue galaxies tend to be spirals while red galaxies tend to be ellipticals, although there is considerable scatter in the correlation and blue ellipticals and red spirals also exist (e.g. [Driver et al., 2007](#); [Gadotti, 2009](#); [Mahajan & Raychaudhury, 2009](#); [Wolf et al., 2009](#); [Masters et al., 2010](#); [Schawinski et al., 2014](#)). As an example, in the right panels of [Fig. 1.1](#), the galaxy sample has been separated into early-type, elliptical, galaxies and late-type, spiral galaxies. These galaxies have been given morphological classifications visually through the citizen science project Galaxy Zoo ([Lintott et al., 2008, 2011](#)). The top panel shows how early-type galaxies are almost always red with a small tail of the distribution stretching to bluer colours, while late-type galaxies are predominantly blue, although with a more widespread distribution extending to redder colours.

1.2.1.4 Star formation

The rate at which galaxies convert their cold gas content to stars is known as the star formation rate (SFR). More massive (star-forming) galaxies form stars at a higher rate than lower mass ones, forming a main-sequence of star forming galaxies ([Brinchmann et al., 2004](#); [Noeske et al., 2007](#); [Daddi et al., 2007](#); [Whitaker et al., 2012](#)). The specific star formation rate (sSFR) is the SFR normalized by the stellar mass of the galaxy and it can be used to classify its star formation status relative to the main sequence. Typically, a value of 10^{-11} yr^{-1} is used as the threshold value for this classification – galaxies with sSFRs above this threshold are classified as star-forming, while those below this value are classified as passive.

SFRs can be determined observationally through several methods. The simplest is to observe the galaxy in a UV filter and convert this luminosity into a SFR through well calibrated relations, since young O and B stars are bright in UV (e.g. [Salim et al., 2007](#); [Murphy et al., 2011](#); [Hao et al., 2011](#)). However, as mentioned above, some of this light may be obscured due to dust in the galaxy and re-emitted in the IR. Hence, adding the SFR obtained from a UV filter and a mid-IR filter (e.g. [Wu et al., 2005](#); [Calzetti et al., 2007](#); [Rieke et al., 2009](#)) can give a more complete SFR. Another method is to observe the galaxy in multiple filters and determine its SFR through SED fitting. This method requires assumptions regarding the initial stellar population and stellar evolution. The SFR can also be obtained by measuring the strength of certain emission lines in the galaxy’s spectrum such as $\text{H}\alpha$ and OII (e.g.

[Kewley et al., 2004](#); [Glazebrook et al., 2004](#); [Moustakas et al., 2006](#); [Gilbank et al., 2010](#)) – this method, while more precise in some ways, is also sensitive to dust in the galaxy and is more restrictive, since it requires greater resources.

The different methods measure different phases of star formation. For example, SFRs determined from UV luminosity measure recent star formation as they rely on young stars, while SFRs determined from mid-IR luminosity measure star formation averaged over longer timescales due to the delay before the light is reprocessed by dust. Again, there is a distinct correlation between colours, morphology and star formation status – red, elliptical galaxies tend to also be passive, while blue spiral galaxies tend to be star forming – although there are exceptions to this separation as well, as there have been observations of red star forming galaxies (e.g. see [Wolf et al., 2005](#); [Koyama et al., 2008](#); [Gallazzi et al., 2009](#); [Schawinski et al., 2014](#))

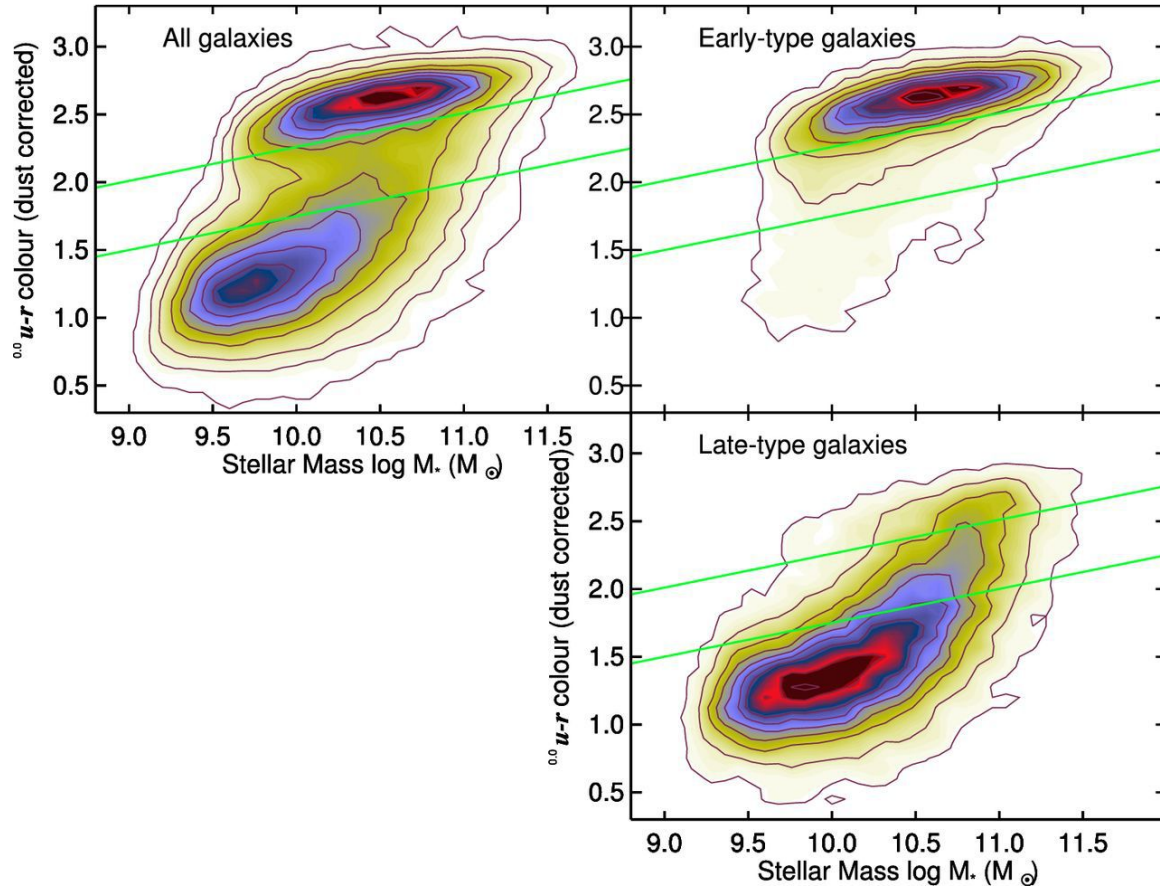


Figure 1.1: Fig. 4 of [Schawinski et al. \(2014\)](#) showing $(u-r)$ colour vs. stellar mass of SDSS galaxies. Colour has been corrected for dust reddening. Left panel shows their complete sample. Right panels show colour-mass diagram for early-type (top) and late-type (bottom) galaxies separately. Coloured regions and contoured lines show the distribution of the data. Green lines indicate the location of the green valley in the panel with all galaxies (reproduced in the other two panels).

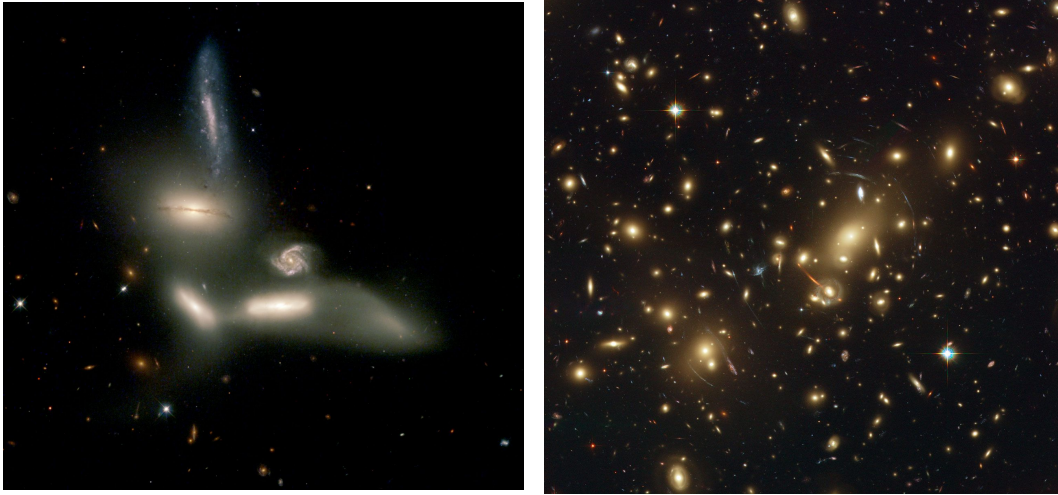
1.2.2 Environments

The environment of a galaxy is not a discretely quantifiable property, since the precise classification of environment is somewhat arbitrary. In general, galaxy environments are broadly classified as the field vs. dense structures, the latter of which can be further broken into groups and clusters. Groups and clusters are usually classified by a threshold in halo mass – clusters have halo masses of $M_{\text{halo}} \sim (10^{14} - 10^{15})M_{\odot}$ whereas groups have $M_{\text{halo}} \sim (10^{13} - 10^{14})M_{\odot}$. Fig. 1.2 shows examples of a galaxy group and a cluster. There is also no agreed upon definition for the field. In some studies, it may mean truly ‘isolated’ galaxies with a minimum distance requirement for the nearest structure, while others may include all galaxies that are not part of a group or cluster.

The Field Field galaxies are typically defined as galaxies that are found in isolated environments, not within the haloes of larger structures. The nearest galaxies to such field galaxies are sufficiently far away that they do not impose any environmental effects on the field galaxies. Hence, field galaxies are expected to evolve through internal or secular processes only. Such field galaxies live in their own dark matter haloes, which typically have masses of $\sim (10^{10} - 10^{12})M_{\odot}$.

Clusters Galaxy clusters are the largest virialized structures in the Universe and represent the other extreme in environments compared to field galaxies. They can contain hundreds to even thousands of galaxies. Such clusters have halo masses in the range of $\sim (10^{14} - 10^{15})M_{\odot}$. Due to their deep gravitational potentials, they contain a significant amount of hot, X-ray emitting gas, with temperatures of $\gtrsim 10^7 - 10^8$ K. All galaxies within the cluster therefore not only have to contend with the deep gravitational potential of the cluster and the higher number density of nearby galaxies, they also interact with the surrounding hot gas in the cluster halo, known as the intra-cluster medium (ICM). According to the hierarchical model of structure formation in the Universe, galaxy clusters represent some of the largest overdensities in the matter distribution in the Universe, and are formed through the coalescence of smaller structures such as individual galaxies or even groups of galaxies.

Groups Galaxy groups represent an intermediate environment between the field and galaxy clusters. They contain a few to a few tens of bright galaxies and have halo



(a) Interacting galaxy group, Seyfert's sextet. **Image credit:** NASA/ESA, J. English (U. Manitoba), S. Hunsberger, S. Zonak, J. Charlton, S. Gallagher (PSU), and L. Frattare (STScI)

(b) Cluster of galaxies, Abell 2218. **Image credit:** NASA, ESA, and Johan Richard (Caltech, USA). **Acknowledgement:** Davide de Martin and James Long (ESA/Hubble)

Figure 1.2: Examples of galaxy groups and clusters.

masses of $\sim (10^{13} - 10^{14})M_{\odot}$. As they have shallower potentials than clusters, they may or may not have observable amounts of hot gas, i.e. the intra-group medium (IGM). They can also have a wide range in dynamical properties with a significant proportion of groups being unrelaxed (e.g. Hou et al., 2013). Thus, galaxy groups can present a very different environment for galaxies to evolve in. Over $\sim 50\%$ of galaxies in the Universe belong to a group or a cluster (Eke et al., 2004). However, galaxy groups are difficult to detect observationally, since they require precise redshift measurements to determine group memberships, and they may or may not be detectable in the techniques used to detect massive clusters such as X-ray imaging, lensing or the Sunyaev-Zeldovich (SZ) effect.

Galaxies in dense environments have different properties on average compared to field galaxies. Group and clusters galaxies are observed to have higher fractions of quiescent galaxies, redder colours and more elliptical morphologies (e.g. Oemler, 1974; Dressler, 1980; Balogh et al., 2004; Kauffmann et al., 2004; Hogg et al., 2004; Blanton et al., 2005; Baldry et al., 2006; Wetzel et al., 2012). For example, Fig. 1.3 from (Wetzel et al., 2012) (top panel of fig. 3 in the paper) shows the fraction of SDSS

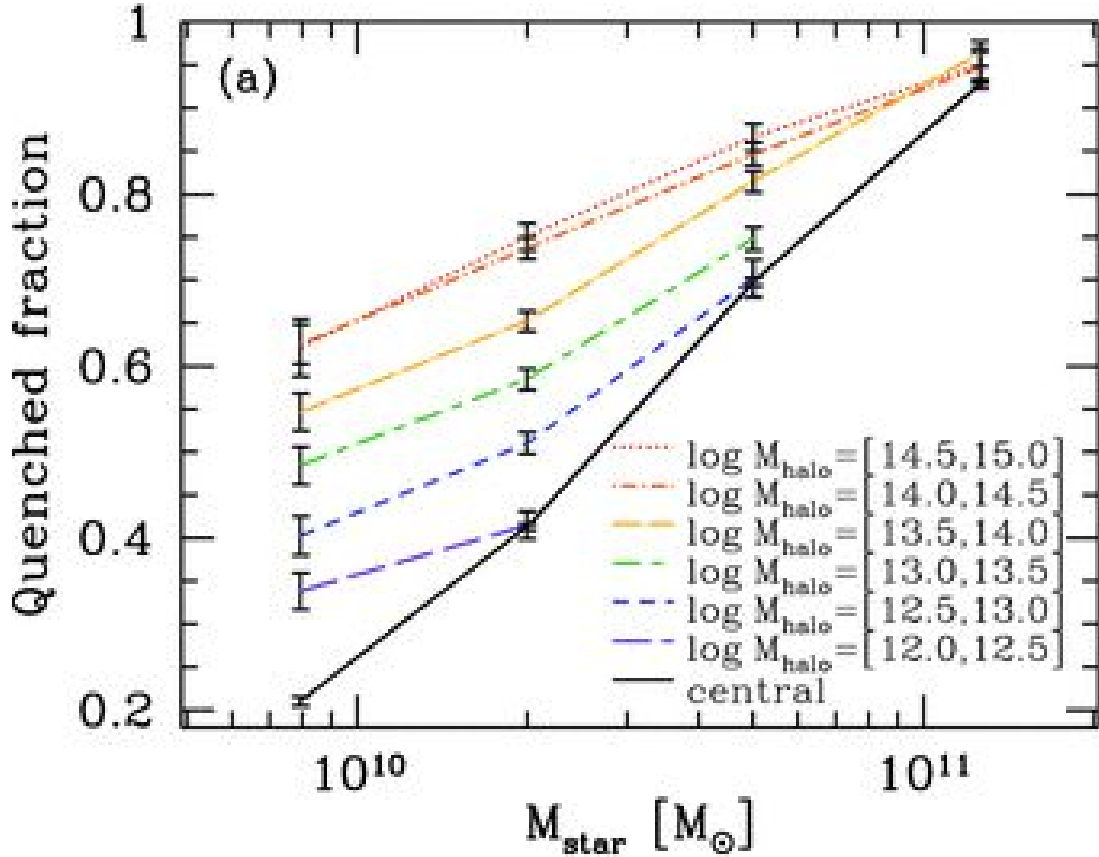


Figure 1.3: Top panel of Fig. 3 of [Wetzel et al. \(2012\)](#) showing the fraction of quenched galaxies vs. stellar mass using SDSS data. The solid black line represents central galaxies at the centres of their group/cluster halo, while coloured lines show satellite populations in bins of host halo mass.

galaxies that are quenched as a function of their stellar mass. Quenched galaxies are galaxies with drastically reduced sSFRs, as mentioned above; the term ‘quenched’ may sometimes imply that the transformation from star-forming to passive was via a rapid process, but the term ‘quenched’ is often used interchangeably with ‘passive’ or ‘quiescent’. The black solid line shows the sample of ‘central’ galaxies that are at the centres of their host haloes, while the coloured lines show satellite populations in bins of host halo mass. For galaxies with lower stellar masses, the quenched fraction varies significantly with environment, with galaxies in denser environments more likely to be quenched. On the other hand, the quenched fraction is highest for the most massive galaxies and shows almost no variation with environment.

1.3 Galaxy Evolution

1.3.1 Internal processes

Several internal processes within galaxies can regulate their properties as the galaxy evolves. Each process affects the balance of material flowing into and out of a given state, particularly the conversion of gas from hot to cold and star forming or vice versa.

1.3.1.1 Star formation

Over time, gas within a galaxy will cool by radiating away energy and form denser and denser regions. This cold gas can eventually cool to form molecular clouds that are dense enough to form stars. As star formation continues, it depletes the galaxy of its gas, gradually transforming the galaxy from blue, star-forming to red and passive. The rate at which a galaxy forms stars can have a significant impact on the galaxy's properties. Additionally, star formation can be significantly affected by external processes, as discussed below, which can either heat star forming gas or remove it completely from the galaxy. Star formation can only continue if there is a continual supply of gas to replenish the gas lost due to these processes. Additionally, the overall star formation rate density in the Universe rises steadily at early times, peaking at $z \sim 2$, followed by a steady decline to $z = 0$ as shown by the Lilly-Madau plot (Lilly et al., 1996; Madau et al., 1996, 1998; Schiminovich et al., 2005; Madau & Dickinson, 2014).

1.3.1.2 Stellar feedback from winds and supernovae

The stars forming in galaxies can have a wide range of masses, which is the key property that determines their fate. Massive stars have short lifespans of $\sim 10 - 100$ Myr, ending in violent supernova explosions. Additionally, throughout their lifetime, stars eject material in the form of stellar winds that serve to heat the surrounding ISM. In the past few decades, it has become clear that these supernovae and stellar winds have a large impact on the ISM within the galaxy. Specifically, the energy released in these supernovae can prevent star formation in the surrounding regions. The precise method by which this occurs, whether it is through radiatively heating the gas that would have formed stars, or mechanical heating, or other processes,

is not yet resolved. However, several studies have examined the effects of stellar feedback on galaxies and found that stellar feedback is important for regulating star formation rates and the formation of disc dominated galaxies, especially for galaxies with $M_{\text{halo}} \lesssim 10^{12} M_{\odot}$ (e.g. [White & Frenk, 1991](#); [Okamoto et al., 2005](#); [Governato et al., 2007](#); [Dalla Vecchia & Schaye, 2008](#); [Keller et al., 2016](#)).

1.3.1.3 Active Galactic Nuclei (AGN)

For more massive galaxies, another important and perhaps dominant mechanism for regulating galaxy properties is the presence of an active galactic nucleus (AGN), which is the supermassive black hole (SMBH) at the centre of the galaxy actively accreting material from the surrounding accretion disc, and in the process, releasing large amounts of energy in the form of jets. These jets can also serve to prevent star formation by heating the surrounding gas and stopping it from reaching the temperature and density it needs to form stars; this is especially important for galaxies with $M_{\text{halo}} \gtrsim 10^{12} M_{\odot}$ (e.g. [Fabian, 2012](#); [Dubois et al., 2013](#); [Cicone et al., 2014](#); [Le Brun et al., 2014](#); [Keller et al., 2016](#)). Modelling AGN feedback is made difficult by the fact that it is propagated by collimated jets that are highly directional. Additionally, the process powering AGN feedback, i.e. accretion by the central SMBH, occurs on the scale of a few A.U., and yet the jets affect the global properties of galaxies extending to 100's of kiloparsecs. This makes simulating AGN feedback challenging and often involves subgrid recipes, i.e. numerical prescriptions for calculating various properties that cannot directly be resolved in the simulation (e.g. [Hopkins & Hernquist, 2006](#); [Croton et al., 2006](#); [Scannapieco et al., 2012](#)).

1.3.2 Environmental processes

Apart from the internal processes mentioned above, the environment the galaxies live in has a large impact on their properties. As described above, galaxies can live in a wide range of environments – from isolated regions containing a single galaxy, to small numbers of galaxies interacting with each other but with each of them contained within a separate dark matter halo, to groups and clusters of galaxies sharing a massive common dark matter halo. There are several categories of interactions that can occur in such environments. In dense environments like groups and clusters, the galaxies have more frequent interactions with other galaxies due to their higher

number densities. The deeper gravitational potential of the group or cluster can also impact the composition of galaxies. Processes such as mergers, tidal effects, harassment and dynamical friction fall under this category. Additionally, the IGM or ICM can also hydrodynamically interact with the galaxies through processes such as ram pressure stripping and strangulation. Each of these processes detailed here can impact the galaxies' immediate and future properties.

1.3.2.1 Gravitational processes

Mergers Due to the higher occurrence of galaxies in close proximity, galaxy mergers are more frequent in groups and clusters (Lacey & Cole, 1993; Kauffmann et al., 1993; Makino & Hut, 1997). Mergers can be characterized by the ratio of the masses of the participating galaxies – major mergers involve galaxies of similar mass whereas minor mergers involve two galaxies of significantly different masses, sometimes differing by over an order of magnitude. Depending on the merger ratio, either one or both participating galaxies may undergo significant changes in morphology as well as SFR. Minor mergers tend to disturb the morphology of the more massive galaxy (e.g. Springel & Hernquist, 2005; Hopkins et al., 2009) and perhaps induce a burst of star formation, while the smaller galaxy is often completely disrupted and incorporated into the larger galaxy. Major mergers on the other hand can significantly change the morphology of the participating galaxies, often converting the ordered structure of spiral disc galaxies to more spheroidal, dispersion-supported galaxies (Toomre, 1977; Barnes, 1992). In the process, they can drive gas to high densities and thus induce large starbursts which can rapidly consume the gas with the galaxy, thus making it unavailable for future star formation (Barnes & Hernquist, 1991; Mihos & Hernquist, 1994, 1996; Elbaz & Cesarsky, 2003; Hopkins et al., 2006). Such starbursting galaxies can be observed as Luminous Infra-Red Galaxies (LIRGs) or Ultra-Luminous Infra-Red Galaxies (ULIRGs). The end result of such interactions is that galaxy populations slowly change from more star forming, blue, spiral galaxies to more quiescent, red, elliptical ones.

Harassment Harassment is another galaxy-galaxy interaction that occurs at high approach velocities between the two galaxies. Rather than coming in contact with each other directly, these high-speed encounters lead to an increase in the galaxies' velocity dispersions, making their mass less bound and therefore more easily removed

from the galaxy (Moore et al., 1996, 1998). While the effects of harassment may not immediately be detectable, they may contribute in the long term to the galaxies' evolution in the group or cluster. Recent studies have examined the effects of harassment and have generally found that galaxy harassment may not be an important factor in driving observed environmental trends in galaxies (e.g. Tanaka et al., 2004; van den Bosch et al., 2008; Weinmann et al., 2009; Smith et al., 2015).

Tidal Effects Due to the deeper gravitational potential of the group or cluster environment, galaxies in these structures face competition in terms of being able to retain their own mass, let alone being able to accrete more mass as they would in the field. This differential gravitational force due to the galaxy's own halo and the group/cluster's halo serves to remove mass that is less bound to the galaxy and more bound to the group/cluster itself, usually from the outskirts of the galaxy (Toomre & Toomre, 1972; Barnes & Hernquist, 1992; Bournaud et al., 2004). The tidal radius r_{tid} for a satellite around a host should satisfy the condition that

$$\frac{GM_{\text{sat}}(< r_{\text{tid}})}{r_{\text{tid}}^2} = \frac{GM_{\text{host}}(< (d - r_{\text{tid}}))}{(d - r_{\text{tid}})^2} - \frac{GM_{\text{host}}(< d)}{d^2} \quad (1.9)$$

where d is the distance between the satellite and host centres, and M_{sat} and M_{host} are their masses enclosed within the given radius respectively. Assuming that $r_{\text{tid}} \ll d$ and $M_{\text{host}}(< (d - r_{\text{tid}})) \approx M_{\text{host}}(< d)$, this condition can be approximated as:

$$\rho_{\text{sat}}(< r_{\text{tid}}) \approx 2\rho_{\text{host}}(< d) \quad (1.10)$$

We can estimate the distance d at which the satellite should begin to be affected by the host by setting $r_{\text{tid}} = r_{\text{vir,sat}}$, whereby

$$\rho_{\text{sat}}(< r_{\text{tid}}) = \Delta_c \rho_c \quad (1.11)$$

For the host halo, assuming an NFW profile and using eqs. 1.7 and 1.8, the density of the host can be determined as

$$\rho_{\text{host}}(< d) = \frac{\Delta_c \rho_c}{x^3} \left(\frac{\ln(1 + xc) - \frac{xc}{1+xc}}{\ln(1 + c) - \frac{c}{1+c}} \right) \quad (1.12)$$

where c is the concentration parameter for the host halo and $x = d/r_{\text{vir,host}}$. The value of x can be determined by combining eqs. 1.10, 1.11 and 1.12 – for a wide range of values for $c = [1, 50]$, $x \approx 1.3 - 1.5$. This approximation implies that the host can begin tidally stripping the satellite before it enters the virial radius of the host.

As tidal stripping removes mass from the outside in, it is more likely to remove dark matter and hot gas from the galaxy first, and only then reach the colder gas and stars (e.g. [Smith et al., 2016](#)). A crude estimate of the position of the satellite when its tidal radius is a given fraction of its virial radius can also be estimated. Assuming a concentration parameter of 10 for both the satellite and the host, for $r_{\text{tid}} = 0.5 r_{\text{vir,sat}}$, $x \approx 0.8$, while for $r_{\text{tid}} = 0.1 r_{\text{vir,sat}}$, $x \approx 0.2$. Note also that this approximation assumes that $M_{\text{host}}(< (d - r_{\text{tid}})) \approx M_{\text{host}}(< d)$, which does not hold close to the centre of the host halo. Thus, the satellite must be very close to the centre of the host halo before any stellar content can be stripped.

Dynamical Friction There are also additional processes that do not directly affect the galaxies themselves, but affect their positions within the group or cluster, such as dynamical friction. First proposed by [Chandrasekhar \(1943\)](#), dynamical friction is the drag force generated by the gravitational forces from a cloud of objects as the galaxy travels through them, that gradually drives the galaxy towards the centre of the group/cluster halo. The acceleration caused by dynamical friction on a body of mass M travelling with a velocity of \mathbf{v}_M through a distribution of particles of mass m_a , where $m_a \ll M$, can be estimated as follows (e.g. see [Binney & Tremaine, 1987](#)):

$$\frac{d\mathbf{v}_M}{dt} = -16\pi^2 G^2 M m_a \ln \Lambda \left[\int_0^{v_M} dv_a v_a^2 f(v_a) \right] \frac{\mathbf{v}_M}{v_M^3} \quad (1.13)$$

Here, $f(v_a)$ is the distribution of speeds of the surrounding particles and the factor Λ is approximated as:

$$\Lambda \approx \frac{b_{\text{max}} v_{\text{typ}}^2}{GM} \quad (1.14)$$

where b_{max} is the largest impact parameter between a particle and the body and v_{typ} is a typical velocity for the body within the group/cluster. For sufficiently large values of \mathbf{v}_M , as are typical in groups and clusters, the equation reduces to

$$\frac{d\mathbf{v}_M}{dt} = -4\pi^2 G^2 M m_a n \ln \Lambda \frac{\mathbf{v}_M}{v_M^3} \quad (1.15)$$

where n is the number density of the particles. The dynamical friction force therefore scales as

$$F_{drag} \propto \frac{M^2 \rho}{v_M^2} \quad (1.16)$$

where ρ is the density within the host halo. Thus the dynamical friction force is expected to depend on the ratio of the mass of the satellite and the mass of its host halo. While dynamical friction does not affect the galaxies' internal structure, their positions in the group/cluster halo can make them more or less susceptible to the other environmental processes (Ostriker & Tremaine, 1975; Tremaine et al., 1975; White, 1977).

Another important factor is the timescale on which dynamical friction can affect galaxies. The timescale on which a satellite might sink to the centre of a host halo due to dynamical friction is given by:

$$\tau_{df} = 1.17 \frac{r_{circ}^2 V_{circ}}{GM \ln(Nm/M)} \epsilon^\alpha \quad (1.17)$$

where V_{circ} is the circular velocity of the satellite, r_{circ} is the radius of a circular orbit with the same orbital energy as the actual orbit of the satellite, N is total number of surrounding particles, and ϵ is the circularity of the satellite's orbit, defined as the ratio of the angular momentum of its orbit to that of a circular orbit having the same orbital energy (Binney & Tremaine, 1987; Lacey & Cole, 1993). Numerical studies have found values of $\alpha \approx 0.4$ (e.g. Colpi et al., 1999). More recent studies have found that this equation underestimates the merger timescales using simulations and semi-analytical modelling (e.g. see Jiang et al., 2008; Boylan-Kolchin et al., 2008; Gan et al., 2010). Whether dynamical friction is an important factor in groups and clusters is an ongoing topic of debate.

1.3.2.2 Hydrodynamical processes

Ram Pressure Stripping As groups and clusters contain a significant amount of hot gas forming the IGM or ICM respectively, group/cluster galaxies also interact with this medium hydrodynamically. The IGM/ICM can strip even the tightly bound cold gas from galaxies through the process of ram pressure stripping (Gunn & Gott, 1972; Abadi et al., 1999). The magnitude of ram pressure experienced by a galaxy depends on the density of the surrounding medium, ρ_{med} , and velocity of the galaxy

relative to the medium, v , as:

$$P_{\text{ram}} = \rho_{\text{med}} v^2 \quad (1.18)$$

Ram pressure stripping results in the galaxy rapidly losing its cold gas, which is the immediate fuel for star formation. Hence, this process leads to rapid mass loss and star formation quenching. Several recent studies have examined the role of ram pressure stripping and found that it is an important evolutionary mechanism for galaxy evolution in groups and clusters (e.g. [Mayer et al., 2006](#); [Font et al., 2008](#); [McCarthy et al., 2008](#))

Starvation Starvation is a milder form of ram pressure stripping in that it is also due to the interaction between the galaxy’s gas content and the surrounding medium, but only results in the removal of the hot gas reservoir, which would otherwise have cooled in the future and eventually formed stars. Thus, the immediate effect of strangulation is only the loss of hot gas, while its effects are felt later as the galaxy’s SFR declines in the absence of a continuous supply of cold gas ([Larson et al., 1980](#); [Balogh et al., 2000](#); [Kawata & Mulchaey, 2008](#)).

1.4 Simulating the Universe

One major hurdle in understanding galaxy evolution through observations is the fact that it occurs over large timescales, too large for us to follow an individual galaxy as it evolves. Instead, galaxies are observed at varying epochs and their evolution is inferred under the assumption that we can connect populations of galaxies as following the same evolutionary paths. Simulations or semi-analytical modelling can circumvent this problem by allowing us to follow not only individual galaxies, but even individual particles within the galaxies, in order to directly measure their evolution. Simulations come with their own limitations. They are constrained by computational resources, which restrict the spatial resolution that can be obtained from them. The amount of computational resources required does not scale linearly with resolution and hence, achieving a higher spatial resolution requires additional efforts to increase efficiency. In turn, the resolution that can be attained restricts the physics that can be probed by the simulation.

1.4.1 Dark matter simulations

Conducting full hydrodynamical simulations is computationally very expensive. The first cosmological simulations however were not hydrodynamical but N-body simulations of the dark matter alone (e.g. [Holmberg, 1941](#); [von Hoerner, 1960](#); [Aarseth, 1963](#)). These have the advantage that they are only driven by gravitational forces and therefore, require much less computation. Despite this fact, calculating gravity scales as N^2 with the number of particles in the simulation, which quickly becomes restrictive for high resolutions. Therefore, significant advancements have been made in developing approximate methods, notably in developing tree codes, where particles that are farther away can be treated as a single aggregate, thereby reducing the number of calculations that are required at each step.

A lot can be learned from dark-matter only simulations. Since most of the matter in the Universe is composed of dark matter, the growth of structure is dominated by the behaviour of dark matter, and therefore, such simulations can predict the populations and distributions of the haloes of galaxies, groups and clusters even in the absence of baryons. There have been several large cosmological dark-matter simulations that have helped shed light on structure formation. Notable among these are the Millennium project ([Springel, 2005](#); [Boylan-Kolchin et al., 2009](#)) and the Bolshoi simulation ([Klypin et al., 2011](#)). The first Millennium simulation consisted of a $(500 h^{-1}\text{Mpc})^3$ volume containing $\sim 10^{10}$ particles, each with a particle mass of $8.6 \times 10^8 h^{-1}M_{\odot}$, run using the code GADGET-2 ([Springel, 2005](#)). This was followed by the higher-resolution Millennium II simulation ([Boylan-Kolchin et al., 2009](#)), which consisted of a $(500 h^{-1}\text{Mpc})^3$ with the same number of particles, resulting in a particle mass of $6.9 \times 10^6 h^{-1}M_{\odot}$. The Bolshoi simulation consists of a $(250 h^{-1}\text{Mpc})^3$ volume containing $\sim 8.6 \times 10^9$ particles, each with a particle mass of $1.4 \times 10^8 h^{-1}M_{\odot}$. Such large volumes are required in order to overcome the constraints of cosmic variance, i.e. the variance in the distribution of structure in the Universe, and obtain statistically meaningful samples of massive haloes. For example, at present, the number density of the massive clusters with $M_{\text{halo}} \sim 10^{15}M_{\odot}$ is on the order of 10^{-6}Mpc^{-3} ([Mo & White, 2002](#)), which means that a volume of $(100 \text{Mpc})^3$ will contain a few of these massive clusters.

Such dark matter simulations allow us to probe structure formation in the Universe, such as the collapse of haloes, their evolution in terms of mass, size and shape and density profiles, merger histories and gravitational interactions including the en-

vironmental processes discussed in Chapter 1. However, the absence of any baryonic physics means that in order to connect these simulations to galaxies, several assumptions have to be made. These can be in the form of direct stellar mass-to-halo mass relations e.g. from [Behroozi et al. \(2013b\)](#) or [Hudson et al. \(2015\)](#), or in the form of semi-analytical modelling with the use of approximate analytical recipes for several physical processes that can be used in conjunction with dark matter haloes to predict the behaviour of galaxies within the haloes. Several assumptions have to be made in applying either of these methods. Additionally, recent work has found that baryonic physics is crucial to simulating galaxies, not only for understanding the behaviour of gas and stars, but also because the baryons can have a measurable effect on the dark matter haloes they inhabit (e.g. [Peñarrubia et al., 2012](#); [Brooks et al., 2013](#); [Sawala et al., 2016](#)).

1.4.2 Hydrodynamical simulations

The limitations of dark matter simulations and semi-analytical modelling can be partially overcome through full hydrodynamical simulations that incorporate all the key baryonic physics processes, although they use several subgrid recipes which require their own assumptions. While they are much more computationally expensive, they allow us to apply known physics and directly study the gaseous and stellar components of galaxies, groups and clusters.

Several research groups have developed sophisticated codes to carry out hydrodynamical simulations, each deploying a variety of physics modules. At a minimum, these codes numerically solve the fundamental equations of fluid dynamics, impose cooling through radiating away heat energy, and apply a recipe for star formation. In addition to these, codes may also involve more complicated stellar winds and feedback from supernovae, follow several metal species, and sometimes even incorporate the formation of black holes and feedback from AGN. These feedback processes are crucial for the regulation of star formation in simulated galaxies, as well as for shaping their morphologies so that they match the properties of observed galaxies. Note that each of these processes occurs well below the resolution limit of current galaxy-scale (and higher) simulations. They are therefore not directly simulated, but approximated through detailed sub-grid physics.

Galaxy simulations can broadly be separated into those that focus on isolated, single galaxies that are highly-resolved, and those that focus on large cosmological

volumes where large scale effects are accounted for, but the galaxies themselves may not be well resolved. One method to bridge these two approaches is to carry out zoom-in simulations, where a small region within a larger cosmological volume is simulated with higher resolution, while the surrounding volume can still affect the high-resolution region without us having to expend effort in simulating it in detail. Of the simulations focusing on individual galaxies, the notable recent projects are the GIMIC (Schaye et al., 2010), FIRE (Hopkins et al., 2014), APOSTLE (Sawala et al., 2016) and MUGS2 (Keller et al., 2016) projects. Recent hydrodynamical simulations of large cosmological volumes and zoom-in regions containing group and cluster scale structures include OWLS (Crain et al., 2009), EAGLE (Crain et al., 2015; Schaye et al., 2015), ILLUSTRIS (Vogelsberger et al., 2014) and ROMULUS (Tremmel et al., 2017). Each of these simulations incorporate some form of supernova feedback. APOSTLE, EAGLE, ILLUSTRIS and ROMULUS also employ AGN feedback. MUGS2 was run using GASOLINE2 (Wadsley et al., 2017), which is an SPH, hydrodynamic code that includes an improved prescription for superbubble feedback from supernovae (Keller et al., 2014).

1.5 Halo finding

One important step in analysing the results of simulations is defining either dark matter haloes in an N-body simulation, or galaxies as well as groups and clusters in a hydrodynamical simulation. In particular, when studying groups and clusters which are high density environments, being able to identify separate structures as an additional overdensity compared to the overall halo of the group or cluster becomes a difficult task.

Several groups have studied the ideal method to identify haloes in simulations. These methods can broadly be separated into two categories of algorithms: a) spherical overdensities (SO) algorithms that locate regions of higher density in the matter distribution, and define dark matter haloes based on their density contrast, in spherical regions around the halo centre compared with the background density, and b) friends-of-friends (FOF) algorithms that connect individual particles to each other if they are closer than a specified linking length. Each of these algorithms can be carried out iteratively with stricter criteria – higher refinement criteria for SO algorithms or tighter linking lengths for FOF algorithms – to centre in on density peaks, and in the

process, generate a hierarchy of structures. Along with spatial information, several algorithms also use the velocities of particles or cells to improve their ability to differentiate between haloes, especially in high density environments where haloes may overlap, but their member particles have distinct velocity distributions, e.g. in the case of recent mergers. Some halo finders even specialize in detecting substructures and sometimes several levels of substructure. Popular SO halo finders include BOUND DENSITY MAXIMA (BDM) (Klypin & Holtzman, 1997), SUBFIND (Springel et al., 2001) and the AMIGA HALO FINDER (AHF) (Knollmann & Knebe, 2009). FOF halo finders include HIERARCHICAL FOF (Gottlöber et al., 1999), PARALLEL FOF (Rasera et al., 2010), 6DFOF (Diemand et al., 2006) and ROCKSTAR (Behroozi et al., 2013a) (these last two are phase-space algorithms, i.e. they use both spatial and velocity information). The precise algorithm used can have a significant effect on the population of galaxies recovered as well as how well the galaxies can be tracked over time.

Galaxy Analogues In Chapters 2 and 3, we use a dark matter simulation of a large cosmological volume. When analysing dark matter simulations, a key step is determining which of the dark matter haloes identified by a halo finder represent galaxies and which represent groups and clusters. This is especially difficult when the halo finder identifies several levels of subhalo hierarchy. Often, the approach taken is to use haloes within a certain mass range, or use all haloes that are hosted by another halo. In practice, this leads to the selection of multiple (sub)haloes that may represent a single galaxy on the one hand, or a halo that may represent a few galaxies. Since we are interested in ‘galaxies’ within groups and clusters, we developed a simple set of criteria to explore the entire subhalo hierarchy and only retain those haloes that represented a single galaxy. Fig. 1.4 shows a schematic of the criteria, which are explained in detail in Chapter 2. In short, we first apply mass limits to select candidate galaxy analogues. Then, starting with the distinct halo at the top of the subhalo hierarchy, we explore its subhaloes, subsubhaloes etc. and keep those haloes that are likely to host a single galaxy.

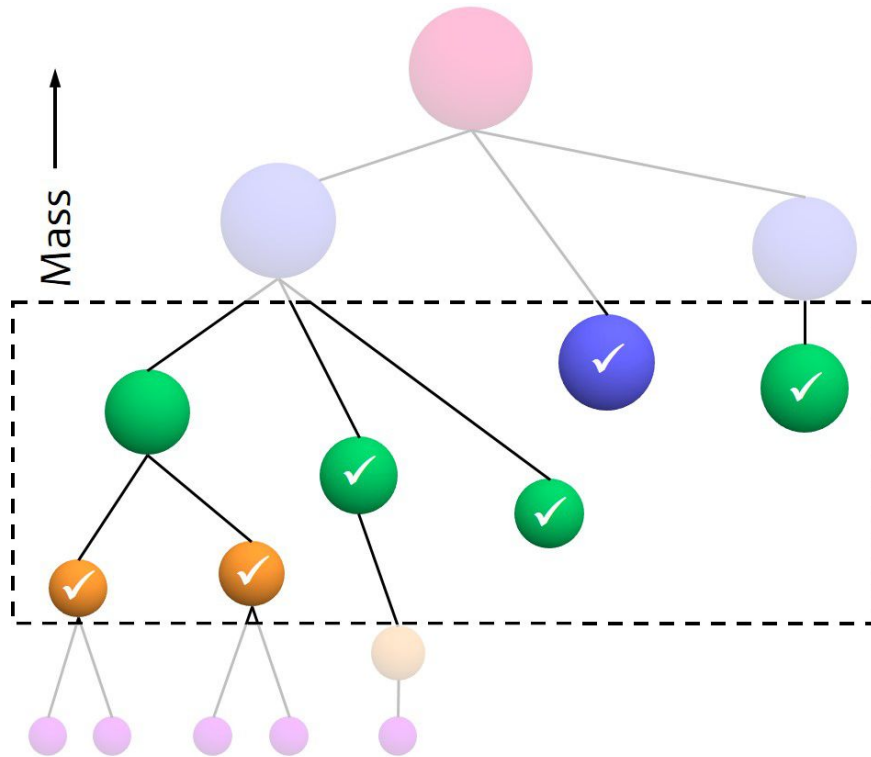


Figure 1.4: Schematic showing selection of galaxy analogues from a hierarchy of subhaloes. The dotted lines indicate the mass limits applied to all haloes – haloes at any level in the hierarchy are considered as candidate galaxy analogues. The final selection keeps only those haloes that could host galaxies (haloes with tickmarks), while accounting for overlapping haloes and subhaloes. For example, the leftmost green halo is removed since it is likely to host two galaxies (orange haloes) which are already accounted for.

1.6 This thesis

Galaxies in groups and clusters can undergo several different processes that alter their composition, structure, star formation rate and morphology. In this thesis, we are particularly interested in understanding the ways in which galaxies lose mass as they are accreted onto groups and clusters as well as the role that preprocessing (defined below) plays in determining this mass loss. Groups have lower gravitational potentials and therefore exert weaker tidal forces. They also have less hot gas which implies lower ram pressures imposed by the IGM. At the same time, lower relative velocities between galaxies can lead to higher merger rates. Dynamical friction is also stronger when the velocities involved are lower, which implies that it may be more efficient at the group scale rather than the cluster scale. In order to study mass segregation, mass loss and preprocessing of dark matter haloes and galaxies in groups environments, we make use of a dark-matter simulation of a large cosmological volume described in Chapters 2 and 3 and a zoom-in hydrodynamical simulation of a galaxy group described in Chapter 4.

In Chapter 2, we examine the phenomenon of mass segregation in group and cluster haloes at $z = 0$. Mass segregation is a radial trend in the average mass of galaxies in a group or cluster, with galaxies near the centre of the group/cluster being more massive. If it is observed in groups and clusters, it could be the result of dynamical friction driving more massive haloes towards the centres of galaxies. However, it could also be the result of the assembly history of the group or cluster. Haloes that are accreted early are found closer to the centres of the groups/clusters; if they are preferentially more massive, this can directly lead to mass segregation without requiring dynamical friction. Previous studies have found conflicting results in both observations and simulations. Observational studies such as [Lares et al. \(2004\)](#); [van den Bosch et al. \(2008\)](#); [von der Linden et al. \(2010\)](#); [Ziparo et al. \(2013\)](#); [Roberts et al. \(2015\)](#) have found at most weak mass segregation which is stronger in groups than in clusters. Simulation studies such as [Contini & Kang \(2015\)](#); [van den Bosch et al. \(2016\)](#) also find weak but significant segregation. On the other hand [Kafle et al. \(2016\)](#) compared results from observations, simulations as well as semi-analytical modelling and found no evidence of mass segregation. In Chapter 2, we study mass segregation using a dark matter simulation of a large cosmological volume. To do so, we first develop a

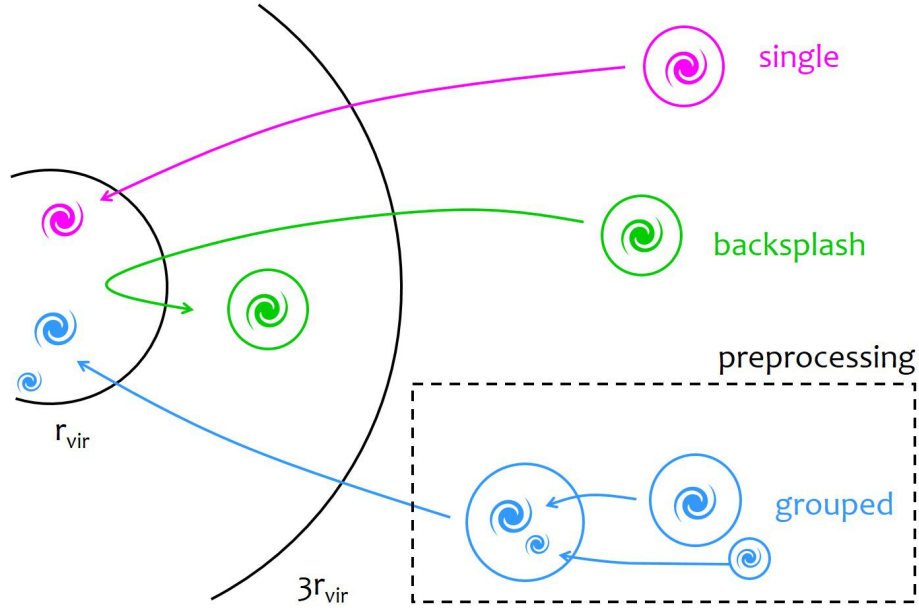


Figure 1.5: Schematic of single vs. grouped galaxies to illustrate preprocessing. Single galaxies are those that have been distinct for their entire history before being accreted onto the group/cluster, indicated by the r_{vir} circle. Grouped galaxies were part of an external group before they were accreted by the final group/cluster. The green galaxy also illustrates backsplash galaxies that have crossed within r_{vir} in the past and may now be found at larger radii. We chose to keep all galaxies within $3r_{\text{vir}}$ for our analysis.

simple set of criteria to select a sample of galaxy analogues that can represent observed populations of galaxies.

In Chapter 3, we extend the results from Chapter 2 to trace the accretion and mass loss and mass gain histories of the galaxy analogues. While previous studies have found mild to no mass segregation, radial trends in the mass *lost* by galaxies have been found to be much stronger, with galaxies closest to the group/cluster centre having lost the most mass (e.g. [van den Bosch et al., 2016](#)). According to the hierarchical model of structure formation, massive groups and clusters form not only by accreting individual galaxies but also small groups of galaxies, the members of which may have already experienced some of the environmental processes mentioned above. This phenomenon of galaxies being preprocessed can affect our understanding of the efficiency of evolutionary processes affecting galaxies in different environmental regimes (e.g. [McGee et al., 2009](#); [Bahé et al., 2013](#); [Hou et al., 2014](#); [Bahé & McCarthy, 2015](#); [Wetzel et al., 2015](#); [Gabor & Davé, 2015](#)). Fig. 1.5 shows a schematic of ‘single’

galaxies, which were distinct for their entire histories before becoming part of the final group/cluster and ‘grouped’ galaxies, which had been part of an external group at some point before accretion onto the final group/cluster. The figure also shows a population of ‘backsplash’ galaxies that have crossed within the group/cluster in the past, but may now be found at larger radii. Such galaxies have distinct dynamical properties from galaxies within the group/cluster (e.g. see [Mahajan et al., 2011](#); [Oman et al., 2013](#)). We therefore examine the mass loss histories of galaxy analogues as well as the consequences of preprocessing in this chapter and treat backsplash galaxies as a separate case.

In Chapter 4, we build on the previous two studies by focusing on a single group and carrying out a zoom-in, hydrodynamical simulation incorporating key baryonic physics elements. We examine the mass loss of galaxies as they approach and enter the group, now studying the dark matter, gaseous and stellar components separately. We are able to examine trends in hydrodynamical processes such as star formation and ram pressure stripping along the trajectories of individual galaxies. As with Chapter 3, we look at single and grouped galaxies separately to determine the effects of preprocessing and also compare them to a sample of unaccreted galaxies that have never been part of the group. We explore the mass loss experienced by single and grouped galaxies in dark matter, gas and stars separately to determine the effect of the group environment. We also track individual galaxies as they approach the group and are accreted onto it to study how their proximity to the group affects their mass loss. Finally, we examine the consequences of these galaxies’ evolution in the group on their final properties.

References

- Aarseth S. J., 1963, [MNRAS](#), **126**, 223
- Abadi M. G., Moore B., Bower R. G., 1999, [MNRAS](#), **308**, 947
- Allgood B., Flores R. A., Primack J. R., Kravtsov A. V., Wechsler R. H., Faltenbacher A., Bullock J. S., 2006, [MNRAS](#), **367**, 1781
- Bahé Y. M., McCarthy I. G., 2015, [MNRAS](#), **447**, 969
- Bahé Y. M., McCarthy I. G., Balogh M. L., Font A. S., 2013, [MNRAS](#), **430**, 3017

- Bailin J., Steinmetz M., 2005, [ApJ](#), **627**, 647
- Baldry I. K., Glazebrook K., Brinkmann J., Ivezić Ž., Lupton R. H., Nichol R. C., Szalay A. S., 2004, [ApJ](#), **600**, 681
- Baldry I. K., Balogh M. L., Bower R. G., Glazebrook K., Nichol R. C., Bamford S. P., Budavari T., 2006, [MNRAS](#), **373**, 469
- Balogh M. L., Navarro J. F., Morris S. L., 2000, [ApJ](#), **540**, 113
- Balogh M. L., Baldry I. K., Nichol R., Miller C., Bower R., Glazebrook K., 2004, [ApJ](#), **615**, L101
- Barnes J. E., 1992, [ApJ](#), **393**, 484
- Barnes J. E., Hernquist L. E., 1991, [ApJ](#), **370**, L65
- Barnes J. E., Hernquist L., 1992, [Nature](#), **360**, 715
- Behroozi P. S., Wechsler R. H., Wu H.-Y., 2013a, [ApJ](#), **762**, 109
- Behroozi P. S., Wechsler R. H., Conroy C., 2013b, [ApJ](#), **770**, 57
- Bell E. F., de Jong R. S., 2001, [ApJ](#), **550**, 212
- Binney J., Tremaine S., 1987, Galactic dynamics
- Blanton M. R., Moustakas J., 2009, [ARA&A](#), **47**, 159
- Blanton M. R., et al., 2003, [ApJ](#), **594**, 186
- Blanton M. R., Eisenstein D., Hogg D. W., Schlegel D. J., Brinkmann J., 2005, [ApJ](#), **629**, 143
- Bolzonella M., Miralles J.-M., Pelló R., 2000, [A&A](#), **363**, 476
- Bournaud F., Duc P.-A., Amram P., Combes F., Gach J.-L., 2004, [A&A](#), **425**, 813
- Boylan-Kolchin M., Ma C.-P., Quataert E., 2008, [MNRAS](#), **383**, 93
- Boylan-Kolchin M., Springel V., White S. D. M., Jenkins A., Lemson G., 2009, [MNRAS](#), **398**, 1150

- Brainerd T. G., Blandford R. D., Smail I., 1996, *ApJ*, **466**, 623
- Brinchmann J., Charlot S., White S. D. M., Tremonti C., Kauffmann G., Heckman T., Brinkmann J., 2004, *MNRAS*, **351**, 1151
- Brooks A. M., Kuhlen M., Zolotov A., Hooper D., 2013, *ApJ*, **765**, 22
- Bryan G. L., Norman M. L., 1998, *ApJ*, **495**, 80
- Bullock J. S., 2002, in Natarajan P., ed., *The Shapes of Galaxies and their Dark Halos*. pp 109–113 ([arXiv:astro-ph/0106380](https://arxiv.org/abs/astro-ph/0106380)), [doi:10.1142/9789812778017_0018](https://doi.org/10.1142/9789812778017_0018)
- Calzetti D., et al., 2007, *ApJ*, **666**, 870
- Chandrasekhar S., 1943, *ApJ*, **97**, 255
- Cicone C., et al., 2014, *A&A*, **562**, A21
- Civano F., Fabbiano G., Pellegrini S., Kim D.-W., Paggi A., Feder R., Elvis M., 2014, *ApJ*, **790**, 16
- Colpi M., Mayer L., Governato F., 1999, *ApJ*, **525**, 720
- Conselice C. J., 2003, *ApJS*, **147**, 1
- Conselice C. J., Bershadsky M. A., Jangren A., 2000, *ApJ*, **529**, 886
- Contini E., Kang X., 2015, *MNRAS*, **453**, L53
- Crain R. A., et al., 2009, *MNRAS*, **399**, 1773
- Crain R. A., et al., 2015, *MNRAS*, **450**, 1937
- Croton D. J., et al., 2006, *MNRAS*, **365**, 11
- Daddi E., et al., 2007, *ApJ*, **670**, 156
- Dalla Vecchia C., Schaye J., 2008, *MNRAS*, **387**, 1431
- Diemand J., Kuhlen M., Madau P., 2006, *ApJ*, **649**, 1
- Dressler A., 1980, *ApJ*, **236**, 351

- Driver S. P., Allen P. D., Liske J., Graham A. W., 2007, [ApJ](#), **657**, L85
- Dubois Y., Gavazzi R., Peirani S., Silk J., 2013, [MNRAS](#), **433**, 3297
- Eke V. R., et al., 2004, [MNRAS](#), **348**, 866
- Elbaz D., Cesarsky C. J., 2003, [Science](#), **300**, 270
- Fabbiano G., 1989, [ARA&A](#), **27**, 87
- Fabian A. C., 2012, [ARA&A](#), **50**, 455
- Font A. S., et al., 2008, [MNRAS](#), **389**, 1619
- Gabor J. M., Davé R., 2015, [MNRAS](#), **447**, 374
- Gadotti D. A., 2009, [MNRAS](#), **393**, 1531
- Gallazzi A., et al., 2009, [ApJ](#), **690**, 1883
- Gan J., Kang X., van den Bosch F. C., Hou J., 2010, [MNRAS](#), **408**, 2201
- Gilbank D. G., Baldry I. K., Balogh M. L., Glazebrook K., Bower R. G., 2010, [MNRAS](#), **405**, 2594
- Giovanelli R., et al., 2005, [AJ](#), **130**, 2598
- Glazebrook K., Tober J., Thomson S., Bland-Hawthorn J., Abraham R., 2004, [AJ](#), **128**, 2652
- Gottlöber S., Klypin A. A., Kravtsov A. V., 1999, in Giuricin G., Mezzetti M., Salucci P., eds, *Astronomical Society of the Pacific Conference Series Vol. 176, Observational Cosmology: The Development of Galaxy Systems*. p. 418 ([arXiv:astro-ph/9810445](#))
- Governato F., Willman B., Mayer L., Brooks A., Stinson G., Valenzuela O., Wadsley J., Quinn T., 2007, [MNRAS](#), **374**, 1479
- Gunn J. E., Gott III J. R., 1972, [ApJ](#), **176**, 1
- Guth A. H., 1981, [Phys. Rev. D](#), **23**, 347

- Hao C.-N., Kennicutt R. C., Johnson B. D., Calzetti D., Dale D. A., Moustakas J., 2011, [ApJ](#), **741**, 124
- Hogg D. W., et al., 2004, [ApJ](#), **601**, L29
- Holmberg E., 1941, [ApJ](#), **94**, 385
- Hopkins P. F., Hernquist L., 2006, [ApJS](#), **166**, 1
- Hopkins P. F., Hernquist L., Cox T. J., Di Matteo T., Robertson B., Springel V., 2006, [ApJS](#), **163**, 1
- Hopkins P. F., Cox T. J., Younger J. D., Hernquist L., 2009, [ApJ](#), **691**, 1168
- Hopkins P. F., Kereš D., Oñorbe J., Faucher-Giguère C.-A., Quataert E., Murray N., Bullock J. S., 2014, [MNRAS](#), **445**, 581
- Hou A., et al., 2013, [MNRAS](#), **435**, 1715
- Hou A., Parker L. C., Harris W. E., 2014, [MNRAS](#), **442**, 406
- Hudson M. J., et al., 2015, [MNRAS](#), **447**, 298
- Jiang C. Y., Jing Y. P., Faltenbacher A., Lin W. P., Li C., 2008, [ApJ](#), **675**, 1095
- Jing Y. P., Suto Y., 2002, [ApJ](#), **574**, 538
- Kafle P. R., et al., 2016, [MNRAS](#), **463**, 4194
- Kauffmann G., White S. D. M., Guiderdoni B., 1993, [MNRAS](#), **264**, 201
- Kauffmann G., et al., 2003, [MNRAS](#), **341**, 33
- Kauffmann G., White S. D. M., Heckman T. M., Ménard B., Brinchmann J., Charlot S., Tremonti C., Brinkmann J., 2004, [MNRAS](#), **353**, 713
- Kawata D., Mulchaey J. S., 2008, [ApJ](#), **672**, L103
- Keller B. W., Wadsley J., Benincasa S. M., Couchman H. M. P., 2014, [MNRAS](#), **442**, 3013
- Keller B. W., Wadsley J., Couchman H. M. P., 2016, [MNRAS](#), **463**, 1431

- Kewley L. J., Geller M. J., Jansen R. A., 2004, [AJ](#), **127**, 2002
- Kim D.-W., Fabbiano G., 2015, [ApJ](#), **812**, 127
- Klypin A., Holtzman J., 1997, ArXiv Astrophysics e-prints,
- Klypin A. A., Trujillo-Gomez S., Primack J., 2011, [ApJ](#), **740**, 102
- Knollmann S. R., Knebe A., 2009, [ApJS](#), **182**, 608
- Koyama Y., et al., 2008, [MNRAS](#), **391**, 1758
- Lacey C., Cole S., 1993, [MNRAS](#), **262**, 627
- Lares M., Lambas D. G., Sánchez A. G., 2004, [MNRAS](#), **352**, 501
- Larson R. B., Tinsley B. M., Caldwell C. N., 1980, [ApJ](#), **237**, 692
- Le Brun A. M. C., McCarthy I. G., Schaye J., Ponman T. J., 2014, [MNRAS](#), **441**, 1270
- Lilly S. J., Le Fevre O., Hammer F., Crampton D., 1996, [ApJ](#), **460**, L1
- Linde A. D., 1982, [Physics Letters B](#), **108**, 389
- Lintott C. J., et al., 2008, [MNRAS](#), **389**, 1179
- Lintott C., et al., 2011, [MNRAS](#), **410**, 166
- Madau P., Dickinson M., 2014, [ARA&A](#), **52**, 415
- Madau P., Ferguson H. C., Dickinson M. E., Giavalisco M., Steidel C. C., Fruchter A., 1996, [MNRAS](#), **283**, 1388
- Madau P., Pozzetti L., Dickinson M., 1998, [ApJ](#), **498**, 106
- Mahajan S., Raychaudhury S., 2009, [MNRAS](#), **400**, 687
- Mahajan S., Mamon G. A., Raychaudhury S., 2011, [MNRAS](#), **416**, 2882
- Makino J., Hut P., 1997, [ApJ](#), **481**, 83
- Masters K. L., et al., 2010, [MNRAS](#), **405**, 783

- Mayer L., Mastropietro C., Wadsley J., Stadel J., Moore B., 2006, [MNRAS](#), **369**, 1021
- McCarthy I. G., Frenk C. S., Font A. S., Lacey C. G., Bower R. G., Mitchell N. L., Balogh M. L., Theuns T., 2008, [MNRAS](#), **383**, 593
- McGee S. L., Balogh M. L., Bower R. G., Font A. S., McCarthy I. G., 2009, [MNRAS](#), **400**, 937
- Meyer M. J., et al., 2004, [MNRAS](#), **350**, 1195
- Mihos J. C., Hernquist L., 1994, [ApJ](#), **425**, L13
- Mihos J. C., Hernquist L., 1996, [ApJ](#), **464**, 641
- Mo H. J., White S. D. M., 2002, [MNRAS](#), **336**, 112
- Moore B., Katz N., Lake G., Dressler A., Oemler A., 1996, [Nature](#), **379**, 613
- Moore B., Lake G., Katz N., 1998, [ApJ](#), **495**, 139
- Morgan W. W., 1958, [PASP](#), **70**, 364
- Moustakas J., Kennicutt Jr. R. C., Tremonti C. A., 2006, [ApJ](#), **642**, 775
- Murphy E. J., et al., 2011, [ApJ](#), **737**, 67
- Navarro J. F., Frenk C. S., White S. D. M., 1996, [ApJ](#), **462**, 563
- Noeske K. G., et al., 2007, [ApJ](#), **660**, L43
- Oemler Jr. A., 1974, [ApJ](#), **194**, 1
- Okamoto T., Eke V. R., Frenk C. S., Jenkins A., 2005, [MNRAS](#), **363**, 1299
- Oman K. A., Hudson M. J., Behroozi P. S., 2013, [MNRAS](#), **431**, 2307
- Ostriker J. P., Tremaine S. D., 1975, [ApJ](#), **202**, L113
- Peñarrubia J., Pontzen A., Walker M. G., Koposov S. E., 2012, [ApJ](#), **759**, L42
- Peebles P. J. E., 1980, *The large-scale structure of the universe*
- Peng C. Y., Ho L. C., Impey C. D., Rix H.-W., 2002, [AJ](#), **124**, 266

- Planck Collaboration et al., 2016, *A&A*, **594**, A13
- Press W. H., Schechter P., 1974, *ApJ*, **187**, 425
- Rasera Y., Alimi J.-M., Courtin J., Roy F., Corasaniti P.-S., Füzfa A., Boucher V., 2010, in Alimi J.-M., Fuözfa A., eds, American Institute of Physics Conference Series Vol. 1241, American Institute of Physics Conference Series. pp 1134–1139 ([arXiv:1002.4950](#)), [doi:10.1063/1.3462610](#)
- Rees M. J., Ostriker J. P., 1977, *MNRAS*, **179**, 541
- Rieke G. H., Alonso-Herrero A., Weiner B. J., Pérez-González P. G., Blaylock M., Donley J. L., Marcillac D., 2009, *ApJ*, **692**, 556
- Roberts I. D., Parker L. C., Joshi G. D., Evans F. A., 2015, *MNRAS*, **448**, L1
- Rowlands K., et al., 2017, preprint, ([arXiv:1707.07989](#))
- Salim S., et al., 2007, *ApJS*, **173**, 267
- Sawala T., et al., 2016, *MNRAS*, **457**, 1931
- Scannapieco C., et al., 2012, *MNRAS*, **423**, 1726
- Schawinski K., et al., 2014, *MNRAS*, **440**, 889
- Schaye J., et al., 2010, *MNRAS*, **402**, 1536
- Schaye J., et al., 2015, *MNRAS*, **446**, 521
- Schiminovich D., et al., 2005, *ApJ*, **619**, L47
- Silk J., 1977, *ApJ*, **211**, 638
- Simard L., et al., 2002, *ApJS*, **142**, 1
- Smith R., et al., 2015, *MNRAS*, **454**, 2502
- Smith R., Choi H., Lee J., Rhee J., Sanchez-Janssen R., Yi S. K., 2016, *ApJ*, **833**, 109
- Springel V., 2005, *MNRAS*, **364**, 1105
- Springel V., Hernquist L., 2005, *ApJ*, **622**, L9

- Springel V., White S. D. M., Tormen G., Kauffmann G., 2001, [MNRAS](#), **328**, 726
- Springel V., et al., 2005, [Nature](#), **435**, 629
- Tanaka M., Goto T., Okamura S., Shimasaku K., Brinkmann J., 2004, [AJ](#), **128**, 2677
- Toomre A., 1977, in Tinsley B. M., Larson D. Campbell R. B. G., eds, Evolution of Galaxies and Stellar Populations. p. 401
- Toomre A., Toomre J., 1972, [ApJ](#), **178**, 623
- Tremaine S. D., Ostriker J. P., Spitzer Jr. L., 1975, [ApJ](#), **196**, 407
- Tremmel M., Karcher M., Governato F., Volonteri M., Quinn T. R., Pontzen A., Anderson L., Bellovary J., 2017, [MNRAS](#), **470**, 1121
- Vogelsberger M., et al., 2014, [MNRAS](#), **444**, 1518
- Wadsley J. W., Keller B. W., Quinn T. R., 2017, [MNRAS](#), **471**, 2357
- Walcher J., Groves B., Budavári T., Dale D., 2011, [Ap&SS](#), **331**, 1
- Walter F., Brinks E., de Blok W. J. G., Bigiel F., Kennicutt Jr. R. C., Thornley M. D., Leroy A., 2008, [AJ](#), **136**, 2563
- Weinmann S. M., Kauffmann G., van den Bosch F. C., Pasquali A., McIntosh D. H., Mo H., Yang X., Guo Y., 2009, [MNRAS](#), **394**, 1213
- Wetzel A. R., Tinker J. L., Conroy C., 2012, [MNRAS](#), **424**, 232
- Wetzel A. R., Tinker J. L., Conroy C., van den Bosch F. C., 2013, [MNRAS](#), **432**, 336
- Wetzel A. R., Deason A. J., Garrison-Kimmel S., 2015, [ApJ](#), **807**, 49
- Whitaker K. E., van Dokkum P. G., Brammer G., Franx M., 2012, [ApJ](#), **754**, L29
- White S. D. M., 1977, [MNRAS](#), **179**, 33
- White S. D. M., Frenk C. S., 1991, [ApJ](#), **379**, 52
- Wilson C. D., 1995, [ApJ](#), **448**, L97
- Wolf C., Gray M. E., Meisenheimer K., 2005, [A&A](#), **443**, 435

Wolf C., et al., 2009, [MNRAS](#), **393**, 1302

Wu H., Cao C., Hao C.-N., Liu F.-S., Wang J.-L., Xia X.-Y., Deng Z.-G., Young C. K.-S., 2005, [ApJ](#), **632**, L79

Young J. S., et al., 1995, [ApJS](#), **98**, 219

Ziparo F., et al., 2013, [MNRAS](#), **434**, 3089

van den Bosch F. C., Pasquali A., Yang X., Mo H. J., Weinmann S., McIntosh D. H., Aquino D., 2008, preprint, ([arXiv:0805.0002](#))

van den Bosch F. C., Jiang F., Campbell D., Behroozi P., 2016, [MNRAS](#), **455**, 158

von Hoerner S., 1960, [ZAp](#), **50**

von der Linden A., Wild V., Kauffmann G., White S. D. M., Weinmann S., 2010, [MNRAS](#), **404**, 1231

CHAPTER 2

UNCOVERING MASS SEGREGATION WITH GALAXY ANALOGUES IN DARK-MATTER SIMULATIONS

Reprinted from

Joshi, Gandhali J., Parker, Laura C., Wadsley, James, 2016, MONTHLY NOTICES OF THE ROYAL ASTRONOMICAL SOCIETY, Volume 462, Issue 1, p. 761-777, DOI: 10.1093/mnras/stw1699. Published by Oxford University Press on behalf of the Royal Astronomical Society. All rights reserved.

Abstract

We investigate mass segregation in group and cluster environments by identifying galaxy analogues in high-resolution dark matter simulations. Subhaloes identified by the Amiga’s Halo Finder (AHF) and ROCKSTAR halo finders have similar mass functions, independent of resolution, but different radial distributions due to significantly different subhalo hierarchies. We propose a simple way to classify subhaloes as galaxy analogues. The radial distributions of galaxy analogues agree well at large halo-centric radii for both AHF and ROCKSTAR but disagree near parent halo centres where the phase-space information used by ROCKSTAR is essential.

We see clear mass segregation at small radii (within $0.5 r_{\text{vir}}$) with average galaxy analogue mass decreasing with radius. Beyond the virial radius, we find a mild trend where the average galaxy analogue mass increases with radius. These mass segregation trends are strongest in small groups and dominated by the segregation of low-mass analogues. The lack of mass segregation in massive galaxy analogues suggests that the observed trends are driven by the complex accretion histories of the parent haloes rather than dynamical friction.

2.1 Introduction

Galaxies in groups and clusters are known to exhibit different properties compared to field galaxies. They have redder colours, more elliptical morphologies and suppressed star formation rates (e.g. Oemler, 1974; Dressler, 1980; Balogh et al., 2004; Hogg et al., 2004; Kauffmann et al., 2004; Blanton et al., 2005). On large scales, structure in the Universe grows hierarchically; smaller dark-matter haloes collapse earlier while larger structures form later through the coalescence of these smaller haloes. Baryons are accreted into the potentials of these haloes to form galaxies. As they are accreted onto larger objects, their properties transition from those of field galaxies to those of group/cluster galaxies. This is evidenced by observed radial trends in several different properties such as luminosity and morphology (e.g. Girardi et al., 2003), colour (e.g. Blanton & Berlind, 2007), quenched fractions (e.g. Wetzel et al., 2012) and star formation rates (e.g. Balogh et al., 2000). Such a correlation between an average galaxy property and distance from the group/cluster centre is defined as segregation.

Segregation in observed properties may be largely driven by baryonic physics. Several mechanisms can transform galaxies in groups/clusters – harassment and tidal interactions with other nearby galaxies can remove gas, stars and dark matter (Moore et al., 1996, 1998); gas removal can result in strangulation and the prevention of future star formation (Larson et al., 1980; Balogh et al., 2000; Kawata & Mulchaey, 2008); ram pressure stripping can remove the more bound cold gas (Gunn & Gott, 1972; Abadi et al., 1999); mergers can trigger starbursts that rapidly consume the fuel for star formation (Makino & Hut, 1997; Angulo et al., 2009). Mass segregation, on the other hand, could arise due purely to the interactions of the dark-matter haloes in which galaxies reside and the larger potential of the group or cluster. Understanding mass segregation may shed light on the processes of galaxy evolution in these environments and whether baryons or dark matter play the dominant role. Additionally, several galaxy properties such as luminosity, stellar ages and metallicities etc. are correlated with the galaxy’s stellar mass as well as halo mass. Therefore, any radial segregation of these properties may at least partially be the result of mass segregation. Dynamical friction (Chandrasekhar, 1943) is predicted to play an important role in driving mass segregation (Ostriker & Tremaine, 1975; Tremaine et al., 1975; White,

1977); the resultant drag force increases with mass resulting in massive objects being preferentially found near the centre of the group or cluster.

The existence of mass segregation in different environments is still a topic of debate. Observational studies such as Lares et al. (2004) analyzed the dynamical properties of group galaxies from 2dFGRS and found significant segregation trends by examining the differences in the velocity functions of galaxies of different luminosity (and therefore stellar mass) ranges. van den Bosch et al. (2008) also found stellar mass segregation trends with projected radius using data from the Sloan Digital Sky Survey Data Release 7 (SDSS-DR7; Abazajian et al., 2009). They concluded that segregation trends in colour and concentration naturally arise due to mass segregation and the correlation between stellar mass and colour/concentration. Roberts et al. (2015) also found evidence for weak (stellar) mass segregation using galaxy groups in SDSS-DR7. They concluded that the mass segregation trend is strengthened by the inclusion of low-mass galaxies and that the trend is weaker in higher mass groups/clusters. On the other hand, von der Linden et al. (2010) studied cluster galaxies in SDSS and found no evidence of stellar mass segregation in their sample. Ziparo et al. (2013) only found a mild segregation trend in stellar mass in the low-redshift end of their sample of X-ray selected groups from the COSMOS, GOODS and ECDFS fields.

Studies of simulated galaxies have also explored mass segregation. Contini & Kang (2015) used dark-matter simulations along with semi-analytic models in four different host mass regimes ranging from $10^{13} h^{-1}M_{\odot}$ to greater than $5 \times 10^{14} h^{-1}M_{\odot}$. They found that within a virial radius, the mean galaxy mass decreases with halo-centric distance while between $1-2 R_{\text{vir}}$, it increases with distance. Most recently, van den Bosch et al. (2016) conducted an extensive study of the segregation of various properties of subhaloes in the Bolshoi and Chinchilla simulations. Their sample consisted of host haloes with a minimum mass of $6.7 \times 10^{12} h^{-1}M_{\odot}$ from the Bolshoi simulation and $7.2 \times 10^{12} h^{-1}M_{\odot}$ and $3.0 \times 10^{13} h^{-1}M_{\odot}$ for the two Chinchilla simulations. They found a weak correlation between the subhaloes' present-day mass and their location in the larger host halo, although they found other indicators such as the mass at infall and the amount of mass lost after infall to be more strongly correlated with radius.

The lack of consensus among these studies is partly due to the differences in the way mass segregation is measured in observational data versus simulated data. Observational studies generally focus on trends in stellar mass and projected radial separation from halo centres; studies of simulations use 3D separations (although note

that several authors do also look at projection effects and how these can alter their results; e.g. [van den Bosch et al., 2016](#)). Simulation studies also generally consider dark matter halo masses, since the conversion from halo mass to stellar mass requires either an assumed stellar mass–halo mass relation, semi-analytical modelling or sophisticated hydrodynamical simulations. Each of these techniques can add scatter to the relation due to the additional assumptions regarding star formation and feedback.

Understanding mass segregation requires an understanding of the assembly history of the system. Observationally, we cannot follow an individual galaxy over its entire lifetime. Instead, we observe galaxies at different epochs and infer the processes occurring over time. Another challenge is that although $\sim 50\%$ of galaxies at low redshifts are associated with a group or cluster, groups become difficult to detect without extensive spectroscopy over large areas. Cosmological simulations can be used to help overcome these challenges, as we are able to identify haloes at every time step and track the evolution of a single halo through its lifetime. Simulations also provide full phase-space information which could be key in finding group/cluster members.

In order to use simulations to study galaxy evolution, it is critical to first robustly identify haloes and subhaloes. Several different techniques have been used to identify haloes in simulations. One set of early halo finders used a Friends-of-Friends (FOF) algorithm that links together particles separated by distances smaller than a linking length ‘ b ’, usually specified as a fraction of the mean interparticle spacing in the simulation ([Davis et al., 1985](#)). These early algorithms would occasionally link two distinct haloes through a tenuous bridge of particles and were also unable to detect substructure due to the use of a single linking length ([Knollmann & Knebe, 2009](#)). Spherical overdensity (SO) algorithms did not suffer from the first problem. These algorithms identify particles around density peaks and determine a terminal radius at which the average density within the sphere is the critical density of the Universe multiplied by a factor that comes from the spherical collapse model ([Lacey & Cole, 1994](#)). Nearly all current halo finders are descendants of one of these two fundamental algorithms.

The next step is to detect substructure within the overdensities of the distinct haloes. Several algorithms that can detect subhaloes now exist including bound density maxima (BDM) ([Klypin & Holtzman, 1997](#)), Subhalo Finder (SUBFIND) ([Springel et al., 2001](#)), Amiga’s Halo Finder (AHF) ([Knollmann & Knebe, 2009](#)) and ROCK-

STAR (Behroozi et al., 2013). In this work, we examine the performance of AHF and ROCKSTAR in detecting substructure for the purpose of studying mass segregation. Previous studies have tended to only include direct ‘subhaloes’ i.e. a single level lower than the parent halo, and sometimes ‘subsubhaloes’ of the host halo in their analysis; here, we investigate the consequences of such criteria. There have been past efforts in comparing the performance of various halo finders e.g. Lacey & Cole (1994); Cole & Lacey (1996); White (2002); Knollmann & Knebe (2009); Lukić et al. (2009); Muldrew et al. (2011); Behroozi et al. (2013). We compare our results to the recent work of Knebe et al. (2011) with the *Haloes gone MAD* project and Onions et al. (2012) with the *Subhaloes gone Notts* project. Knebe et al. (2011) carried out an extensive comparison project, using several popular halo finders including AHF and ROCKSTAR, studying their ability to accurately reconstruct particle memberships, centres, masses, bulk velocities and dispersions etc. from mock data as well from an actual simulation. They found that both AHF and ROCKSTAR were able to recover the masses of the mock halo and subhalo to within $\sim 5\%$ although only phase-space halo finders such as ROCKSTAR were able to detect subhaloes at very small separations from the host halo centre. Onions et al. (2012) examined the properties of subhaloes embedded in a single Milky Way-like halo from the Aquarius project (Springel et al., 2008) using several different halo finders. They found good agreement between AHF and ROCKSTAR in terms of the subhalo mass functions (MFs) and radial distributions they detected.

Comparing the mass and radial distributions of the subhaloes detected by both halo finders prompts the need to select a new population of ‘galaxy analogues’ that better corresponds to observed galaxy populations. We then use these galaxy analogues to search for possible mass segregation trends not only in the total sample, but also separating by host halo mass in order to study possible environmental effects. The paper is organized as follows: in Section 2.2, we provide the details of the simulation and describe the halo finding algorithms used in this study. In Section 2.3 we look at the MFs of haloes and subhaloes detected by both halo finders at all three resolutions. Section 2.4 examines the radial distributions of subhaloes and motivates the need to select galaxy analogues. Section 2.5 describes the selection criteria for these analogues and examines their mass and radial distributions. Finally, with this new population, we look for possible mass segregation trends and the effects of host mass and low-mass ‘galaxies’ in Section 2.6.

2.2 Methods

2.2.1 Simulation

We performed collisionless, cosmological N-body simulations using the Tree-SPH code CHANGA (Jetley et al., 2008, 2010; Menon et al., 2015) at three different resolutions. The simulation volume was a comoving box of length 100 Mpc on each side. The low-, medium- and high-resolution runs contained 256^3 , 512^3 and 1024^3 particles, respectively, with gravitational softening lengths of 5, 2.5 and 1.25 kpc, resulting in particle masses of $2.4 \times 10^9 M_\odot$, $2.9 \times 10^8 M_\odot$ and $3.7 \times 10^7 M_\odot$ respectively. The softening lengths are comoving for $z > 8$, physical at lower redshifts. Initial conditions (ICs) were generated using MUSIC (Hahn & Abel, 2013) assuming a flat Λ cold dark matter cosmology with $n_s = 0.9611$, $\sigma_8 = 0.8288$, $\Omega_\Lambda = 0.6814$, $\Omega_m = 0.3086$, $h = 0.6777$ (the cosmological parameters were obtained from Planck Collaboration et al., 2014). The same parameters and random number seeds were used at all three resolutions in order to ensure that we recovered the same large-scale structures. Note that MUSIC requires mass and dimension values to be in h -inverse units whereas CHANGA does not. We chose to work in absolute units for the entire analysis; since the halo finders also output masses and radii etc. in h -inverse units, we first convert all quantities to absolute units using the value of h from Planck Collaboration et al. (2014). Each simulation was started at a redshift of $z = 100$ and evolved to $z = 0$ in 1000 linear timesteps (output every 25 timesteps). For a first look at the results, Fig. 2.1 shows projected density maps of the most massive halo at all three resolutions (the centre coordinates and radius are taken from the highest-resolution run). The overall large-scale structures are recovered well at all three resolutions.

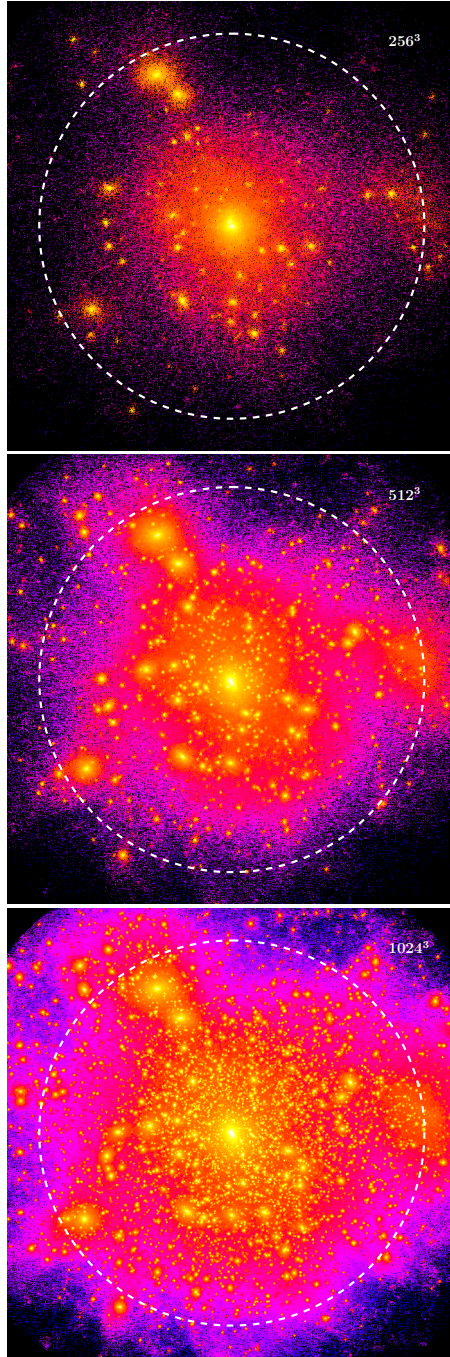


Figure 2.1: Projected density of the most massive distinct halo at all three resolutions. The white dotted line shows virial radius $r_{\text{vir}} = 2.18$ Mpc. Particles are coloured according to a smoothed density on a logarithmic scale. Centre coordinates and radius were taken from the highest resolution run. The same large-scale features are recovered at all three resolutions.

2.2.2 Halo finding

We first compare the performance of halo finders that use both spatial and velocity information versus those that only use spatial information. The velocity information may not provide much additional help in identifying isolated haloes that are spatially well separated. However, in high-density environments where several haloes are found in a small volume, as well as when multiple haloes live within a larger host halo, halo finders which use velocity information have been shown to be better at finding distinct haloes and subhaloes (e.g. [Knebe et al., 2011](#)). We used two representative algorithms – AHF which is a spatial algorithm, and ROCKSTAR which is a phase space algorithm. The two codes employ different techniques to identify potential haloes and subhalo hierarchies as described below. In both halo finders, the virial radius is defined as the radius within which the average density is given by

$$\bar{\rho}_{\text{vir}}(z) = \Delta_c(z)\rho_c(z) = \Delta_m(z)\rho_m(z) \quad (2.1)$$

where ρ_c is the critical density of the Universe and ($\rho_m = \Omega_m\rho_c$) is the background matter density at the given redshift. The factor Δ_c is calculated for a flat matter- Λ Universe following [Bryan & Norman \(1998\)](#) as

$$\Delta_c(z) = 18\pi^2 + 82x - 39x^2 \quad (2.2)$$

where

$$x = \frac{\Omega_{m,0}(1+z)^3}{\Omega_{m,0}(1+z)^3 + \Omega_\Lambda} - 1 \quad (2.3)$$

With the cosmological parameters used in this study we find $\Delta_c = 102$ and $\Delta_m = 332$ at $z = 0$.

2.2.2.1 AMIGA's Halo Finder

AHF identifies haloes as spherical overdensities in the spatial distribution of particles in simulations. The major steps in the algorithm are as follows (see [Knollmann & Knebe \(2009\)](#) for further details).

1. An Adaptive Mesh Refinement (AMR) grid is generated starting from a coarse regular grid; any cell whose particle density exceeds a specified threshold (N_{per} -

$RefCell=5$) is refined by splitting it into eight equally-sized cells. The process is repeated until no cell exceeds the particle density threshold.

2. Starting at the finest refinement level, contiguous regions at each refinement level are marked as potential haloes. A grid hierarchy is also built whereby each potential halo at a finer refinement level is linked to the region it resides in at the (coarser) level above it.
3. When multiple potential haloes at one level live within the same region at an upper level, the potential halo with the most number of particles is assigned to be the ‘host’; the rest are designated ‘subhaloes’. This process is repeated at every refinement level.
4. The ‘leaves’ of this grid hierarchy, i.e. the haloes at the finest refinement levels, are assumed to be the centres of potential haloes. Particles within a given radius are assigned to these centres. For a host halo with no subhaloes, this radius is the first isodensity contour where the density is lower than the required $\bar{\rho}$. For subhaloes, the radius is half the distance to the host halo.
5. An iterative unbinding procedure is performed to remove particles with speeds greater than the escape velocity \times a tunable factor. Unbound particles from a subhalo are considered for boundedness to the host halo. This is done for all potential halo centres to determine a final list of haloes. Only haloes with a minimum number of particles (*for this study, $N_{minPerHalo}=20$*) are kept in the final output.
6. Further halo properties are calculated using the bound particles assigned to the halo. Note that subhalo particles are included when calculating ‘host’ halo properties. By construction, all particles within the virial radius are bound to the halo.

2.2.2.2 ROCKSTAR

ROCKSTAR identifies haloes as overdensities in the 6D phase-space distribution of the simulation particles, using an FOF algorithm. The major steps in the algorithm are as follows (see [Behroozi et al. \(2013\)](#) for further details). Note that although there are a number of tunable parameters whose values we specify below, we use the default values recommended by [Behroozi et al. \(2013\)](#) as they have been extensively tested.

1. Initially, overdense regions in the spatial distribution of particles are identified using a modified fast 3D FOF algorithm with a single large linking length. This is done only in order to break up the simulation into independent units that can be further analysed in parallel.
2. Within a single overdense region (‘parent group’), phase-space overdensities are identified using a 6D FOF method with a distance metric defined as

$$d(p_1, p_2) = \sqrt{\frac{|\mathbf{x}_1 - \mathbf{x}_2|^2}{\sigma_x^2} + \frac{|\mathbf{v}_1 - \mathbf{v}_2|^2}{\sigma_v^2}} \quad (2.4)$$

where σ_x and σ_v are the dispersions in the particle positions and velocities for the region. The linking length is chosen such that a specific fraction of particles ($FOF_FRACTION=0.7$) are linked to at least one other particle.

3. The process is repeated at each level generating a hierarchy of subgroups; a tighter linking length is chosen at each level, corresponding to a higher overdensity. It is terminated when a group reaches a specified minimum number of particles ($MIN_HALO_PARTICLES=10$).
4. The FOF groups at the finest refinement level become ‘seed haloes’. If a parent group contains a single seed halo, all particles in the parent group are assigned to the seed. If multiple seeds exist in a single parent group, particles are assigned to the closest seed halo in phase-space using a modified distance metric.
5. Halo–subhalo relations are determined by treating the ‘seed haloes’ as single particles and calculating a modified distance metric to all haloes with larger numbers of assigned particles. The halo in question is then assigned to be the subhalo of the nearest larger halo in phase space.
6. An unbinding procedure is carried out to remove unbound particles. Halo properties are then calculated using only bound particles. Only haloes with a minimum number of assigned particles are included in the final output (*for this study*, $MIN_HALO_OUTPUT_SIZE=20$). Also not included in the final output are any haloes whose fraction of unbound particles exceeds a maximum threshold ($UNBOUND_THRESHOLD=0.5$)

2.3 Mass functions

We first compare the overall mass distributions of the host haloes and their satellites as identified by the two halo finders through their mass functions (MFs). Throughout this paper, the set of ‘distinct’ haloes are those that do not have a parent i.e. they are at the top level of the subhalo hierarchy. Of these, only distinct haloes with $M_{\text{vir}} \geq 10^{12.5} M_{\odot}$ are taken to be part of the ‘parent’ halo set. Based on the $M_h - M_*$ relations in [Hudson et al. \(2015\)](#), this corresponds to a stellar mass of roughly $M_* = 10^{11} M_{\odot}$; any haloes more massive than this are expected to contain more than a single galaxy and would therefore qualify as host haloes. The *direct* subhaloes of these parent haloes, i.e. only one level down in the subhalo hierarchy, whose centres lie within one virial radius from the parent halo centre are considered to be the ‘subhalo’ population. For reference, [Table 2.1](#) provides the numbers of distinct haloes and subhaloes detected by both halo finders in the highest-resolution simulation within various mass ranges.

Table 2.1: Numbers of distinct haloes, subhaloes and galaxy analogues identified by both halo finders in the high-resolution simulation, in various mass ranges. The numbers in brackets are the average value for a single parent halo. Since analogues are identified out to $3 r_{\text{vir}}$ while subhaloes only extend to $1 r_{\text{vir}}$, we also provide numbers of galaxy analogues within $1 r_{\text{vir}}$

Subset	ROCKSTAR	AHF
Distinct haloes		
$M_{\text{vir}} \geq M_{\text{complete}} (= 10^9 M_{\odot})$	787,374	810,082
$M_{\text{vir}} \geq 10^{12.5} M_{\odot}$	606	604
$10^{12.5} \leq M_{\text{vir}} < 10^{13} M_{\odot}$	411	409
$10^{13} \leq M_{\text{vir}} < 10^{14} M_{\odot}$	178	178
$10^{14} \leq M_{\text{vir}} < 10^{15} M_{\odot}$	17	17
Subhaloes with $M_{\text{vir}} \geq 10^{10} M_{\odot}$ and $M_{\text{parent}} \geq 10^{12.5} M_{\odot}$		
Total	10,145 (17)	11,535 (20)
$10^{12.5} \leq M_{\text{par}} < 10^{13} M_{\odot}$	2,501 (7)	2,659 (7)
$10^{13} \leq M_{\text{par}} < 10^{14} M_{\odot}$	4,382 (25)	4,849 (28)
$10^{14} \leq M_{\text{par}} < 10^{15} M_{\odot}$	3,262 (192)	4,027 (237)
Galaxy analogues with $M_{\text{parent}} \geq 10^{12.5} M_{\odot}$		
Total	43,864 (36)	44,070 (36)
$10^{12.5} \leq M_{\text{par}} < 10^{13} M_{\odot}$	10,349 (26)	10,311 (26)
$10^{13} \leq M_{\text{par}} < 10^{14} M_{\odot}$	18,925 (107)	18,753 (106)
$10^{14} \leq M_{\text{par}} < 10^{15} M_{\odot}$	14,590 (859)	15,006 (883)
Galaxy analogues with $M_{\text{parent}} \geq 10^{12.5} M_{\odot}$ and $r < r_{\text{vir}}$		
Total	13,726 (23)	14,213 (24)
$10^{12.5} \leq M_{\text{par}} < 10^{13} M_{\odot}$	2,910 (8)	3,374 (9)
$10^{13} \leq M_{\text{par}} < 10^{14} M_{\odot}$	5,644 (32)	6,152 (35)
$10^{14} \leq M_{\text{par}} < 10^{15} M_{\odot}$	5,172 (305)	4,687 (276)

2.3.1 Distinct haloes

Fig. 2.2(a) shows the MFs of the distinct haloes detected at all three resolutions and by both halo finders. The errors shown are Poisson errors. Qualitatively, the two halo finders produce consistent results down to the completeness limits of $M_{\text{vir}} = (10^{11}, 10^{10}, 10^9)M_{\odot}$ for the low-, mid- and high-resolution runs, respectively. These completeness limits are set by requiring that each halo is resolved by a minimum of 25 particles. The ROCKSTAR MFs extend to lower masses than AHF. This is because in AHF, the user specifies the minimum *bound* particles a halo must have to be included in the final output (20 in this study); in ROCKSTAR the minimum threshold specifies how many particles have been uniquely assigned to the FOF group, but due to the aspherical nature of these groups, a significant number of these particles can lie outside the virial radius, which means the virial mass for the haloes can be lower than the mass of 20 particles. However, these differences are at masses lower than the completeness limit and therefore do not impact our analysis.

The MFs appear to be a single power law down to the completeness limit with no flattening evident at the low-mass end. At the high-mass end, there does appear to be some evidence of the exponential drop off expected for a Schechter function, but we are limited by low number statistics and cannot probe this region with any certainty. For a quantitative comparison, we instead fit a single power law between the completeness limit for the particular resolution and $M_{\text{vir}} = 10^{13}M_{\odot}$. The upper mass limit is set by requiring a maximum relative uncertainty of 10%, which is equivalent to having at least 100 haloes in each bin. The results of the power-law fits for both halo finders and all three resolutions are shown in Figure 2.3. (These values are also provided in Table 2.3 in the Appendix.)

Considering each resolution separately, we find that the two halo finders produce identical MFs for distinct haloes both in terms of slope and normalization. The MFs for the mid- and high-resolution runs are nearly identical as well; their slopes agree within 1σ and normalizations within 2σ . For the low-resolution run however, we find a systematically steeper slope as well as a higher normalization; this is partly due to less substructure created in the simulations.

Knebe et al. (2011) find similar agreement between AHF and ROCKSTAR using a mock data set. They provide three different systems with known masses, centres and velocity offsets – (i) a single halo, (ii) a halo with an embedded subhalo and (iii) a halo with an embedded subhalo as well as a subsubhalo – as input and compare

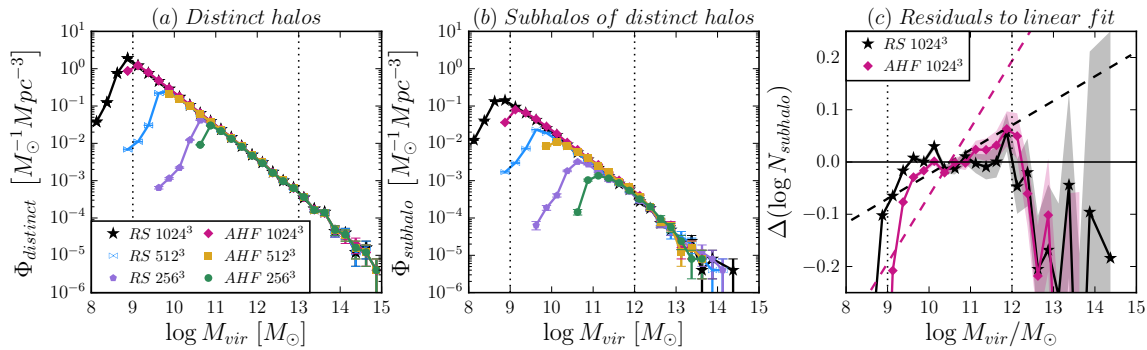


Figure 2.2: (a): Mass functions (MFs) of distinct haloes identified by both halo finders and at all three resolutions. $\Phi = dn/d\log M_{\text{vir}}$ is the number density of haloes per unit $\log(\text{mass})$. (b): MFs of subhaloes; colours are identical to (a). The uncertainties in both these plots are calculated as Poisson errors. (c) Differences between subhalo MFs and corresponding distinct halo MFs to compare their slopes. We fit a power-law model of the form $[\log \Phi = a \log M_{\text{vir}} + b]$ to the MFs within the mass ranges indicated by the vertical dotted lines in (a) and (b) (these limits are explained in the text). The fits from (a) are then normalized at $M = 10^{10.5} M_{\odot}$ to match the corresponding value in (b). The data points show the residuals between the subhalo MFs and the renormalized distinct halo MF fits. The dashed lines show the difference between the subhalo MF fits and the renormalized distinct halo MF fits. For both halo finders, the subhalo MF appears to be shallower than the corresponding distinct MF, although the difference for ROCKSTAR is smaller than for AHF.

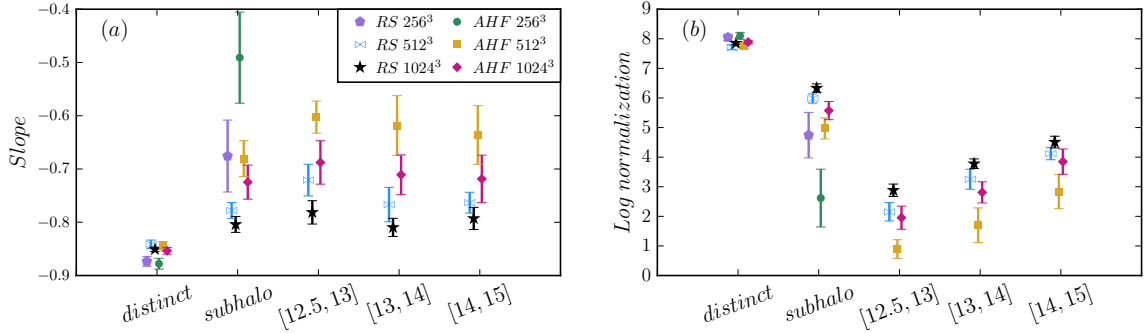


Figure 2.3: (a): Log slopes and (b): log-normalizations from power-law fits to the MFs shown in Figs 2.2 and 2.11. The various samples shown here are the distinct haloes, the complete sample of subhaloes and the three subhaloes samples in bins of host mass $\log M_{\text{parent}} = [12.5, 13]$, $[13, 14]$ and $[14, 15]$ respectively. Arbitrary offsets were applied in the x -direction for clarity. We only use data points within a specific range in $\log M_{\text{vir}}$ – the lower limit is set by requiring a minimum of 25 particles in each halo, which corresponds to 11, 10 and 9 for the low-, mid- and high-resolutions runs respectively; the upper limit is set by requiring a maximum relative error of 10%, which corresponds to 13 for the distinct haloes, 12 for the total sample of subhaloes and 11.25 for the binned subhaloes samples.

the results from several different halo finders. The recovered masses for the isolated haloes from AHF and ROCKSTAR are within $\sim 5\%$ of the input values as well as each other, although note that these masses were not the values returned by the halo finders themselves. Instead, Knebe et al. (2011) use the locations of the haloes and the particles belonging to them to calculate halo properties using a single code in order to eliminate any differences in the way these properties are calculated by the halo finders.

There are a number of high-resolution simulations of large cosmological volumes that we can compare our results to, such as the Bolshoi simulation (Klypin et al., 2011) and the Illustris project (specifically the Illustris-1-Dark simulations; Vogelsberger et al., 2014). While the MFs for these simulations were both fit by an empirically derived formula from Sheth & Tormen (2002), the simulations were large enough to have over 10 times the number of haloes that we have in our simulation. They therefore had much better statistics at the high-mass end where we expect a steepening of the power law. Since Klypin et al. (2011) and Vogelsberger et al. (2014) fit a modified Press–Schechter functional form to their MFs, they do not provide equivalent values for their slopes. However, we have estimated the MF slopes for both Bolshoi and

Illustris within a mass range of $(10^9\text{--}10^{13}) h^{-1}M_{\odot}$ and found them to be in agreement with our results.

2.3.2 Subhaloes

We next look at the MFs of the subhaloes, shown in Fig. 2.2(b). We measure the power-law slopes of the MFs over a mass range defined by the completeness limit at the low-mass end and $10^{12}M_{\odot}$ at the high-mass end. The upper limit here is lower than the one used for distinct haloes in keeping with the requirement of a maximum relative error of 10%. The results of the fits are provided in Fig. 2.3 as well as Table 2.3 in the appendix.

We find that the low-mass completeness limits set for the distinct haloes remain applicable for the subhaloes as well. The shapes of the MFs are qualitatively the same as the ones for the distinct haloes – they obey power-law relations up to the upper mass limit used for the model fit. The turn-over at the high-mass end does appear to be at a lower mass than in the case of the distinct haloes. At each resolution, the AHF MFs have slopes that are systematically shallower and consistently lower normalizations as compared to the ROCKSTAR results indicating that AHF detects slightly fewer low-mass subhaloes. Setting aside the low-resolution run, for a single halo finder, the two higher resolution runs have statistically identical MFs, although the best-fitting values for the slopes are consistently shallower and the best-fitting normalizations are lower in the mid-resolution run than in the high-resolution run.

In order to compare the slopes of the subhalo MFs and distinct halo MFs, we first remove the obvious differences stemming from their normalizations. We normalize the power-law fit to the distinct halo MF in Fig. 2.2(a) at $M = 10^{10.5}M_{\odot}$ to match the corresponding value of the subhalo MF. The differences between the subhalo MFs and the renormalized distinct halo MF fits for the high-resolution run are plotted in Fig. 2.2(c). The dashed lines show the difference between the subhalo MF fits and the renormalized distinct halo MF fits. Fig. 2.2(c) shows that the subhalo MFs are shallower than the distinct halo MFs, although the difference is more pronounced in the case of AHF than in ROCKSTAR. This may be expected as more massive subhaloes have higher density peaks that can be distinguished more easily from the background halo density profile, making them easier to detect than lower mass subhaloes.

2.3.3 Dependence on parent mass

Since the parent haloes cover a large mass range, it is possible that the results found above could vary with parent halo mass. We look at the same MFs separated into bins of parent halo mass $M_{\text{parent}} = 10^{12.5}\text{--}10^{13}$, $10^{13}\text{--}10^{14}$ and $10^{14}\text{--}10^{15}M_{\odot}$. The numbers of subhaloes in each bin for the high-resolution simulation are given in Table 2.1. The bin widths were chosen to have comparable numbers of subhaloes in each bin as well as representing different environments. The lowest parent-mass bin might represent a poor group or a large galaxy with a population of dwarfs around it; the intermediate bin might represent a group of a few to a few tens of bright galaxies; the highest parent-mass bin would represent a cluster of galaxies. As before, we fit power-law models within a mass range defined by the completeness limits and $10^{11.25}M_{\odot}$. The results of the fits are shown in Fig. 2.3 (there were too few points within this mass range in the low-resolution run to calculate a good fit, which is why it is excluded from these fits).

As with the total subhalo sample, the MF slopes at both resolutions agree within 1σ for both halo finders separately, although the best-fitting slopes for the mid-resolution run are systematically shallower than the ones for the high-resolution run. The AHF slopes are systematically shallower and normalizations lower than ROCKSTAR. The normalizations increase steadily with parent halo mass which is to be expected as more massive host haloes should contain more substructure. Crucially, the slopes are identical in all three environments when controlling for resolution and halo finder. Thus, we find no significant effect of environment on the subhalo MFs. For completeness, we provide the MFs in different parent-mass bins and comparisons to the distinct halo MF in Fig. 2.11 in the appendix.

2.4 Radial distributions of subhaloes

While the MFs of subhaloes detected by both halo finders appear to be consistent, environmental effects on the subhaloes will depend on their radial position within the parent halo. For the remainder of the paper, we focus only on the highest resolution run. Fig. 2.4(a) shows the stacked radial distribution (3D) of the subhaloes. The sample is broken up into bins of $\log(M_{\text{subhalo}})$, shown as different linestyles in the figure. The distance of each subhalo from the centre of the parent halo is normalized by

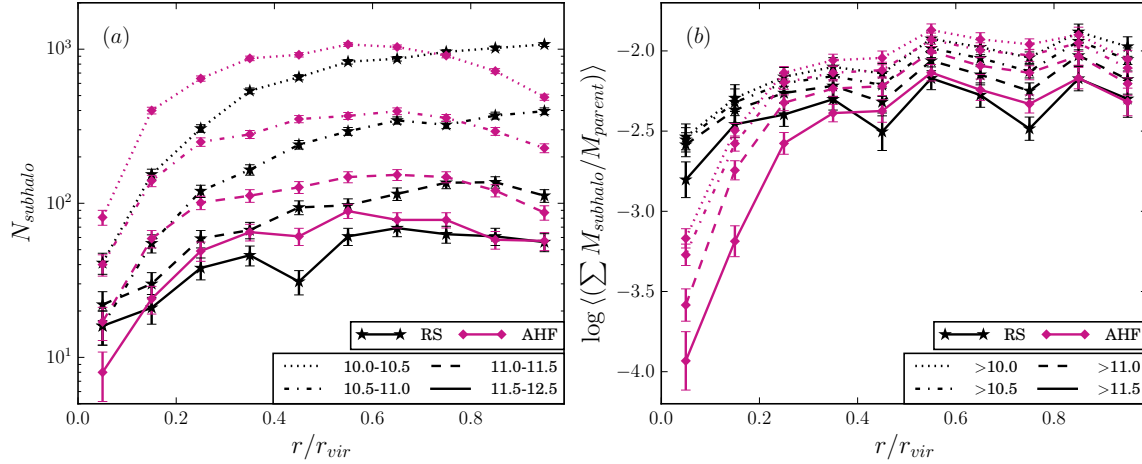


Figure 2.4: (a): Stacked numbers of subhaloes in bins of radial separation from the centre of the parent halo. The different linestyles correspond to different bins of $\log M_{\text{subhalo}}/M_{\odot}$ while the colours correspond to the two halo finders used as in previous figures. AHF and ROCKSTAR produce different radial trends, with AHF generally finding more subhaloes within $\sim 0.7 r_{\text{vir}}$ at all subhalo masses except in the innermost radial bin. The effect is largest in the lower subhalo mass bins. (b): Fractional subhalo mass versus radial distance from parent halo centre, averaged by the total number of parent haloes. The linestyles again represent bins of $\log M_{\text{subhalo}}/M_{\odot}$; here they all have the same upper limit of $M_{\text{subhalo}} = 10^{12.5} M_{\odot}$ while the lower limit is gradually changed to show the contribution of lower mass subhaloes. Low-mass haloes contribute very little to the total subhalo mass within the host, which is why in the inner $\sim 0.5 r_{\text{vir}}$, ROCKSTAR assigns more mass to subhaloes than AHF does even though this mass comes from fewer subhaloes.

the virial radius of the parent halo so that equal weighting is given to both high-mass and low-mass parent haloes. From Fig. 2.4(a), it is clear that although the subhalo populations selected by both halo finders appeared similar in their mass distributions, their radial distributions are quite different. Despite not using velocity information, AHF surprisingly finds many more subhaloes than ROCKSTAR within $0.7 r_{\text{vir}}$. The only place this trend is reversed is in the innermost radial bin in the two higher subhalo mass bins.

Fig. 2.4(b) shows the radial profile of the total fractional mass in subhaloes (i.e. $M_{\text{subhalo}}/M_{\text{parent}}$), normalized by the total number of parent haloes. The different linestyles here represent bins of $\log M_{\text{subhalo}}$ that have the same upper limit of $10^{12.5} M_{\odot}$ while the lower limit is gradually changed in order to show the contribution of lower mass subhaloes. Fig. 2.4(b) shows that within $\sim 0.5 r_{\text{vir}}$ ROCKSTAR assigns more mass to the subhaloes than AHF does (nearly an order of magnitude higher in the first radial bin). Even though ROCKSTAR detects fewer subhaloes in the inner regions, they appear to represent a larger *fraction* of the mass within their parent haloes. This is a result of the fact that although the low-mass subhaloes dominate the number of subhaloes, they do not make up much of the total mass in subhaloes. Knebe et al. (2011) found that close to the halo centre, only phase-space halo finders like ROCKSTAR could detect subhaloes at all, though they also tended to overestimate or underestimate the mass in the subhalo. This may explain why ROCKSTAR assigns more mass to subhaloes near the centre in our results, although it contradicts the larger numbers of subhaloes found by AHF near the centre.

We also explored the dependence of these results on the host mass and found similar results as those of the total sample. AHF found more subhaloes than ROCKSTAR in the inner regions though the differences are more pronounced as the mass of the parent haloes increases. The fractional mass in subhaloes is higher for ROCKSTAR than AHF in the lowest parent-mass bin but the trend appears to reverse in the highest parent-mass bin; these results are dominated by the most massive subhaloes. Radial profiles of the numbers of subhaloes and their fractional mass in bins of parent halo mass are shown in Fig. 2.12 in the appendix.

Fig. 2.4 shows that the two halo finders detect significantly different radial distributions of subhaloes. There are two possible interpretations of these results – either the two halo finders detect different satellite populations altogether or the designation of ‘subhalo’ selects different subsets of the true satellite population. The latter would

mean that the ‘subhalo’ designation is insufficient to select a sample of satellites that would match an observed galaxy population. In the next section, we therefore explore different selection criteria to construct a more representative sample of satellites.

2.5 Galaxy analogues

It is clear that the subhalo populations identified by the two halo finders show differences in their radial distributions, yet the global MFs are in agreement. One of the reasons for this may be that by only selecting subhaloes, we are neglecting the deeper levels in the subhalo hierarchy, i.e. several of the subhaloes have subsubhaloes of their own that could host galaxies. Additionally, in observational studies, analysis is carried out on visible galaxies whereas the simulated dark-matter subhaloes could host 0, 1 or multiple galaxies. Therefore, it is important to select the right haloes in order to be consistent with observational results. To do this, we employ a simple method of selecting such a population of ‘galaxy analogues’ (hereafter referred to as just ‘analogues’).

Our main selection criterion for analogues is mass; a halo is only eligible to be a galaxy analogue if its mass lies within the range of $M_{\text{vir}} = [10^{10}, 10^{12.5}M_{\odot}]$, which would roughly correspond to a stellar mass of $M_{*} = [10^{8.5}, 10^{11}]M_{\odot}$ based on the $M_h - M_{*}$ relations in [Hudson et al. \(2015\)](#). However, a simple mass cut is insufficient since there may be cases where both a halo and its subhaloes meet this criterion, in which case we need to examine whether both are likely to host galaxies. We assign levels to each halo based on its position in the subhalo hierarchy – distinct haloes are designated level 0, subhaloes level 1, subsubhaloes level 2 etc. We then start with a distinct halo and work through its subhalo hierarchy. Any candidate for an analogue is put through the following selection criteria. The ‘halo’ here can be at any level in the hierarchy.

1. If $M_{\text{vir}} < 10^{10}M_{\odot}$, then the halo and its subsequent branches in the hierarchy are eliminated.
2. If $M_{\text{vir}} \geq 10^{12.5}M_{\odot}$, then the halo itself is ignored, but each of its subhaloes is considered as an analogue candidate and put through these same selection criteria.

3. If the halo has a mass $10^{10} < M_{\text{vir}} < 10^{12.5}M_{\odot}$ and either has no subhaloes or all of its subhaloes have masses $M_{\text{vir}} < 10^{10}M_{\odot}$, then the halo is included as an analogue while its subsequent branches are eliminated.
4. If the halo has a mass $10^{10} < M_{\text{vir}} < 10^{12.5}M_{\odot}$ and at least one of its subhaloes has a mass $M_{\text{vir}} > 10^{10}M_{\odot}$, then we first look at the excess mass it contains after subtracting off the masses of *all* of its subhaloes (not just the ones that meet the mass criteria). If this excess mass is also within the valid range, then the halo is included as an analogue and each of its subhaloes is also considered as an analogue candidate.

Effectively, if we have a system in which a halo (at any level) and one or more of its subhaloes both meet the mass criterion, then the final step means that in a limited number of cases, we keep both the halo as well as its subhaloes. Once the analogue population has been identified, we select analogues within $3r_{\text{vir}}$ of every parent halo centre. The numbers of analogues identified by both halo finders in various parent-halo mass ranges are provided in Table 2.1.

The distribution of the final analogue population is shown in Fig. 2.5. The two top panels are identical to Fig. 2.4, only now showing analogues instead of subhaloes. The distributions of the total numbers of analogues from both halo finders are in much better agreement using this selection strategy. The bottom two panels are 2D histograms of the analogues with radial distance from the parent halo centre on the x-axis and subhalo level on the y-axis. It is clear from Fig. 2.5 (c) and (d) that the analogues selected represent much deeper levels of the subhalo hierarchy in the ROCKSTAR catalogue than in the AHF one. Crucially, some of the analogues selected here are at much deeper levels than what would be included by a ‘subhalo’ or ‘subsubhalo’ designation. We also examined these trends in the three different parent-mass bins and the results are included in Fig. 2.13 in the appendix. We find that the results from both halo finders also agree well within all three environments, except possibly in the innermost radial bins in the lowest parent mass bin. Again, the ROCKSTAR analogues represent deeper levels of the subhalo hierarchy as compared to the AHF ones in all three environments.

In Fig. 2.6, we show an example system with mass $M_{\text{vir}} = 2.9 \times 10^{13}M_{\odot}$, to explicitly compare the subhalo hierarchies. In the top panels, we plot the particles within $1.5r_{\text{vir}}$. Ignoring any (sub)subhaloes with $M_{\text{vir}} < 10^{10}M_{\odot}$, we plot the subhaloes in

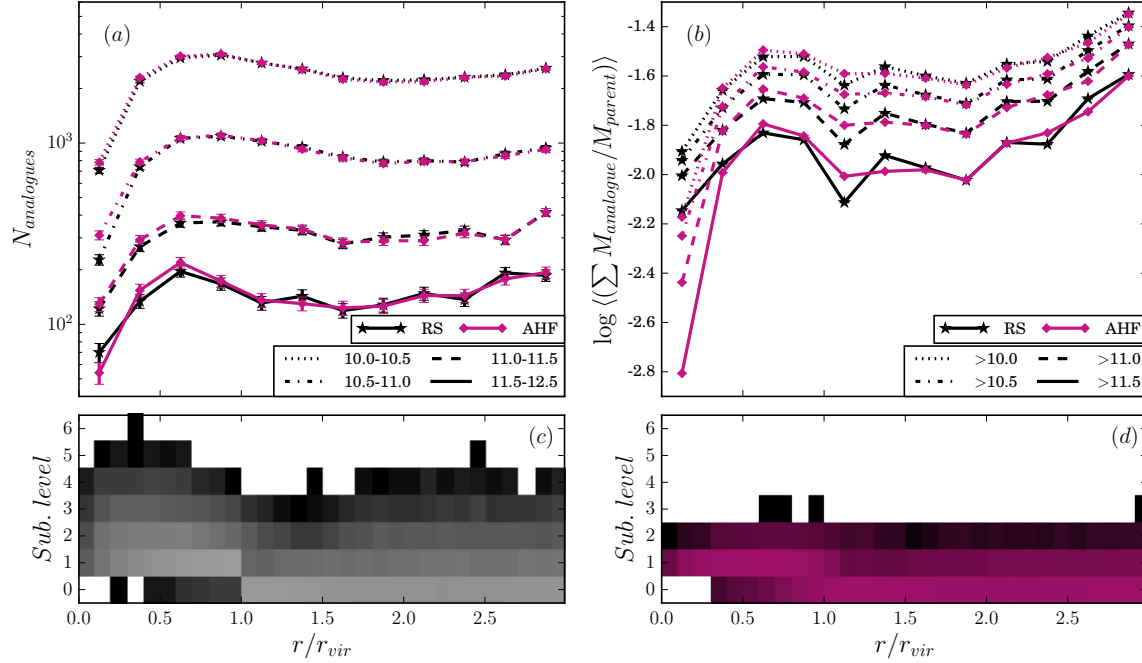


Figure 2.5: (a): Stacked numbers of analogues in bins of radial separation from parent halo centre. The linestyles correspond to different bins of $\log M_{\text{analogue}}/M_{\odot}$ while the colours correspond to the two halo finders as in Fig. 2.4. (b): Fractional analogue mass versus radial separation from parent halo center, averaged by the total number of parent haloes. The selection criteria for analogues ensure that we select the same population not only in terms of mass, but also in terms of radial distribution, although within $\sim 0.5 r_{\text{vir}}$, ROCKSTAR still assigns more mass to subhaloes than AHF does. (c) & (d) 2D histograms of radial distance between analogues and the centre of the parent halo on the x -axis and subhalo level on the y -axis. (Distinct haloes are level 0, subhaloes level 1, subsubhaloes level 2 etc.). For (c) & (d), brighter colours indicate higher numbers with black corresponding to a single halo and the brightest gray in (c) and the brightest pink in (d) corresponding to 1675 and 1680 analogues respectively. The colour maps are logarithmic and continuous with a range of $1 - 10^4$ analogues. While the same population can be selected consistently from either halo catalogue, the analogues can be at very different levels in the subhalo hierarchy. ROCKSTAR identifies many more levels of subhaloes than AHF.

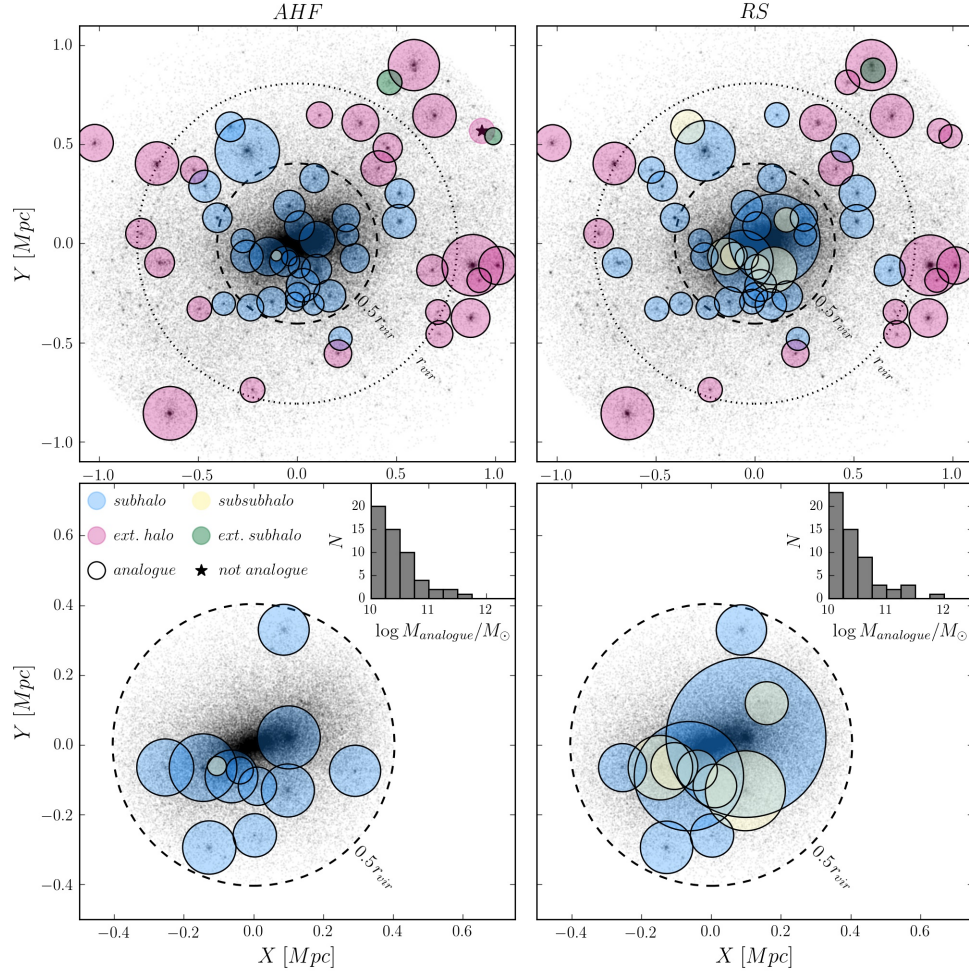


Figure 2.6: Comparing (sub)subhaloes and analogues identified by AHF (left) and ROCKSTAR (right) for an example system with mass $M_{\text{vir}} = 2.9 \times 10^{13} M_{\odot}$. Top: particles within $1.5 r_{\text{vir}}$ from the parent halo centre are plotted as black points (we only plot every fifth particle for clarity). r_{vir} for the host haloes is shown by the black dotted circle, $0.5 r_{\text{vir}}$ by the black dashed circle. Coloured circles show the satellites around the halo - subhaloes of the main parent halo are shown in blue, subsubhaloes in yellow; distinct haloes around the main parent halo within $1.5 r_{\text{vir}}$ are shown in red while their subhaloes are shown in green. The radii of the circles match their virial radii. We only show (sub)subhaloes with $M_{\text{vir}} > 10^{10} M_{\odot}$ here. All analogues identified for the system within $1.5 r_{\text{vir}}$ are shown by the solid black circles. Nearly all of the satellites were selected as analogues. The one exception in the case of AHF is shown by the star symbol. Bottom: zooming in on the inner $0.5 r_{\text{vir}}$. The insets also show the MF of the total analogue population within $1.5 r_{\text{vir}}$. While the sets of subhaloes and subsubhaloes from both halo finders are different, the analogue populations are more consistent, although within $0.5 r_{\text{vir}}$ even analogue populations look different. The figures show that a selection based solely on ‘subhalo’ designations would result in several analogues being missed.

blue and subsubhaloes in yellow. We also show in red other distinct haloes within $1.5 r_{\text{vir}}$ of the parent halo centre and their subhaloes in green. We refer to all four sets collectively as ‘satellites’. We plot *all* analogues within $1.5 r_{\text{vir}}$ as black open circles, so that any satellite outlined in black is also an analogue. For both AHF and ROCKSTAR, all but one of the satellites were also analogues. The one satellite that was not included in the AHF case is designated by the star symbol. In the bottom panels we focus on the inner $0.5 r_{\text{vir}}$. The insets also show the MF of the analogues. Fig. 2.6 shows how several subhaloes that are designated as ‘subhaloes’ by AHF are considered ‘subsubhaloes’ by ROCKSTAR while also being ‘galaxy analogues’. A selection based on subhalo designations alone would therefore miss significant portions of the analogue population.

Figs. 2.5 and 2.6 confirm that while the sets of subhaloes and subsubhaloes are different between the two halo finders, the analogue populations are consistent with one another outside $\sim 0.5 r_{\text{vir}}$. AHF appears more likely to break up nearby overdensities into distinct subhaloes at a shallower level, while ROCKSTAR is more likely to group them into a bigger subhalo and then assign them as subsubhaloes at a deeper level. Therefore, we find that even without using velocity information, a halo finder like AHF can detect most of the haloes of interest outside $\sim 0.5 r_{\text{vir}}$ as well as a halo finder like ROCKSTAR can. In the inner regions however, phase-space information is crucial in being able to separate substructure from the main host halo as was found by previous studies such as Knebe et al. (2011).

2.6 Mass segregation

With the analogue population identified, we are able to examine whether we see any mass segregation trends in the host haloes. Given that phase-space information appears to be important in identifying analogues in the inner regions of parent haloes, we focus on the ROCKSTAR results here. Fig. 2.7(a) shows the radial profile of average analogue mass. The different colours and linestyles represent bins of $\log M_{\text{analogue}}$ where the upper limit is always 12.5 (the mass cut off for selecting analogues) while the lower limit is varied to explore the effect of including low-mass haloes. Fig. 2.7(b) shows the average radial profile of analogue mass as a fraction of the mass of its host halo. As seen in Fig. 2.7(a), the mass profile is remarkably flat over most of the

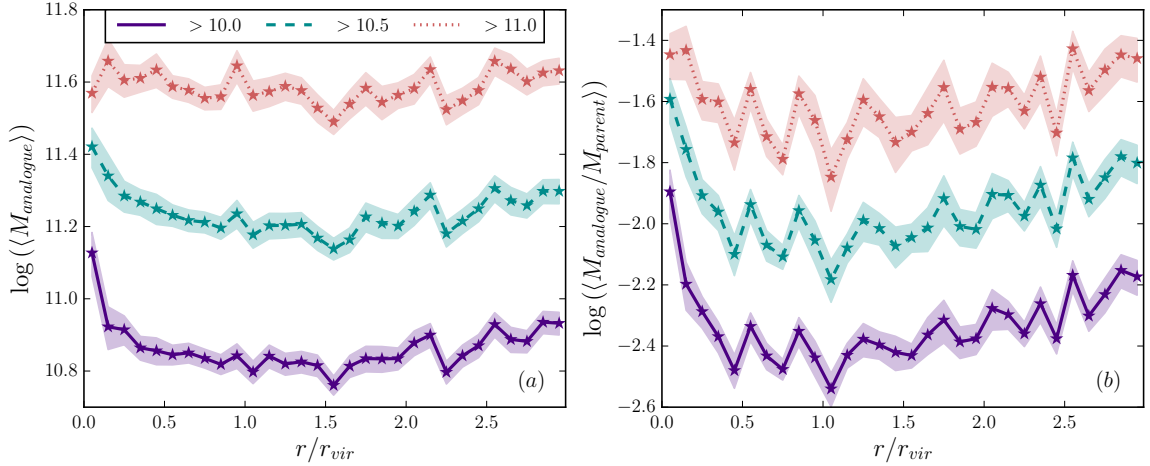


Figure 2.7: Radial trends in average analogue mass (left) and average fractional analogue mass (right) in mass bins of $\log(M_{\text{analogue}}/M_{\odot})$, as shown by the different colours and linestyles. The bins have the same upper limit of $M_{\text{analogue}} = 10^{12.5}M_{\odot}$ while the lower limit is gradually changed to show the effect of including lower mass haloes in detecting mass segregation trends. Errors shown are standard errors on the mean. Within $0.5 r_{\text{vir}}$ we find a weak trend with average mass decreasing with radius. There is also a milder trend outside r_{vir} with average mass increasing with radius. The trends are sensitive to the lower mass limit applied to the sample – they are stronger when low-mass analogues are included (purple solid line and green dashed line). The trends are also more prominent when looking at fractional mass, again only within $0.5 r_{\text{vir}}$.

$3 r_{\text{vir}}$ considered here and any significant mass segregation trend is confined to within $\sim 0.5 r_{\text{vir}}$.

Linear models of the form $\log(M_{\text{analogue}}) = a_1(r/r_{\text{vir}}) + b_1$ and $\log(M_{\text{analogue}}/M_{\text{parent}}) = a_2(r/r_{\text{vir}}) + b_2$ were fit to the radial profiles from $(0-0.5)r_{\text{vir}}$, $(0.5-1)r_{\text{vir}}$ and $(1-3)r_{\text{vir}}$ separately. The results of the fits are given in Table 2.2 (we focus on the fits for the total mass range of analogues, which corresponds to the solid purple lines in Fig. 2.7). The average mass decreases with distance in the inner $0.5 r_{\text{vir}}$, rises with distance beyond r_{vir} and is nearly constant between $(0.5$ and $1)r_{\text{vir}}$ with a minimum at $\sim r_{\text{vir}}$. We find a slope a_1 of -0.5 ± 0.2 within $0.5 r_{\text{vir}}$, -0.05 ± 0.04 between $(0.5$ and $1)r_{\text{vir}}$ and $+0.06 \pm 0.01$ between $(1$ and $3)r_{\text{vir}}$. The trends are stronger when we consider fractional mass instead of absolute mass as seen in Fig. 2.7(b). The corresponding slopes a_2 are -1.3 ± 0.2 within $0.5 r_{\text{vir}}$, -0.1 ± 0.2 between $(0.5$ and $1)r_{\text{vir}}$ and $+0.14 \pm 0.02$ between $(1$ and $3)r_{\text{vir}}$.

Another effect evident in Fig. 2.7(a) is that the radial trends in mean absolute mass seen at small radii are stronger when we include low mass analogues in our analysis. If we consider only high-mass analogues, the results are consistent with having no trend with radius. Thus, the higher mass substructure does not appear to have a preferred position within the parent halo. Any segregation trend is instead due to the low-mass substructure. Note that since we are looking at the average mass, these results are not due to having a larger volume at large radii but due to intrinsic variations of the analogue population with radial distance. In observational studies, due to detection constraints, low-mass galaxies are often not included in order to have a luminosity- or mass-complete sample. Our results suggest that this can have a significant impact on whether mass segregation is detected.

We also examine these mass segregation trends separating by parent halo mass to explore any environmental dependence. Fig. 2.8 shows the same radial trends in average mass (top panels) and average fractional mass (bottom panels), now separated by environment. Results of linear fits to the profiles for the complete mass range of analogues (purple solid lines) are given in Table 2.2. Outside $0.5 r_{\text{vir}}$, the results are qualitatively in agreement with what we find for the total population – outside r_{vir} there is a mild increase in average (fractional) mass with distance; between $(0.5$ and $1)r_{\text{vir}}$, the average fractional mass profiles are consistent with having no slope while we find mild slopes in the average absolute mass in the two lower-parent-mass bins. Within $0.5 r_{\text{vir}}$ however, we do find significant differences based on environment. In

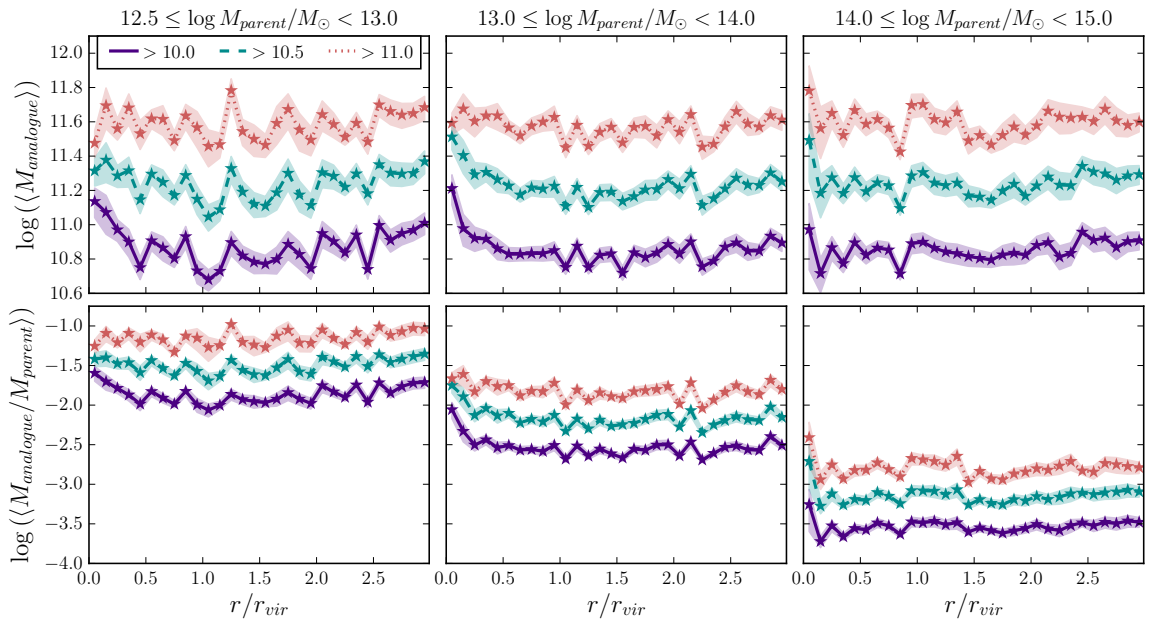


Figure 2.8: Radial trends in average analogue mass (top) and average fractional analogue mass (bottom) as in Fig. 2.7, but separated by environment. As with the total sample, we see a weak trend of average mass decreasing with radius within $0.5 r_{\text{vir}}$, though only in the low- and intermediate-parent mass systems and only when we include lower mass analogues down to a mass of at least $10^{10.5} M_{\odot}$. Most importantly, the trends get weaker with increasing parent halo mass.

Table 2.2: Results of linear fits to mass segregation trends from the ROCKSTAR results including analogues of all masses (purple solid lines in Figs. 2.7 and 2.8). For the average mass profile, the fit is of the form: $\log(M_{\text{analogue}}) = [a_1 (r/r_{\text{vir}}) + b_1]$. For the average fractional mass profile, the fit is of the form $\log(M_{\text{analogue}}/M_{\text{parent}}) = [a_2 (r/r_{\text{vir}}) + b_2]$. All uncertainties are standard errors on regression coefficients. Non-zero slopes are shown in bold.

Subset	a_1	b_1	a_2	b_2
$r/r_{\text{vir}} < 0.5$				
All analogues	-0.54 ± 0.18	11.07 ± 0.06	-1.28 ± 0.22	-1.93 ± 0.07
$10^{12.5} \leq M_{\text{par}} < 10^{13} M_{\odot}$	-0.96 ± 0.08	11.20 ± 0.03	-0.95 ± 0.04	-1.55 ± 0.01
$10^{13} \leq M_{\text{par}} < 10^{14} M_{\odot}$	-0.71 ± 0.22	11.16 ± 0.07	-0.96 ± 0.38	-2.14 ± 0.12
$10^{14} \leq M_{\text{par}} < 10^{15} M_{\odot}$	$+0.18 \pm 0.36$	10.77 ± 0.12	$+0.17 \pm 0.43$	-3.67 ± 0.15
$0.5 < r/r_{\text{vir}} < 1$				
All analogues	-0.05 ± 0.04	10.87 ± 0.03	-0.12 ± 0.25	-2.32 ± 0.19
$10^{12.5} \leq M_{\text{par}} < 10^{13} M_{\odot}$	-0.27 ± 0.24	11.05 ± 0.18	-0.20 ± 0.32	-1.76 ± 0.24
$10^{13} \leq M_{\text{par}} < 10^{14} M_{\odot}$	$+0.04 \pm 0.02$	10.80 ± 0.01	-0.04 ± 0.13	-2.52 ± 0.10
$10^{14} \leq M_{\text{par}} < 10^{15} M_{\odot}$	-0.16 ± 0.30	10.93 ± 0.23	-0.00 ± 0.25	-3.55 ± 0.19
$1 < r/r_{\text{vir}} < 3$				
All analogues	$+0.06 \pm 0.01$	10.72 ± 0.03	$+0.14 \pm 0.02$	-2.62 ± 0.04
$10^{12.5} \leq M_{\text{par}} < 10^{13} M_{\odot}$	$+0.12 \pm 0.03$	10.61 ± 0.06	$+0.13 \pm 0.03$	-2.14 ± 0.06
$10^{13} \leq M_{\text{par}} < 10^{14} M_{\odot}$	$+0.05 \pm 0.02$	10.72 ± 0.04	$+0.05 \pm 0.03$	-2.69 ± 0.06
$10^{14} \leq M_{\text{par}} < 10^{15} M_{\odot}$	$+0.04 \pm 0.02$	10.77 ± 0.03	$+0.03 \pm 0.02$	-3.59 ± 0.04

the highest parent-mass bin, both the average absolute mass and fractional mass profiles are consistent with being flat, whereas we find significant segregation in the two lower parent-mass bins. In all cases, regardless of whether we consider absolute mass or fractional mass and within all three radial regions, the trends are strongest in the least massive systems and weakest in the most massive ones.

2.7 Discussion

2.7.1 Detecting substructure

In this work, we have examined the ability of AHF and ROCKSTAR to detect substructure within groups and clusters in dark matter simulations. The resulting MFs of distinct haloes they find are consistent with each other, while the subhalo MFs show significant differences. The largest differences however are seen in the radial distributions of the subhaloes. Counter-intuitively, AHF detects many more ‘subhaloes’ within the mass range of interest than ROCKSTAR. This shows the sensitivity of these halo finders to various numerical choices. However, as we have shown, outside $0.5 r_{\text{vir}}$, both halo finders are capable of detecting consistent populations of substructure as long as care is taken in selecting ‘galaxy analogue’ populations rather than ‘subhalo’ populations. This is due to the differences in the subhalo hierarchies built by each halo finder whereby the same galaxy analogue could be at different levels within the hierarchy and crucially, deeper than a ‘subhalo’ or even ‘subsubhalo’.

Note that the haloes detected by ROCKSTAR are not necessarily spherical due to the nature of an FOF algorithm. While this is less of an issue for distinct haloes, it does become important for subhaloes embedded in a dense environment. Regions that are spatially distant may be connected into one large structure in phase space which is why the ‘subhalo’ designation was insufficient in our study, since the haloes of interest to us were embedded at deeper levels in the subhalo hierarchy. Studies that select subhalo populations solely based on this designation would therefore miss a significant portion of the true ‘galaxy’ population and instead, select larger numbers of massive haloes relative to the low-mass ones.

The selection criteria used to identify galaxy analogues resulted in a small number of cases ($\sim 5\%$) where both a halo and its subhaloes (at any level in the hierarchy) were both included in the analogue population. Since subhalo particles within the

virial radius of the parent halo are included by both halo finders when calculating halo properties, this may result in part of the subhalo mass being included twice. Although we do not account for this in the results presented in previous sections, we repeated the same analysis after subtracting the mass in subhaloes in the small number of cases where this was relevant and only using the remaining mass. Since the volumes enclosed by the virial radii of the subhaloes can partially overlap each other, this was not an ideal solution; however it was a lower limit on the mass of these haloes, whereas our previous results represent an upper limit, and the two results are not significantly different.

2.7.2 Mass segregation

We used the analogue population to examine mass segregation trends in dense environments. Firstly, in the average mass profiles shown in Fig. 2.7(a), we find statistically significant trends within $0.5 r_{\text{vir}}$ (with average mass decreasing with distance) and beyond r_{vir} (with average mass rising with distance) for the total population, but only when we include low-mass analogues. As seen in Fig. 2.7(a) (pink dotted lines), massive analogues do not appear to preferentially live near the centres of their host haloes. Separating by parent-mass, we find no mass segregation in the most massive systems, which correspond to galaxy clusters, while in less massive systems we find mild to moderate segregation. The strength of the segregation signal appears to be anti-correlated with the mass of the parent halo.

In the average mass profiles for the total population shown in Fig. 2.7(b), the segregation trends are stronger and present in all three ranges of analogue mass under consideration. It is important to reconcile this with the trends in the lower panels of Fig. 2.8 which appear to be shallower in comparison, especially for higher mass analogues (pink dotted lines). Each line in Fig. 2.7(b) is a weighted sum of the corresponding lines in the three lower panels of Fig. 2.8 with the weights equal to the fraction of analogues contributed by each parent-mass bin to each radial bin. We found that for all three ranges of analogue mass, beyond $0.5 r_{\text{vir}}$ the largest contribution comes from the intermediate parent-mass bin. However, the contribution from the lowest parent-mass bin rises steadily with radius while the highest parent-mass bin decreases with radius. Since the absolute mass range of analogues represents a different fraction of the parent mass in each of the three systems, even if the trends in each parent mass bin had been flat, the average fractional mass profile would show

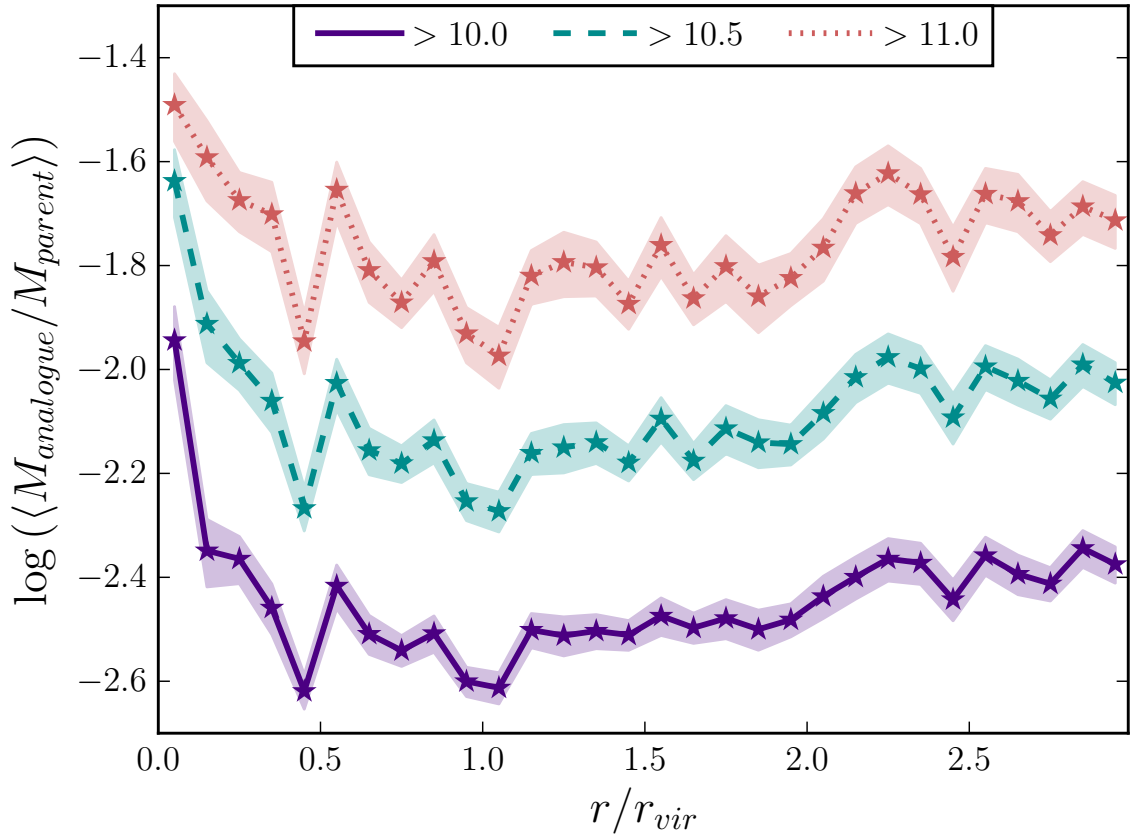


Figure 2.9: Radial trends in average fractional analogue mass as in Fig. 2.7(b) but while excluding the most massive analogues (with mass $10^{12} - 10^{12.5}M_{\odot}$) to reduce stochastic scatter and show mass segregation more clearly.

a gradual increase with radius as the lowest parent-mass bin would be weighted more and more heavily. The opposite is true within $0.5r_{\text{vir}}$ where the contribution from the lowest parent-mass bin rises sharply towards the centre and that from the highest parent-mass bin drops significantly; this effect is partly due to fewer analogues overall near the centres of the parent haloes. Any trends in the fractional mass profile in the lowest parent-mass bin are therefore amplified in the profile for the total sample.

The radial profiles shown in Fig. 2.7(b) are also somewhat noisy making it difficult to discern any trends. We have investigated the source of this noise and found that it is due to the inclusion of the most massive analogues, with $M_{\text{analogue}} > 10^{12}M_{\odot}$; due to low numbers, they appear stochastically in some radial bins. Since they are included in calculating all three lines shown in the figure, they have a large impact on the resultant mass profile. If we exclude these high-mass analogues, the segregation

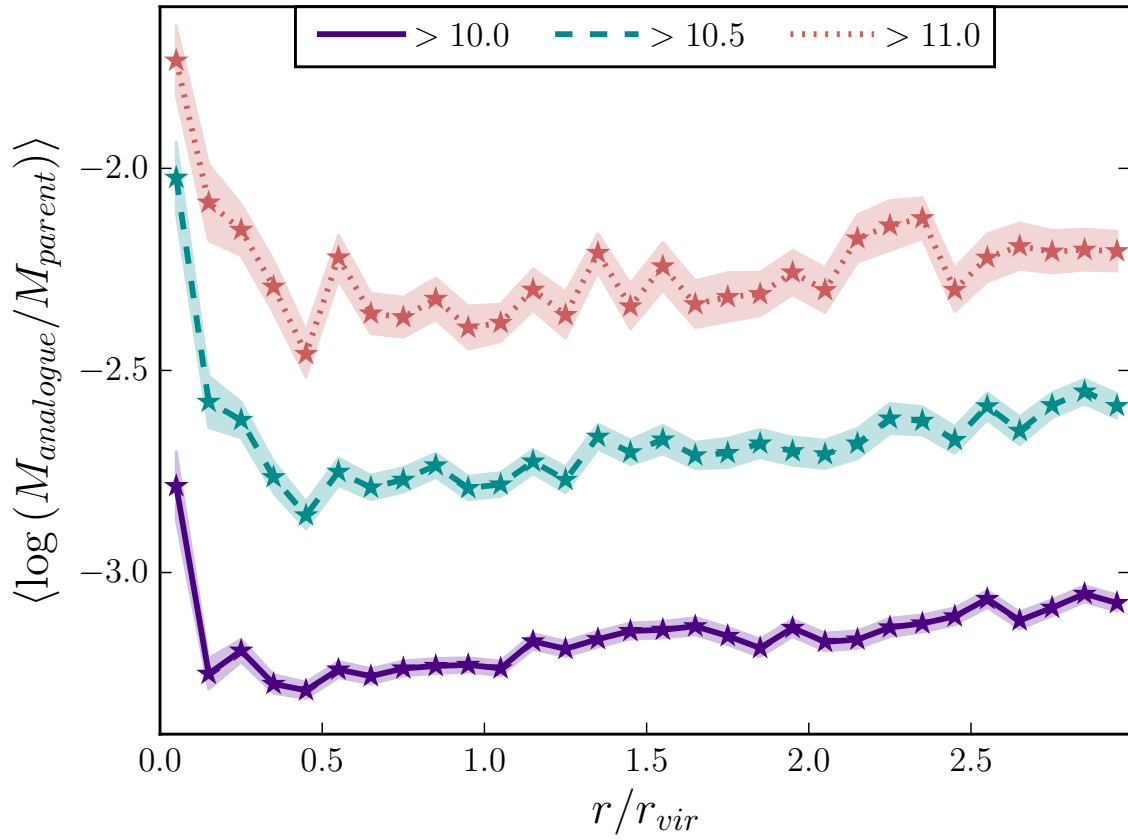


Figure 2.10: Radial trends in average fractional analogue mass as in Fig. 2.7(b) but averaging over $\log(\text{fractional mass})$ rather than (fractional mass) in order to give equal weighting to low mass analogues.

trends are stronger and less noisy as shown in Fig. 2.9. Additionally, in both Figs. 2.7(b) and 2.9, we calculate the average mass of analogues which naturally gives higher weighting to the high-mass analogues. An alternative approach is to average over $\log(M_{\text{analogue}}/M_{\text{parent}})$ thereby weighting high- and low- mass analogues equally. The segregation trends are stronger using this method as shown in Fig. 2.10.

van den Bosch et al. (2016) found a mild *positive* correlation between fractional mass M/M_{host} and 3D separation r/r_{vir} within the virial radius using a Spearman rank-order correlation coefficient. However this indicator of segregation is only meaningful when the correlation between the two quantities is monotonic which was not the case. Accounting for this, they found a weak trend of decreasing mass with increasing radius which is highly sensitive to sample selection. They did however find much stronger and more robust trends when using the mass at accretion $M_{\text{acc}}/M_{\text{host}}$, the peak mass of the subhaloes $M_{\text{peak}}/M_{\text{host}}$ or the mass lost by the subhalo after accretion, quantified by M/M_{acc} as the segregation property. They concluded that the mild segregation in present-day mass is due to a combination of the inside-out assembly of the host haloes resulting in more massive haloes accreted at earlier times being found at smaller radii, dynamical friction causing massive haloes to migrate towards the halo centre, as well as mass-loss due to tidal stripping that acts to negate this segregation. Our results for the total analogue sample are roughly consistent with those of van den Bosch et al. (2016), although when we separate our sample into different parent mass bins we see no trend in the most massive parent haloes. Their subhalo population was defined as haloes whose centres were within r_{vir} of a larger halo, which may more closely resemble our analogue population than a simple ‘direct subhalo’ definition. Note that they excluded subhaloes where $M/M_{\text{host}} < 10^{-3}$ as opposed to a lower absolute mass limit and had additional constraints on $M_{\text{acc}}/M_{\text{host}}$. As the segregation trends in present-day mass were highly sensitive to sample selection, these constraints almost certainly influenced their results.

Contini & Kang (2015) found a clear mass segregation signal of dark-matter subhaloes out to $1R_{\text{vir}}$ and then an upturn in average mass out to $2R_{\text{vir}}$; the upturn was quite sharp in their ‘large groups’ and ‘large clusters’ samples. They considered subhaloes with *stellar* masses greater than $10^{10}M_{\odot}$, which is significantly more massive than the lower mass limit used in this study and the range of host masses they consider only overlap with our two higher parent-mass bins. Our results do support a mild positive mass segregation trend with halo-centric radius beyond a virial radius;

however, the upturn is not as sharp as the one found by [Contini & Kang \(2015\)](#). They found that the segregation trends became weaker with larger host masses which is consistent with our findings.

Our galaxy analogue results agree well with recent observational work by [Roberts et al. \(2015\)](#) who looked at the segregation of galaxy stellar mass using observational data from the SDSS-DR7 group catalogue. Their sample consisted of host haloes with masses $M = (10^{13}–10^{15})M_{\odot}$, which is similar to our sample, and four different lower mass limits in M_* . They found the weakest trends in the most massive groups and the strongest in the least massive ones. They also concluded that the trend gets stronger with the inclusion of lower mass galaxies, consistent with what we see in these dark-matter-only simulations.

There are several factors which could play a role in establishing the trends we detect. Firstly, dynamical friction is one of the main candidates for driving mass segregation by preferentially moving massive analogues towards the centres of their host haloes. The efficiency of dynamical friction is expected to increase with analogue mass, but decrease with parent halo mass ([Chandrasekhar, 1943](#); [Boylan-Kolchin et al., 2008](#)). Secondly, mergers in group and cluster haloes can lead to the creation of more massive analogues which are then subject to dynamical friction. Thirdly, it is important to keep in mind that analogues which were accreted earlier (when the host haloes were smaller and less massive) will preferentially be located at small radii. If more massive analogues are accreted at high redshifts, this scenario can also produce mass segregation. Finally, in addition to mass growth, analogues can also lose mass due to tidal stripping which would result in dynamical friction being less efficient. The mass of an analogue and its position within its host is therefore a complicated combination of accretion time, host halo mass and accretion history, dynamical friction, mergers and stripping.

We have shown that the trends in mass segregation are strongest with the inclusion of low-mass analogues. In fact, there is very little segregation in the most massive analogues, as seen in Figs. [2.7](#) and [2.8](#), implying that they do not have a preferred location within their parent halo. This lack of segregation in massive analogues suggests either that dynamical friction is not the dominant effect at work or that the segregation due to dynamical friction is balanced by the accretion of more massive objects at late times (and therefore at large radii). The segregation trends we observe in low-mass analogues, where dynamical friction is expected to be weak, may

be due to tidal stripping preferentially destroying low-mass objects. However, it is unclear whether tidal stripping can be more efficient for smaller analogues than more massive ones. The low-mass analogue results are consistent with dynamical friction, although they may also be the result of coordinated infall due to the late accretion of smaller groups. The reduction in mass segregation with increasing parent halo mass is consistent with dynamical friction predictions, but the lack of segregation in the most massive analogues suggest that dynamical friction is not the dominant factor in the trends we observe.

It is important to note that we use 3D radial separations throughout this study whereas most observational studies use projected separations. [van den Bosch et al. \(2016\)](#) found that any segregation trends are weaker when using projected separations, which may be the reason for the weaker trends found by observational studies (e.g. [von der Linden et al., 2010](#); [Ziparo et al., 2013](#)). Additionally, we look at segregation in present-day mass, whereas both [van den Bosch et al. \(2016\)](#) and [Contini & Kang \(2015\)](#) also examined mass at accretion which appears to be more strongly segregated. While the stellar mass of galaxies is likely to be correlated with their halo mass at accretion (e.g. [Nagai & Kravtsov, 2005](#)), they can undergo a diverse range of processes within the group/cluster halo that will affect both their present halo mass as well as their current observable properties. The greater segregation at early times also supports a pre-processing scenario where segregation is weaker in massive systems due to the (late) accretion of massive objects, consistent with our results.

2.8 Summary

In this paper, we explore mass segregation trends in groups and clusters using dark-matter-only simulations with two different halo finders: AHF, a 3D spherical overdensity algorithm, and ROCKSTAR, a phase-space FOF algorithm. We compare the performance of the halo finders in detecting substructure by comparing their subhalo MFs and radial distributions.

1. We find that the mass distributions of direct subhaloes of the parent haloes are consistent between the two halo finders. However, their radial distributions are significantly different – in the inner regions of the parent haloes AHF finds more subhaloes whereas ROCKSTAR assigns more mass to them.

2. We then identify a population ‘galaxy analogues’ that would better correspond to observed galaxy populations. The radial distributions of these analogues are in better agreement between the two halo finders although in the inner regions (within $\sim 0.5r_{\text{vir}}$), ROCKSTAR assigns a larger fraction of the parent mass to these analogues than AHF.
3. We find statistically significant mass segregation for the total sample of analogues; within $0.5r_{\text{vir}}$ the mean (fractional) mass decreases with radius while between $(0.5 \text{ and } 1)r_{\text{vir}}$, it shows little variation with radius. Beyond r_{vir} , we find milder positive segregation with mean (fractional) mass increasing with radius.
4. Segregation trends in average absolute mass are stronger when we include low-mass analogues. The trends are also stronger in the lowest parent-mass systems and weaken with increasing parent mass.

Earlier studies have found a much stronger correlation with the mass at accretion or the peak mass of subhaloes with radial separation from the centre which indicates that any mass segregation trends are strongly connected to the accretion histories of the host systems. Therefore, future work must focus on the formation and accretion histories of these analogues to disentangle the various drivers of mass segregation trends in these systems.

Acknowledgements

We thank the anonymous referee for their comments and insights which were very useful in improving the manuscript. We thank the National Science and Engineering Research Council of Canada for their funding. Computations were performed on the *gpc* supercomputer at the SciNet HPC Consortium (Loken et al., 2010). SciNet is funded by: the Canada Foundation for Innovation under the auspices of Compute Canada; the Government of Ontario; Ontario Research Fund – Research Excellence; and the University of Toronto. This work was made possible by the facilities of the Shared Hierarchical Academic Research Computing Network (SHARCNET:www.sharcnet.ca) and Compute Canada.

References

- Abadi M. G., Moore B., Bower R. G., 1999, [MNRAS](#), **308**, 947
- Abazajian K. N., et al., 2009, [ApJS](#), **182**, 543
- Angulo R. E., Lacey C. G., Baugh C. M., Frenk C. S., 2009, [MNRAS](#), **399**, 983
- Balogh M. L., Navarro J. F., Morris S. L., 2000, [ApJ](#), **540**, 113
- Balogh M. L., Baldry I. K., Nichol R., Miller C., Bower R., Glazebrook K., 2004, [ApJ](#), **615**, L101
- Behroozi P. S., Wechsler R. H., Wu H.-Y., 2013, [ApJ](#), **762**, 109
- Blanton M. R., Berlind A. A., 2007, [ApJ](#), **664**, 791
- Blanton M. R., Eisenstein D., Hogg D. W., Schlegel D. J., Brinkmann J., 2005, [ApJ](#), **629**, 143
- Boylan-Kolchin M., Ma C.-P., Quataert E., 2008, [MNRAS](#), **383**, 93
- Bryan G. L., Norman M. L., 1998, [ApJ](#), **495**, 80
- Chandrasekhar S., 1943, [ApJ](#), **97**, 255
- Cole S., Lacey C., 1996, [MNRAS](#), **281**, 716
- Contini E., Kang X., 2015, [MNRAS](#), **453**, L53
- Davis M., Efstathiou G., Frenk C. S., White S. D. M., 1985, [ApJ](#), **292**, 371
- Dressler A., 1980, [ApJ](#), **236**, 351
- Girardi M., Rigoni E., Mardirossian F., Mezzetti M., 2003, [A&A](#), **406**, 403
- Gunn J. E., Gott III J. R., 1972, [ApJ](#), **176**, 1
- Hahn O., Abel T., 2013, MUSIC: MUlti-Scale Initial Conditions, Astrophysics Source Code Library (ascl:1311.011)
- Hogg D. W., et al., 2004, [ApJ](#), **601**, L29

- Hudson M. J., et al., 2015, [MNRAS](#), **447**, 298
- Jetley P., Gioachin F., Mendes C., Kale L., Quinn T., 2008, in *Parallel and Distributed Processing*, 2008. IPDPS 2008. IEEE International Symposium on. pp 1–12, [doi:10.1109/IPDPS.2008.4536319](https://doi.org/10.1109/IPDPS.2008.4536319)
- Jetley P., Wesolowski L., Gioachin F., Kalé L. V., Quinn T. R., 2010, in *Proceedings of the 2010 ACM/IEEE International Conference for High Performance Computing, Networking, Storage and Analysis. SC '10*. IEEE Computer Society, Washington, DC, USA, pp 1–11, [doi:10.1109/SC.2010.49](https://doi.org/10.1109/SC.2010.49), <http://dx.doi.org/10.1109/SC.2010.49>
- Kauffmann G., White S. D. M., Heckman T. M., Ménard B., Brinchmann J., Charlot S., Tremonti C., Brinkmann J., 2004, [MNRAS](#), **353**, 713
- Kawata D., Mulchaey J. S., 2008, [ApJ](#), **672**, L103
- Klypin A., Holtzman J., 1997, *ArXiv Astrophysics e-prints*,
- Klypin A. A., Trujillo-Gomez S., Primack J., 2011, [ApJ](#), **740**, 102
- Knebe A., et al., 2011, [MNRAS](#), **415**, 2293
- Knollmann S. R., Knebe A., 2009, [ApJS](#), **182**, 608
- Lacey C., Cole S., 1994, [MNRAS](#), **271**, 676
- Lares M., Lambas D. G., Sánchez A. G., 2004, [MNRAS](#), **352**, 501
- Larson R. B., Tinsley B. M., Caldwell C. N., 1980, [ApJ](#), **237**, 692
- Loken C., et al., 2010, *Journal of Physics: Conference Series*, **256**, 012026
- Lukić Z., Reed D., Habib S., Heitmann K., 2009, [ApJ](#), **692**, 217
- Makino J., Hut P., 1997, [ApJ](#), **481**, 83
- Menon H., Wesolowski L., Zheng G., Jetley P., Kale L., Quinn T., Governato F., 2015, [Computational Astrophysics and Cosmology](#), **2**, 1
- Moore B., Katz N., Lake G., Dressler A., Oemler A., 1996, [Nature](#), **379**, 613

- Moore B., Lake G., Katz N., 1998, [ApJ](#), 495, 139
- Muldrew S. I., Pearce F. R., Power C., 2011, [MNRAS](#), 410, 2617
- Nagai D., Kravtsov A. V., 2005, [ApJ](#), 618, 557
- Oemler Jr. A., 1974, [ApJ](#), 194, 1
- Onions J., et al., 2012, [MNRAS](#), 423, 1200
- Ostriker J. P., Tremaine S. D., 1975, [ApJ](#), 202, L113
- Planck Collaboration et al., 2014, [A&A](#), 571, A16
- Roberts I. D., Parker L. C., Joshi G. D., Evans F. A., 2015, [MNRAS](#), 448, L1
- Sheth R. K., Tormen G., 2002, [MNRAS](#), 329, 61
- Springel V., White S. D. M., Tormen G., Kauffmann G., 2001, [MNRAS](#), 328, 726
- Springel V., et al., 2008, [MNRAS](#), 391, 1685
- Tremaine S. D., Ostriker J. P., Spitzer Jr. L., 1975, [ApJ](#), 196, 407
- Vogelsberger M., et al., 2014, [MNRAS](#), 444, 1518
- Wetzel A. R., Tinker J. L., Conroy C., 2012, [MNRAS](#), 424, 232
- White S. D. M., 1977, [MNRAS](#), 179, 33
- White M., 2002, [ApJS](#), 143, 241
- Ziparo F., et al., 2013, [MNRAS](#), 434, 3089
- van den Bosch F. C., Pasquali A., Yang X., Mo H. J., Weinmann S., McIntosh D. H., Aquino D., 2008, preprint, ([arXiv:0805.0002](#))
- van den Bosch F. C., Jiang F., Campbell D., Behroozi P., 2016, [MNRAS](#), 455, 158
- von der Linden A., Wild V., Kauffmann G., White S. D. M., Weinmann S., 2010, [MNRAS](#), 404, 1231

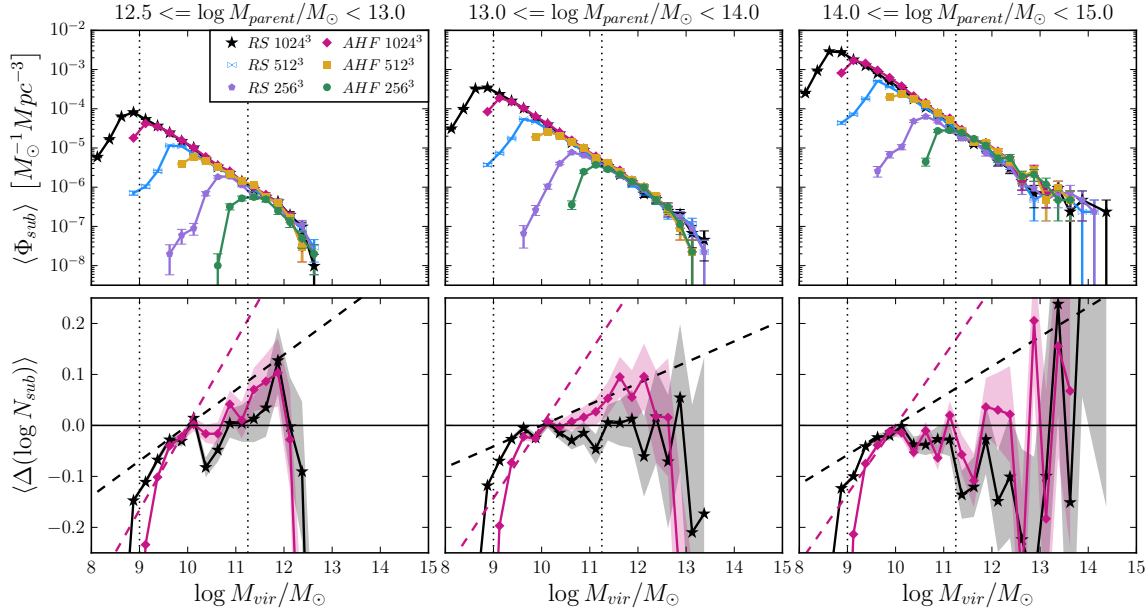


Figure 2.11: Top: MFs and Bottom: differences between subhalo MFs and corresponding distinct halo MFs (as in Fig. 2.2 (b) & (c) above), here separated by parent halo mass and averaged by the number of parent haloes (to remove any differences caused by the different numbers of host haloes in each bin). The distinct halo MFs are normalized at $M = 10^{10}M_{\odot}$ here. For a single resolution and halo finder, the slopes of the MFs in the three bins are identical. However, the MFs for the 512³ run are consistently shallower than the ones for the 1024³ and the AHF MFs are consistently shallower than the ROCKSTAR ones. All these subhalo MFs are also consistently shallower than the corresponding distinct halo MF, although again, the differences for ROCKSTAR are smaller than for AHF.

2.9 Appendices

2.9.1 MFs of subhaloes

Fig. 2.11 shows subhalo MFs (*top panels*) and the differences between the subhalo MFs and corresponding distinct halo MFs (*bottom panels*) as in Fig. 2.2 (b) & (c) here separated into bins of parent halo mass. The results are qualitatively the same as those for the total subhalo sample. Power-law models were fit to these subhalo MFs within a mass range defined by the completeness limit at each resolution and $10^{11.25}M_{\odot}$ – the results are included in Fig. 2.3.

Table 2-3: Results from power-law fits of the form $\log \Phi = a \log M_{\text{vir}} + b$ to the MFs shown in Figs 2.2 and 2.11. We only use data points within a specific range in $\log M_{\text{vir}}$. The lower limit is set by requiring a minimum of 25 particles in each halo, which corresponds to 11, 10 and 9 for the low-, mid- and high-resolutions runs, respectively. The upper limit is set by requiring a maximum relative error of 10%, which corresponds to 13 for the distinct haloes, 12 for the total sample of subhaloes and 11.25 for the binned subhaloes samples.

	ROCKSTAR			AHF		
Subset	256 ³	512 ³	1024 ³	256 ³	512 ³	1024 ³
	Index					
Distinct halos	-0.873 ± 0.009	-0.841 ± 0.008	-0.851 ± 0.004	-0.878 ± 0.010	-0.845 ± 0.009	-0.854 ± 0.006
Subhalos	-0.68 ± 0.07	-0.78 ± 0.01	-0.80 ± 0.01	-0.49 ± 0.09	-0.68 ± 0.03	-0.72 ± 0.03
$M_{\text{par}} : [10^{12.5}, 10^{13}] M_{\odot}$	-	-0.72 ± 0.03	-0.78 ± 0.02	-	-0.60 ± 0.03	-0.69 ± 0.04
$M_{\text{par}} : [10^{13}, 10^{14}] M_{\odot}$	-	-0.77 ± 0.03	-0.81 ± 0.02	-	-0.62 ± 0.06	-0.71 ± 0.04
$M_{\text{par}} : [10^{14}, 10^{15}] M_{\odot}$	-	-0.76 ± 0.02	-0.79 ± 0.02	-	-0.64 ± 0.06	-0.72 ± 0.04
	Normalization					
Distinct halos	8.05 ± 0.11	7.71 ± 0.08	7.85 ± 0.04	8.10 ± 0.12	7.76 ± 0.09	7.89 ± 0.06
Subhalos	4.7 ± 0.8	6.0 ± 0.2	6.3 ± 0.1	2.6 ± 1.0	5.0 ± 0.4	5.6 ± 0.3
$M_{\text{par}} : [10^{12.5}, 10^{13}] M_{\odot}$	-	2.2 ± 0.3	2.9 ± 0.2	-	0.9 ± 0.3	2.0 ± 0.4
$M_{\text{par}} : [10^{13}, 10^{14}] M_{\odot}$	-	3.3 ± 0.3	3.8 ± 0.2	-	1.7 ± 0.6	2.8 ± 0.4
$M_{\text{par}} : [10^{14}, 10^{15}] M_{\odot}$	-	4.1 ± 0.2	4.5 ± 0.2	-	2.8 ± 0.6	3.8 ± 0.4

The results of the power-law fits to the distinct halo MFs, total subhalo MFs and subhalo MFs in bins of parent halo mass depicted in Fig. 2.3 are also provided in Table 2.3.

2.9.2 Radial distributions of subhaloes

Fig. 2.12 shows the radial profiles of the total numbers of subhaloes (*top panels*) and the fractional mass in subhaloes (*bottom panels*) for the highest resolution simulation as in Fig. 2.4, here separated into bins of parent halo mass. The different linestyles represent different bins of $\log M_{\text{subhalo}}$. As with the total subhalo sample, AHF finds more subhaloes in the inner regions at least in the lower subhalo mass bins, although the differences are most pronounced in the highest parent mass bin. However, ROCKSTAR appears to assign more mass to subhaloes in the lowest parent mass bin.

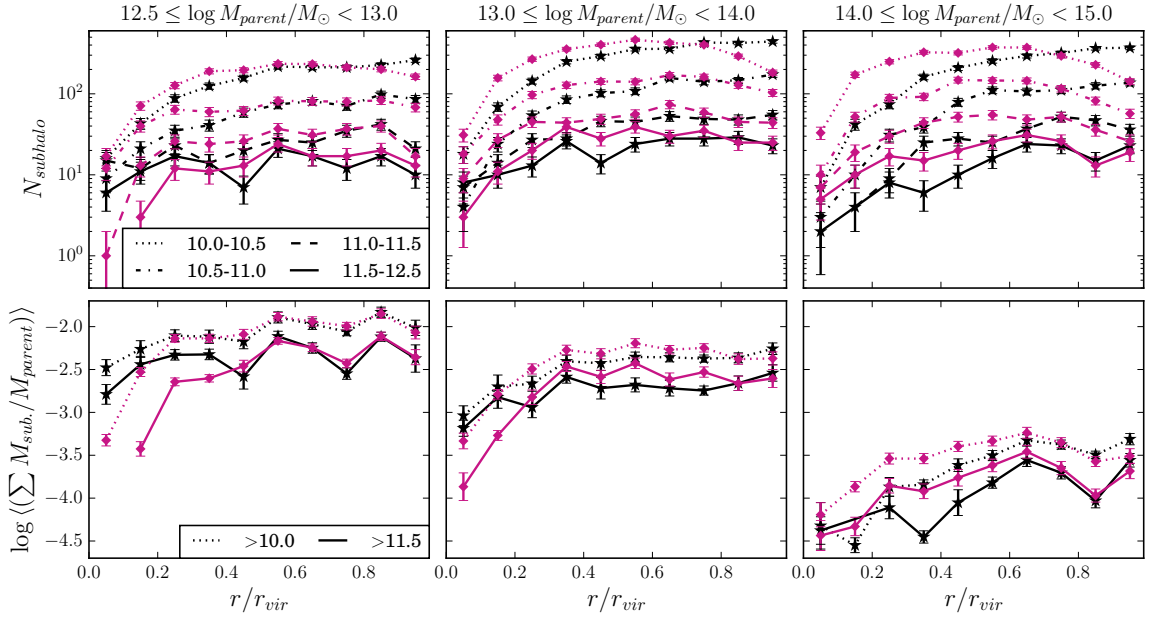


Figure 2.12: Radial profiles of the total numbers of subhaloes (top) and fractional subhalo mass averaged by the number of parent haloes (bottom) as in Fig. 2.4, but separated by parent halo mass (in the bottom panel, we only show the first and last bins for clarity’s sake and since the results in the intermediate bins are similar to the ones shown in Fig. 2.4). The results are similar to those of the total population, with the biggest differences in total subhaloes numbers seen in the most highest parent-halo-mass bin, the least in the lowest parent-halo-mass bin.

2.9.3 Radial distributions of galaxy analogues

Fig. 2.13 shows the radial profiles of the total numbers (*Row 1*) and the fractional mass in galaxy analogues (*Row 2*) as in Fig. 2.5, here separated into bins of parent halo mass. Qualitatively, the results are the same as those for the total analogue sample - both halo finders find similar numbers of analogues which account for similar amounts of mass outside $\sim 0.5 r_{\text{vir}}$. Within $\sim 0.5 r_{\text{vir}}$ however, ROCKSTAR detects more analogues, especially in the lowest parent mass bin. *Rows 3 & 4* in Fig. 2.13 show the subhalo levels the analogues are found at – the ROCKSTAR analogues are again found at deeper levels within the subhalo hierarchy as compared to AHF.

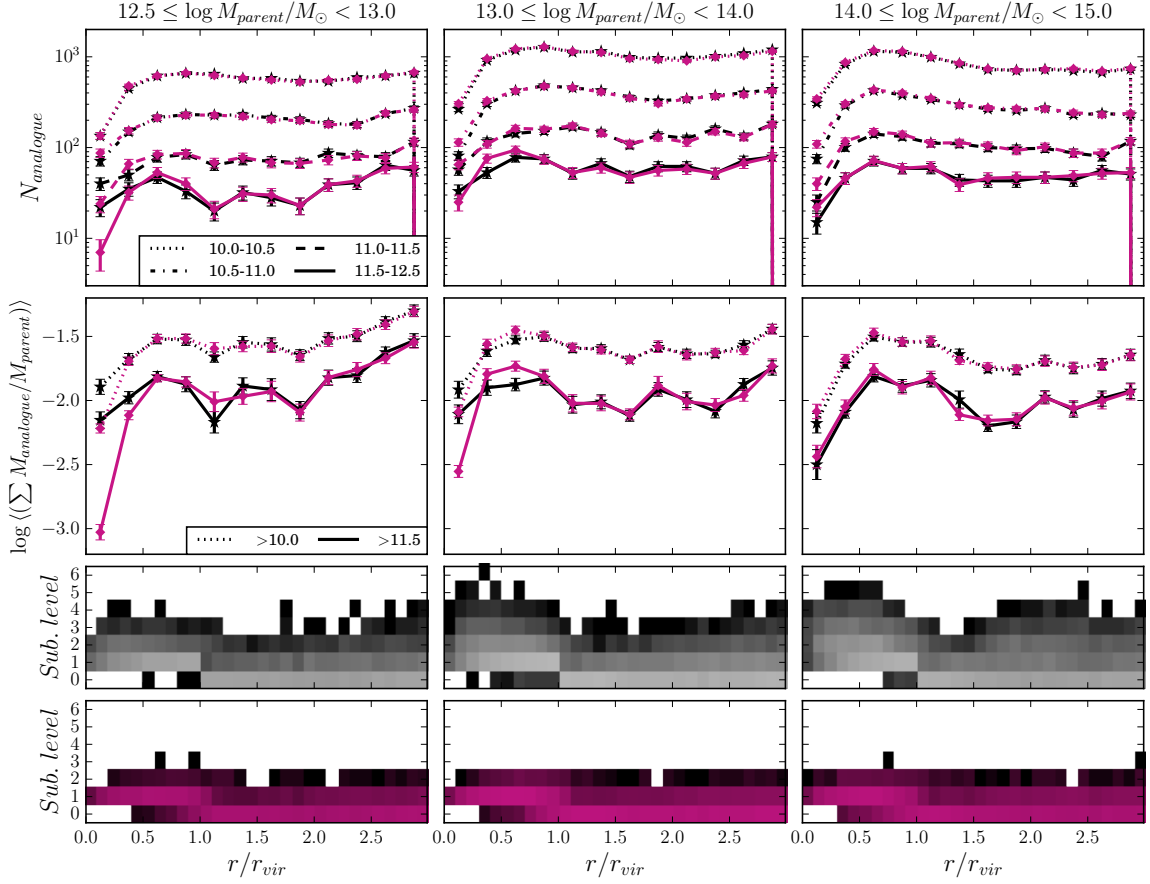


Figure 2.13: Total numbers of analogues (row 1) and fractional analogue mass averaged by number of parent haloes (row 2) versus radial separation from the parent halo centre as in Fig. 2.5, but separated by environment. We only show the first and last bins of analogue mass in Row 2 for clarity. The analogue populations selected by both halo finders are consistent with each other in the lower mass bins in terms of numbers of analogues, regardless of environment. The two differ in the highest mass bin however, resulting in significant differences in terms of the total mass assigned to these analogues in the lowest parent-halo-mass bin. Rows 3 & 4: 2D histograms of radial separation from parent halo centre and subhalo level as in Fig. 2.5, but separated by parent halo mass. The analogues selected from the ROCKSTAR catalogues are at higher subhalo levels as compared to those from AHF, although expectedly, at lower levels in the lowest parent halo mass systems.

CHAPTER 3

PREPROCESSING, MASS-LOSS AND
MASS SEGREGATION OF GALAXIES
IN DARK-MATTER SIMULATIONS

Reprinted from

Joshi, Gandhali J., Wadsley, James, Parker, Laura C., 2017, MONTHLY NOTICES OF THE ROYAL ASTRONOMICAL SOCIETY, Volume 468, Issue 4, p. 4625-4634, DOI: 10.1093/mnras/stx803. Published by Oxford University Press on behalf of the Royal Astronomical Society. All rights reserved.

Abstract

We investigate the mass loss of galaxies in groups and clusters with high-resolution dark matter simulations. We detect weak mass segregation in the inner regions of group/cluster haloes, consistent with observational findings. This applies to samples of galaxy analogues selected using either their present-day mass or past maximum (peak) mass. We find a strong radial trend in the fractional mass *lost* by the galaxies since peak, independent of their mass. This suggests that segregation is due to massive galaxies having formed closer to the halo centres and not the preferential destruction of smaller galaxies near halo centres. We divide our sample into galaxies that were accreted as a group versus as a single, distinct halo. We find strong evidence for preprocessing – the grouped galaxies lose $\sim 35\text{--}45\%$ of their peak mass before being accreted on to their final host haloes, compared to single galaxies that lose $\sim 12\%$. After accretion, however, the single galaxies lose *more* mass compared to the grouped ones. These results are consistent with a scenario in which grouped galaxies are preprocessed in smaller haloes while single galaxies ‘catch up’ in terms of total mass-loss once they are accreted on to the final host halo. The fractional mass-loss is mostly independent of the galaxy mass and host mass, and increases with amount of time spent in a dense environment.

3.1 Introduction

Galaxies have been shown to be influenced by their environment in different ways – on average, dense environments host larger fractions of galaxies that are red, elliptical and quenched, compared to isolated galaxy populations (e.g. Oemler, 1974; Dressler, 1980; Balogh et al., 2004; Hogg et al., 2004; Kauffmann et al., 2004; Blanton et al., 2005). Not only are galaxy populations different in groups/clusters compared to the field, galaxy properties can also depend on their group/cluster-centric radius. Such a radial segregation has been seen in properties such as morphology and luminosity (e.g. Girardi et al., 2003), colour (e.g. Blanton & Berlind, 2007), quenched fractions (e.g. Wetzel et al., 2012) and star formation rates (SFR; e.g. Balogh et al., 2000). The observed segregation in these properties can point towards various pathways of galaxy evolution. Furthermore, the question of where galaxies begin to be affected by their environment is yet to be answered and may be a major factor in establishing such trends.

Several different mechanisms have been put forth to explain galaxy properties in groups and clusters; processes such as mergers (Makino & Hut, 1997; Angulo et al., 2009), ram pressure stripping by the intragroup/cluster medium (Gunn & Gott, 1972; Abadi et al., 1999), harassment by other galaxies (Moore et al., 1996, 1998) and starvation (Larson et al., 1980; Balogh et al., 2000; Kawata & Mulchaey, 2008) can each affect galaxies differently. Each of these processes is efficient on different time-scales and at different masses and halo-centric radii. While the properties mentioned above all involve the baryonic content of the galaxy, mass segregation could arise purely through the gravitational interactions of its dark matter (DM) halo with other haloes. Understanding mass segregation can therefore point to which of the above processes are dominant in group and cluster environments.

Several observational and simulation studies have examined mass segregation and have found conflicting evidence. On the observational side, Lares et al. (2004) found significant segregation trends in the velocity functions of galaxies in different luminosity (and therefore stellar mass) ranges using data on group galaxies from the 2dFGRS (Colless et al., 2001). van den Bosch et al. (2008) found segregation in stellar mass using data from the Sloan Digital Sky Survey (SDSS) DR7 (Abazajian et al., 2009) and concluded that the trends were a result of mass segregation and correlations between stellar mass and colour/concentration. More recently, Roberts et al. (2015)

found weak stellar mass segregation in galaxy groups in the SDSS DR7. They also found that the segregation trends were stronger when low-mass galaxies were included and that the trends were weaker in higher mass groups/clusters. In contrast to these results, [von der Linden et al. \(2010\)](#) found no evidence of mass segregation in cluster galaxies in the SDSS, while [Ziparo et al. \(2013\)](#) only found mild stellar mass segregation and only at low-redshift using X-ray-selected groups from the COSMOS, GOODS and ECDFS fields. Most recently, [Kaffe et al. \(2016\)](#) also found no evidence of mass segregation using data from the GAMA survey ([Driver et al., 2011](#)), the GALFORM semi-analytic model ([Gonzalez-Perez et al., 2014](#)), and the EAGLE simulation ([Schaye et al., 2015](#)) in a wide range of halo masses. Using simulations and semi-analytic modelling, [Contini & Kang \(2015\)](#) found significant mass segregation trends; they found that average mass decreased with halocentric radius out to R_{vir} , then increased with radius out to $2R_{\text{vir}}$. [van den Bosch et al. \(2016\)](#) conducted an extensive study of segregation in various properties of DM haloes in the Bolshoi and Chinchilla simulations. While they only found a mild correlation in the present-day masses of the haloes as a function of their halocentric radius, they did find much stronger correlations when considering the mass at accretion or the amount of mass lost after accretion.

What drives mass segregation, if it does exist, is also not completely understood and several effects could be at work. Dynamical friction ([Chandrasekhar, 1943](#)), where the drag force from surrounding matter preferentially drives more massive haloes towards the centres of groups/clusters, may be one of the more important ones, as has been predicted by several studies (e.g. see [Ostriker & Tremaine, 1975](#); [Tremaine et al., 1975](#); [White, 1977](#)). Galaxies that are accreted earlier will also be located at smaller radii since virial radii at high redshifts were smaller; if these galaxies are also preferentially higher in mass, this can lead to mass segregation. Additionally, each of these effects has to contend with galaxies losing or gaining mass due to tidal stripping and mergers. Observing mass-*loss* in particular, would imply that tidal interactions, both with the encompassing host halo as well as the haloes of other galaxies in the group/cluster, are important in these environments.

These issues regarding mass-loss of galaxy haloes also lead to the phenomenon of preprocessing. While all of the processes mentioned above may occur in the current host haloes, there is mounting evidence that some of these galaxies were accreted as part of smaller groups and that any response they have had to their environment

began in these smaller groups. [McGee et al. \(2009\)](#) studied cluster assembly histories using the Millennium simulation and semi-analytic modelling and concluded that a large fraction of galaxies were accreted on to these clusters as part of smaller groups and were therefore potentially preprocessed. They did find, however, that the degree of preprocessing was dependent on the stellar mass of the infalling galaxies whereby more massive galaxies were more likely to be preprocessed. [Bahé et al. \(2013\)](#) studied radial trends in cold and hot gas mass and SFRs in clusters in the GIMIC suite of simulations. They found that $\sim 50\%$ of galaxies in massive clusters were accreted as part of smaller groups, decreasing to $< 10\%$ in low-mass groups, and that when these preprocessed galaxies were excluded, most of the radial trends they had observed were significantly weakened. [Hou et al. \(2014\)](#) used group and cluster galaxies in the SDSS DR7 and found that galaxies in ‘subhaloes’ (i.e. galaxy clumps within the group or cluster) showed enhanced quenched fractions beyond $\sim 1.5 - 2r_{200}$. They also concluded that preprocessing was important in massive clusters, but less so in smaller groups. [Gabor & Davé \(2015\)](#) studied clusters in a hydrodynamical simulation and found that approximately one-third of the cluster galaxies had been quenched in groups of mass $> 10^{12}M_{\odot}$.

It is important to establish whether preprocessing is indeed an important factor in the observed galaxy properties in groups and clusters. The environmental processes discussed above can alter galaxy properties; however, different mechanisms are dominant in different environments and determining where a galaxy begins transforming can shed light on what process(es) will drive its transformation. Preprocessing may account for a majority of the differences we observe between field and cluster galaxies, especially in the case of massive clusters that are expected to have accreted several smaller groups. Being able to separate such galaxies that have been preprocessed in groups from those that are truly influenced by the cluster will help clarify how clusters influence their member galaxies. Preprocessing also plays an important role in determining whether we see segregation in certain environments – while segregation may occur in smaller groups, as these groups are accreted on to larger clusters, they may destroy any trends formed within the cluster itself.

In this study, we use DM simulations to study both mass segregation and preprocessing in terms of mass-loss and mass-gain, and how these processes depend on various properties of the galaxy haloes. This paper is organized as follows: In Section 3.2, we describe the simulations and the data used for this study. Section 3.3

examines mass segregation in terms of present-day mass as well as peak mass and motivates the use of peak mass for further analysis. In Section 3.4, we study the role of preprocessing and its dependence on various properties of the galaxy haloes. Finally, we discuss our results in Section 3.5 and summarize our findings in Section 3.6.

3.2 Methods

3.2.1 Simulation

The data for this study come from a cosmological DM simulation of a $(100 \text{ Mpc})^3$ comoving volume run using the Tree-SPH (Tree-smoothed particle hydrodynamics) code CHANGA in N -body mode (Jetley et al., 2008, 2010; Menon et al., 2015). Initial conditions were generated using the code MUSIC (Hahn & Abel, 2013) assuming a flat standard Λ cold dark matter (CDM) cosmology with $\Omega_\Lambda = 0.6914$, $\Omega_m = 0.3086$, $h = 0.6777$, $n_s = 0.9611$ and $\sigma_8 = 0.8288$ (Planck Collaboration et al., 2014). The simulation contains 1024^3 particles resulting in a particle mass of $3.7 \times 10^7 M_\odot$ and a gravitational softening length of 1.25 kpc. The softening length is physical for $z < 8$ and comoving at higher redshifts. The simulation was run from $z = 100$ to 0 in 1000 time-steps with every fifth time-step saved, thus producing 200 snapshots equally spaced in time with each pair of consecutive snapshots separated by $\sim 68.9 \text{ Myr}$. Bound haloes were identified in each snapshot with the phase-space Friends-of-Friends algorithm ROCKSTAR (Behroozi et al., 2013a), and used to generate particle-based merger trees that were further refined using the code CONSISTENT TREES (Behroozi et al., 2013b). All halo properties are defined within a virial radius inside which the average density is Δ_c times the critical density of the Universe. The overdensity factor Δ_c is obtained for a flat Λ CDM Universe following Bryan & Norman (1998) as

$$\Delta_c(z) = 18\pi^2 + 82x - 39x^2, \quad (3.1)$$

where

$$x = \frac{\Omega_{m,0}(1+z)^3}{\Omega_{m,0}(1+z)^3 + \Omega_\Lambda} - 1. \quad (3.2)$$

For the cosmological parameters used in this study, this gives $\Delta_c = 102$ at $z = 0$.

3.2.2 Galaxy analogues

We begin by selecting a population of galaxy analogues – haloes that would host observed galaxies regardless of their position in the extensive subhalo hierarchy produced by the halo finder. In previous work (Joshi et al., 2016), we explored the differences between two halo finders in detecting substructure and the importance of taking into account the entire subhalo hierarchy in order to select a sample of haloes that could potentially host galaxies. We therefore defined a simple set of selection criteria that account for the portion of haloes missed due to their being embedded deep in the subhalo hierarchy. Briefly, starting at the distinct halo at the top of the subhalo hierarchy, we sort each candidate halo through the following criteria:

1. If $M_{\text{halo}} < 10^{10} M_{\odot}$, the halo and its branches in the hierarchy are eliminated.
2. If $M_{\text{halo}} > 10^{12.5} M_{\odot}$, the halo itself is eliminated, but each of its subhaloes is put through criteria (i)–(iv).
3. If $10^{10} < M_{\text{halo}} < 10^{12.5} M_{\odot}$ and the halo has no subhaloes with $M_{\text{halo}} > 10^{10} M_{\odot}$, the halo is accepted as an analogue while its subsequent branches in the hierarchy are eliminated.
4. If $10^{10} < M_{\text{halo}} < 10^{12.5} M_{\odot}$ and the halo has at least one subhalo with $M_{\text{halo}} > 10^{10} M_{\odot}$, then we consider $M_{\text{rem}} = (M_{\text{halo}} - \sum M_{\text{subhalo}})$; if $10^{10} < M_{\text{rem}} < 10^{12.5} M_{\odot}$, then the halo is accepted as a galaxy analogue while each of its subhaloes is also put through criteria (i)–(iv).

The mass limits used for these criteria were chosen to correspond to the stellar masses of galaxies in typical redshift surveys, as we show in Section 3.3.2. We generate two sets of galaxy analogues, one where the mass under consideration is the $z = 0$ virial mass and one where it is the peak mass of the halo. A total of 43530 galaxy analogues were selected for the first set, and 80425 were selected for the second. For the remainder of this paper, we refer to the galaxy analogues as just ‘galaxies’, although we emphasize that this nomenclature is adopted for simplicity – we are only analysing DM haloes in this paper, and therefore make no statements regarding the fate of their stellar or gas content. Note that the large difference we see in the sizes of the two samples is because the M_{peak} -selected sample contains galaxies that had relatively low peak masses, that have subsequently lost mass and, by present day,

fall below the lower mass threshold to be included in the $M_{z=0}$ -selected sample; this affects $\sim 46.5\%$ of the M_{peak} -selected sample. Conversely, high-mass galaxies in the $M_{z=0}$ -selected sample could also have peak masses beyond the upper mass limit to be included in the M_{peak} -selected sample; however, the number of such cases is negligibly low compared to the first case, i.e. $\sim 0.3\%$ of the $M_{z=0}$ -selected sample.

3.3 Mass segregation

3.3.1 Comparing $M_{z=0}$ and M_{peak}

We first investigate the mass segregation of the galaxies in terms of both present-day mass, $M_{z=0}$, as well as peak mass, M_{peak} . In Figs 3.1(a) and (b), we show the average galaxy mass as a function of halocentric radius. The different colours represent bins of $\log M$ where the mass is defined as $M_{z=0}$ in (a) and M_{peak} in (b). The upper limit for the bins is always set to 12.5, while the lower limit is gradually altered to show the effect of excluding low mass galaxies.

The results in Fig. 3.1(a) were reported in our previous study (Joshi et al., 2016) and reproduced here for comparison. Note that the sample used here is slightly different than the one in our previous study due to the additional processing carried out by CONSISTENT TREES (see Section 3.2.1). However, these differences are negligible for our results. We had previously found a statistically significant but mild negative trend in $M_{z=0}$ in the inner $0.5 r_{\text{vir}}$, i.e. average $M_{z=0}$ decreasing with halo-centric radius. The trends were weaker when low-mass galaxies were excluded. Both these results are reproduced here.

The results in Fig. 3.1(b), which show segregation in M_{peak} , are consistent with those in Fig. 3.1(a), showing that the mass segregation trends do not depend on the mass definition we use. This is mainly because, for each point on the plots, we average over the same absolute values of mass. This implies that within each radial bin, there are no significant differences in the distribution of $M_{z=0}$ and M_{peak} for the galaxies. This does not mean that the two samples are equivalent, however. To understand these results further, we examine the trends in the fractional mass retained since peak to present day, $M_{z=0}/M_{\text{peak}}$, in Figs 3.1(c) and (d), where the samples used are the same as in Figs 3.1(a) and (b), respectively. Figs 3.1(c) and (d) show that the trend in the ratio of peak mass-to-present-day mass is much stronger than the

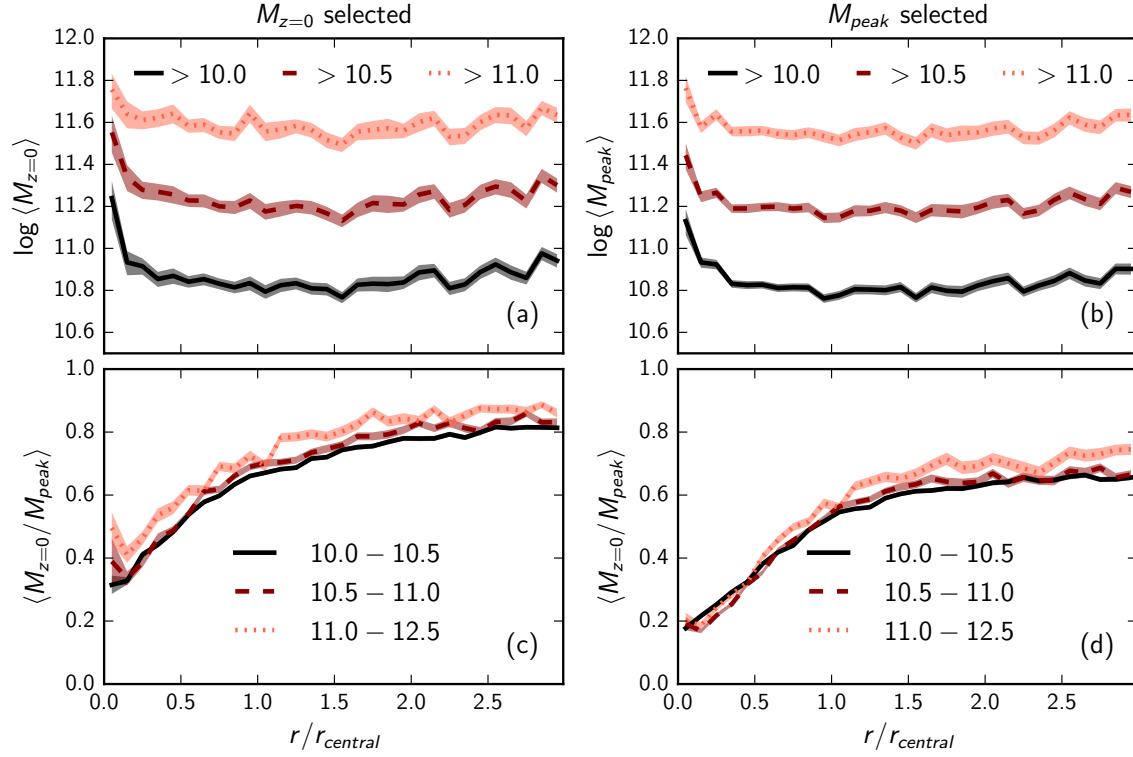


Figure 3.1: Segregation in DM-halo mass of galaxies. (a) and (b) show the average mass of the galaxies as a function of present-day halocentric radius with mass defined as present-day mass, $M_{z=0}$, in (a) and peak mass, M_{peak} , in (b). The different colours (and linestyles) represent bins of $\log M_{z=0}$ in (a) and $\log M_{\text{peak}}$ in (b); the upper limit is always set to 12.5 and the lower limit is altered to examine the effect of excluding low mass galaxies. (c) and (d) show the average fractional mass retained from peak to present day, $M_{z=0}/M_{\text{peak}}$, as a function of halocentric radius. The colours represent bins of $\log M_{z=0}$ in (c) and $\log M_{\text{peak}}$ in (d). The errors shown are standard errors on the mean.

trend in absolute mass. There is a strong trend in both Figs 3.1(c) and (d) with $M_{z=0}/M_{\text{peak}}$ rising with radius out to around $\sim r_{\text{central}}$, beyond which the trends are shallower. Additionally, the $M_{z=0}$ -selected galaxies consistently retain more of their peak mass compared to the M_{peak} -selected galaxies at all radii. These results show that the M_{peak} -selected sample of galaxies has undergone more mass-loss compared to the $M_{z=0}$ -selected sample.

It should be noted that the weak mass segregation trends seen here could result naturally if the halo finder were systematically unable to detect smaller galaxies near the centres of their host haloes. Previous work has shown that the radial distribution of subhaloes in DM simulations is less concentrated than that of observed satellite galaxies (e.g. see Gao et al., 2004; Springel et al., 2008; Budzynski et al., 2012, among others). We explored this issue in more detail in our previous work (Joshi et al., 2016) and found that ROCKSTAR was better able to recover low-mass subhaloes near the centres of their host haloes compared to another popular halo finder, AHF, which only uses spatial information (Knollmann & Knebe, 2009). Additionally, CONSISTENT TREES was designed to follow subhaloes across time-steps more consistently to ensure that we do not lose subhaloes when they pass close to their host halo’s centre (Behroozi et al., 2013b). We examined the radial distributions of the number density of our galaxy samples (not shown here) and while we find some flattening within $\sim 0.5 r_{\text{vir}}$, the flattening is independent of galaxy mass. This lack of a *differential* flattening between the low-mass and high-mass galaxies implies that the average mass in each radial bin is not significantly affected. This radial flattening independent of subhalo mass was also seen by Springel et al. (2008). These factors would suggest that our mass segregation trends are not numerical artefacts.

One additional result to note from Figs 3.1(c) and (d) is that the mass-loss within each radial bin is nearly independent of the mass of the galaxies [$M_{z=0}$ in (c) and M_{peak} in (d)], which implies that any mass segregation trends are not due to the preferential loss of smaller galaxies in the inner regions of the host haloes. Instead, this result confirms that the mass segregation trends we see are due to larger galaxies having formed closer to the centres of their final host haloes.

The galaxies we consider here have spent a significant amount of time in dense environments and therefore could have lost mass due to tidal stripping, which removes the more extended DM from a galaxy more efficiently than its more bound stellar content. It follows that when comparing with observational results, M_{peak} is the

more physically motivated choice, as M_{peak} is much more correlated with present-day stellar mass than $M_{z=0}$, as has been shown in previous studies. For example, using N -body simulations of dwarf spheroidals in clusters, [Peñarrubia et al. \(2008\)](#) showed that nearly $\sim 90\%$ of the galaxies' DM had to be tidally stripped before any of the stellar content was stripped. More recently, [Smith et al. \(2016\)](#) used hydrodynamical simulations of cluster galaxies with a wide range of stellar masses to show that when tidal stripping had removed $\sim 80\%$ of DM from the galaxies, they had only lost $\sim 10\%$ of their stellar content. Therefore, for the remainder of this study, we focus on the sample of M_{peak} -selected galaxies.

3.3.2 Comparing to observational results

In [Fig. 3.2](#), we show the expected mass segregation in terms of stellar mass, M_\star . We assign M_\star to the galaxies using two different prescriptions for the stellar mass-to-halo mass relations, $f_\star = M_\star/M_{\text{halo}}$, to convert M_{peak} to a stellar mass. The first is from [Hudson et al. \(2015\)](#) (hereafter H15):

$$f_\star(M_{\text{halo}}) = 2f_1 \left[\left(\frac{M_{\text{halo}}}{M_1} \right)^{-\beta} + \left(\frac{M_{\text{halo}}}{M_1} \right)^\gamma \right]^{-1}, \quad (3.3)$$

where we use $M_{\text{halo}} \equiv M_{\text{peak}}$. Although their best-fitting model suggests a mild evolution in f_\star with redshift, the range of redshifts considered in H15 is 0.2–0.8, whereas the analogue sample in our study covers a range in z_{peak} of 0–5.5. The parameters for the best-fitting model would result in a value of f_\star that exceeds the cosmic baryon fraction by $z_{\text{peak}} \sim 4.5$. We therefore use the parameters for their ‘no-evolution’ model for all galaxies: $f_1 = 0.04$, $\log M_1 = 12.38$, $\beta = 0.69$ and $\gamma = 0.8$, and do not include scatter in the relation.

The second relation we use is from [Behroozi et al. \(2013c\)](#) (hereafter B13):

$$\log(M_\star(M_h)) = \log(\epsilon M_1) + f \left(\log \left(\frac{M_h}{M_1} \right) \right) - f(0) \quad (3.4)$$

$$f(x) = -\log(10^{\alpha x} + 1) + \delta \frac{(\log(1 + \exp(x)))^\gamma}{1 + \exp 10^{-x}} \quad (3.5)$$

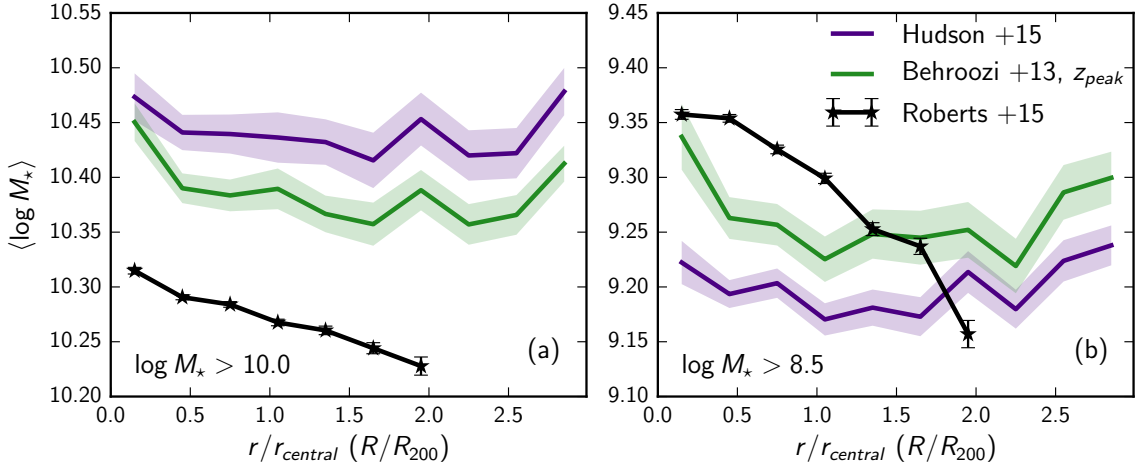


Figure 3.2: Segregation in stellar mass. Average stellar mass as a function of halo-centric radius using two different stellar mass-to-halo mass prescriptions: The purple line uses the ‘no-evolution’ fit from [Hudson et al. \(2015\)](#); the green line uses the prescription from [Behroozi et al. \(2013c\)](#) defined at z_{peak} for each galaxy. In (a), only galaxies with $M_{\star} > 10^{10}M_{\odot}$ are used; (b) uses lower mass galaxies with $M_{\star} > 10^{8.5}M_{\odot}$. Since the segregation results for the DM-halo masses of the galaxies are stronger when low mass galaxies are included, we wanted to determine if the lower mass cut would affect the stellar mass results in the same way. We compare our results to observational results from [Roberts et al. \(2015\)](#), shown in black; while their sample is complete and unweighted in (a), it is V_{max} -weighted in (b) to correct for incompleteness. The mass limits on the host haloes are identical between our results and the observational results. The errors shown are standard errors on the mean. Note that we use r_{vir} instead of R_{200} and our positions are in 3D, while those in [Roberts et al. \(2015\)](#) are projected.

where the parameters M_1 , α , γ , δ and ϵ are functions of redshift. We use the best-fitting parameters from B13 at z_{peak} and $M_h \equiv M_{\text{peak}}$. Again, we do not introduce any scatter in the relation.

Fig. 3.2 shows average profiles for M_* as a function of halocentric radius for two lower mass limits and for the two different stellar mass-to-halo mass relations. In order to compare with observational results, we also show results from Roberts et al. (2015) in black. The observational results in Fig. 3.2(b) have been V_{max} -weighted to account for incompleteness at such low stellar masses. There is a systematic offset between our results and the observations; however, the trends differ by at most 0.3 dex using the H15 relation, 0.15 using the B13 relation, and have similar slopes. The stellar mass functions for our data follow a single power law, similar to their (DM) halo mass functions, as shown in Joshi et al. (2016) (Fig. 2), whereas those for the observational data have characteristic Schechter function profiles, which could be one of the factors responsible for the differences between our results and the observations. It should be noted that amongst recent studies that find evidence for mass segregation, the trends detected are quite weak, which is consistent with our findings.

3.4 The role of preprocessing

The results of the previous section show that galaxies undergo significant mass-loss from their peak mass under the influence of a group/cluster halo. In this section, we explore whether the galaxies experience some of this mass-loss in smaller haloes before they become part of their final group/cluster.

To do so, we first separate the galaxy sample into galaxies that were part of a smaller group prior to infall and those that were not. We define these samples based on whether or not the analogue was distinct (i.e. identified as the top of the subhalo hierarchy by the halo finder) before the first time it crosses within a virial radius. We first remove those galaxies that have never crossed within r_{vir} of their central halo, which affects a little less than half our sample, reducing the sample size to 45105. Galaxies found beyond a virial radius at $z = 0$ are necessarily backsplash galaxies. Such galaxies constitute 26% of this reduced sample [87% of the backsplash galaxies lie in the range $1-2r_{\text{central}}$, while the remaining 13% lie beyond $2r_{\text{central}}$], and represent a different population compared to those found within the virial radius. Hence, for any further analysis, we treat the two separately. Also note that not all galaxies

found within a virial radius are on their first passage within the central halo, nor are all of them on an infall trajectory (i.e. some are on their way out of the central halo); but for convenience, we will simply refer to this subsample as the ‘infall’ population. We separate the galaxies into those that were distinct at *all* timesteps before the first time they crossed the virial radius of their central halo and those that were not (we hereafter refer to this event as ‘crossing’). The former population is designated as ‘single’ and the latter is designated as ‘grouped’. Most of the galaxies reach their peak mass before or at the time of crossing; however, a small fraction of them, $\sim 15\%$ of our total sample (24% of the single sample, 10% grouped sample), do so after crossing. For clarity, we remove these galaxies from the sample, although including them does not qualitatively change our subsequent results. We are then left with 38287 galaxies in total, 12666 in the single category and 25621 in the grouped category.

In Fig. 3.3, we first examine the average total mass retained from peak to present day, $M_{z=0}/M_{\text{peak}}$, as a function of present-day halo-centric radius, as in Fig. 3.1(d), now separating the sample into single and grouped populations. The shaded areas show the 25th-75th percentile range of the data in each radial bin, while the error bars are standard errors on the mean. The gap at r_{central} separates the infall and backsplash galaxies. The figure shows that at nearly all radii, the grouped galaxies have lost more mass since their peak compared to the single galaxies, which suggests that the grouped galaxies were preprocessed. For the backsplash galaxies, the differences between the single and grouped galaxies are nearly constant at all radii with the grouped galaxies losing $\sim 15\text{--}20\%$ more mass than the single galaxies. However, for the infall populations, the differences between the grouped and single galaxies are negligible at the halo centre and increase with increasing radius. The negligible difference at the halo centre appears to be at odds with the significant $\sim 15\text{--}20\%$ difference for the backsplash galaxies, since the backsplash galaxies would have passed near the halo centre at an earlier time and should now display the same amount of mass-loss between the single and grouped populations.

To understand the exact sequence of mass-loss and mass-gain, we separate the mass-loss since peak into two stages – before and after crossing. We show the average mass retained from peak to crossing, $M_{\text{cross}}/M_{\text{peak}}$, in Fig. 3.4(a), and crossing to present-day, $M_{z=0}/M_{\text{cross}}$, in Fig. 3.4(b) as a function of halocentric radius. Note that while $M_{\text{cross}}/M_{\text{peak}}$ is less than one by definition for all galaxies, $M_{z=0}/M_{\text{cross}}$ can be greater than one. Fig. 3.4(b) shows that within a virial radius, the closer the galaxies

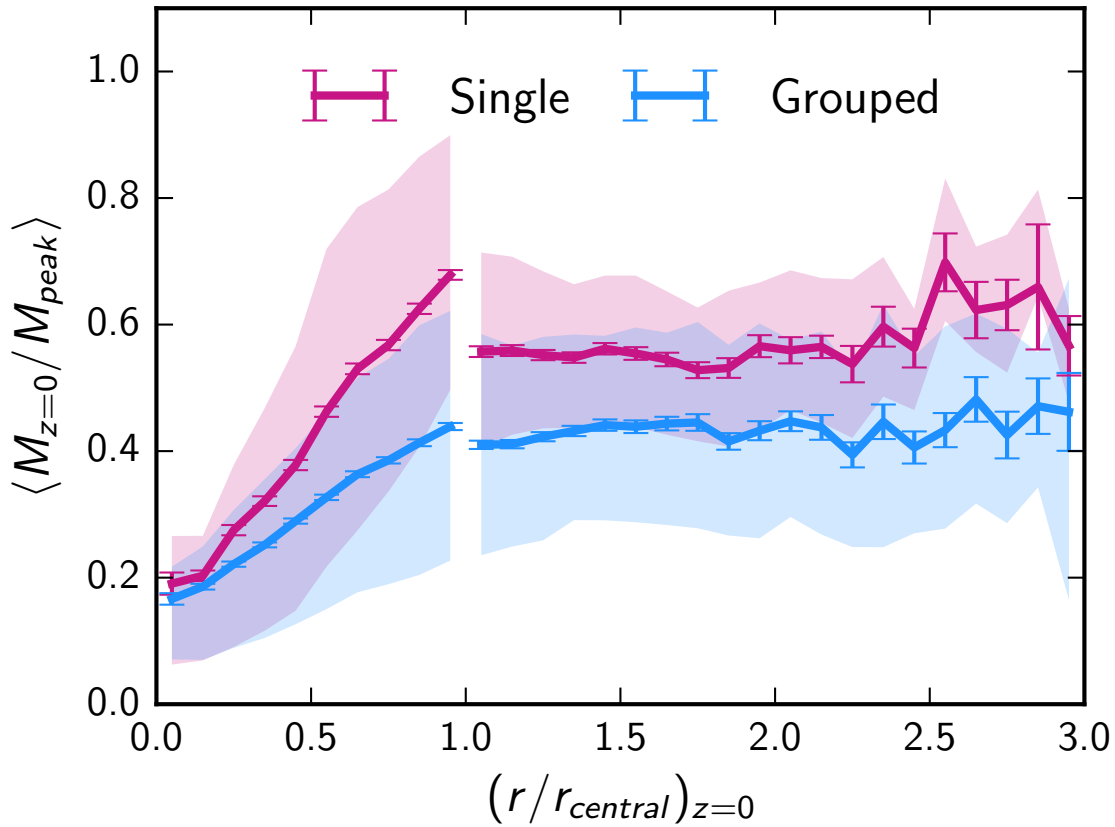


Figure 3.3: Average mass of the galaxies retained since peak to present day as a function of present-day halocentric radius, as in Fig. 3.1(d), now separated into single (pink) and grouped (blue) samples. The shaded areas show the 25th–75th percentile range of the data in each radial bin, whereas the error bars show the standard error on the mean. The gap at $r_{central}$ separates the infall and backplash populations.

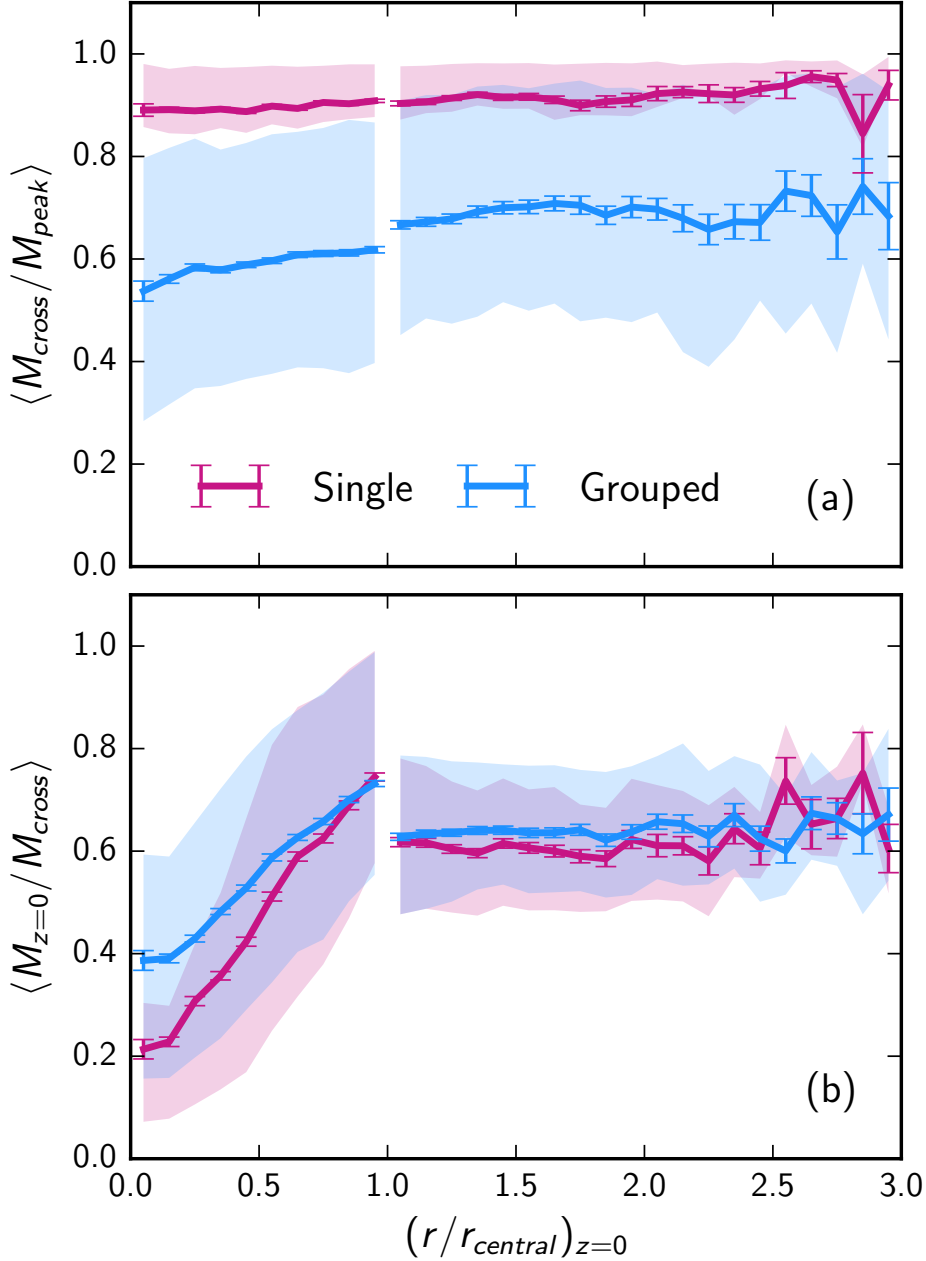


Figure 3.4: Average mass of the galaxies retained from peak to crossing (a) and from crossing to present day (b) as a function of present-day halocentric radius. The single sample is shown in pink and the grouped sample is shown in blue. The shaded areas show the 25th–75th percentile range of the data in each radial bin whereas the errorbars show the standard error on the mean. The gap at r_{central} separates the infall and backplash populations. (a) shows clear evidence for preprocessing where the grouped galaxies had consistently undergone more mass-loss than the single galaxies *before* they crossed within a virial radius of the central halo.

are to the central halo, the more mass they appear to have lost. The single galaxies lose *more* mass than the grouped galaxies. The differences are largest at small radii and decrease with increasing radius. This can be explained by the fact that grouped galaxies are in a denser potential and therefore somewhat shielded from the effects of the final host halo. Additionally, if they have already undergone some mass-loss in smaller haloes, they are likely to be compact, dense objects, less prone to mass-loss. The single galaxies, on the other hand, are likely to have much more loosely bound material in their outskirts, which is more easily stripped by the host halo. The results beyond a virial radius are consistent with having no radial trend and there is no significant difference between the single and grouped sample. This may suggest that after passing through pericentre, the galaxies do not retain any information regarding whether they were single or grouped, or regarding their orbital properties, although more analysis is needed to verify this.

However, *before* crossing a virial radius, there is a clear difference in the amount of mass lost since peak, as shown in Fig. 3.4(a). The grouped sample has consistently lost more mass than the single sample; for the single sample, $\langle M_{\text{cross}}/M_{\text{peak}} \rangle \sim 0.88$, whereas for the grouped sample, $\langle M_{\text{cross}}/M_{\text{peak}} \rangle \sim 0.55\text{--}0.65$. This is clear evidence of galaxies being preprocessed in smaller groups before they are accreted on to their present-day host haloes. Figs 3.4(a) and (b) therefore suggest a scenario in which, compared to single galaxies, grouped galaxies lose significantly more mass in smaller haloes before becoming part of their final host haloes through preprocessing. However, once both sets of galaxies cross within a virial radius of the host halo, the single galaxies lose more mass compared to the grouped galaxies, essentially ‘catching up’ with the total amount of mass-loss of the grouped galaxies. This sequence of events also explains why the backsplash galaxies have nearly the same amount of mass-loss after crossing, whereas they have significant differences in the total amount of mass-loss since peak, as seen in Fig. 3.3.

To investigate if the results in Figs 3.3 and 3.4 are driven by other properties of the galaxies, we examined these radial trends in bins of present-day galaxy mass $M_{z=0}$, the mass of the central halo M_{central} , the peak redshift z_{peak} and the redshift of crossing z_{cross} . We find no dependence of the average mass loss (before or after accretion) on $M_{z=0}$, and a mild dependence on M_{central} where galaxies in more massive clusters had lost slightly more mass before crossing, and slightly less after crossing, as compared to galaxies in lower mass groups. These results are expected since galaxies found in more

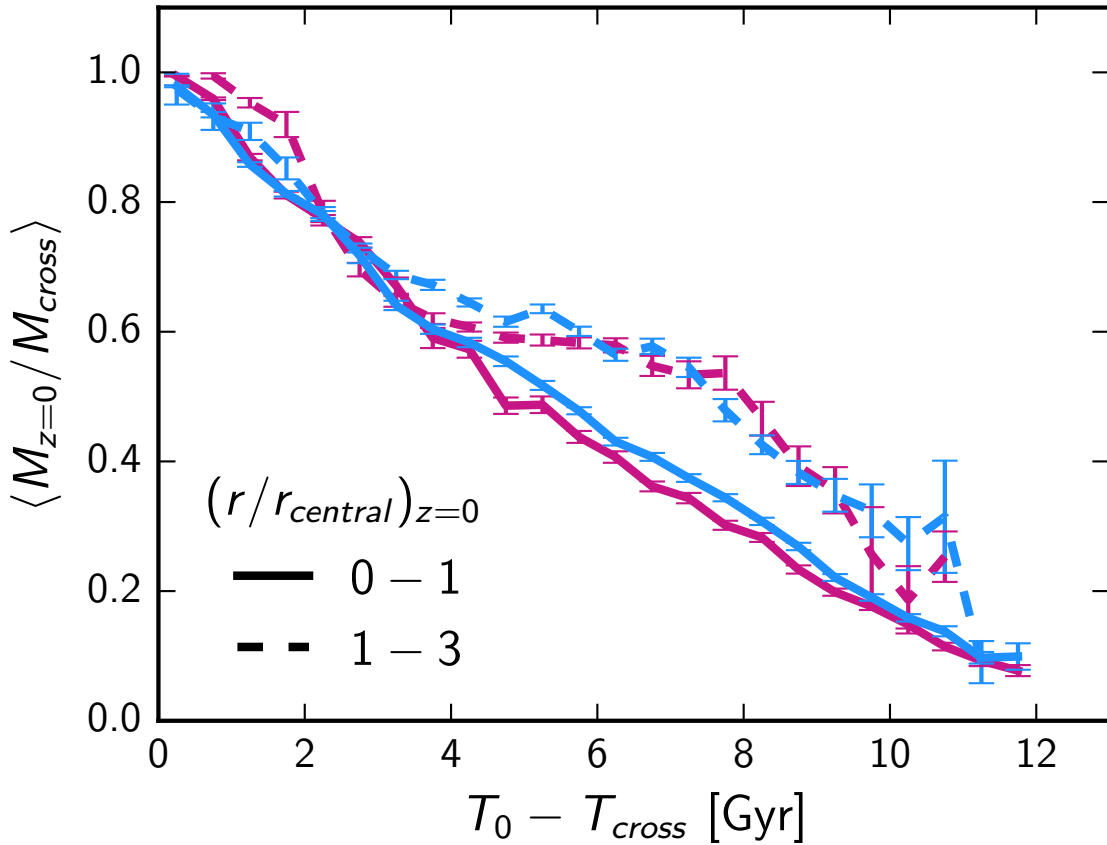


Figure 3.5: Average mass of the galaxies retained from crossing to present day as a function of time since crossing (T_0 and T_{cross} are the ages of the Universe at $z = 0$ and z_{cross} , respectively). The single sample is shown in pink and the grouped sample is shown in blue, as in Fig. 3.3. The different linestyles are bins of the present-day radial position of the galaxies in their central haloes such that the backsplash galaxies are shown by the dashed lines. No significant difference is seen in the mass lost by the single and grouped galaxies after crossing the virial radius of their central halo.

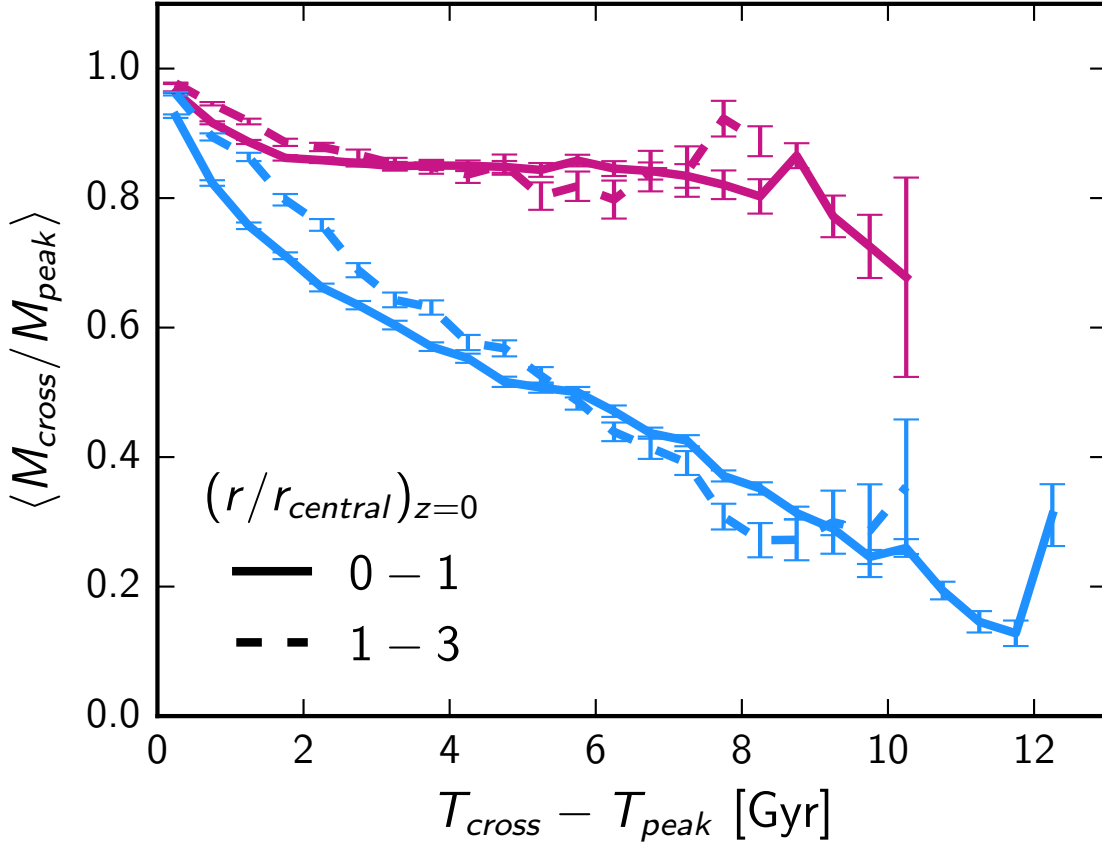


Figure 3.6: Average mass of the galaxies retained from peak to crossing as a function of time between peak and crossing events (T_{peak} and T_{cross} are the ages of the Universe at z_{peak} and z_{cross} , respectively). The single sample is shown in pink and the grouped sample is shown in blue, as in Fig. 3.3. The different linestyles are bins of the present-day radial position of the galaxies in their central haloes such that the backsplash galaxies are shown by the dashed lines. The grouped sample has lost significantly more mass before crossing as compared to the single sample. The mass lost is strongly correlated with the time interval between z_{peak} and z_{cross} with the trend being much steeper for the grouped sample and nearly flat for the single sample.

massive clusters at $z = 0$ are more likely to be preprocessed as the cluster is likely to have accreted several groups of galaxies. However, the results showed a strong dependence on z_{peak} and z_{cross} , implying that the main factor driving these results is the amount of time the galaxies have spent within a given environment. Hence, we examine this in further detail in Figs. 3.5 and 3.6.

In Fig. 3.5, we show the average mass retained after crossing as a function of time since crossing. The infall sample is shown by the solid lines and the backsplash sample is shown by the dashed lines. The figure confirms that there is no significant difference between the single and grouped galaxies once they have crossed within a virial radius. The infall population displays a strong, nearly monotonic trend with time since crossing; these galaxies appear to steadily lose mass within the central halo. The bump seen in the trends for the backsplash galaxies at longer times since crossing is likely due to the fact that these galaxies have spent a significant amount of time outside a virial radius of the central halo and therefore experienced lower amounts of mass-loss. Galaxies who first crossed a virial radius $\lesssim 3\text{Gyr}$ ago have probably only recently crossed back out.

Fig. 3.6 shows the average mass retained from peak to crossing as a function of the time interval between peak and crossing. As in Fig. 3.5, the infall population is shown by the solid lines and the backsplash population is shown by the dashed lines. In this figure, there is a significant separation between the single and grouped samples as in Fig. 3.4(a), which is clear evidence for preprocessing. The amount of mass lost is strongly correlated with the time interval between peak and crossing for the grouped sample, whereas for the single sample, the trend is nearly flat with the galaxies losing $\sim 10\%$ of their peak mass regardless of the time interval. This mass-loss may partially be due to how well the halo finder can recover the masses of these galaxies at each time-step. Note that, by definition, any uncertainty in galaxy mass will be seen as a mass-loss when compared to peak mass. Knebe et al. (2011) investigated the performance of several halo finders by running them on a DM system consisting of a halo, subhalo and subsubhalo with known properties and found that ROCKSTAR was able to recover their masses to within $\sim 10\%$.

3.5 Discussion

3.5.1 Mass segregation

In this work, we have examined mass segregation in group/cluster haloes. In our previous study using DM simulations (Joshi et al., 2016), we showed that the mass segregation of galaxies was restricted to within $\sim 0.5 r_{\text{vir}}$, where galaxies near the centres of groups and clusters were, on average, more massive than those at large radii. Here we apply a more physically motivated mass definition for the galaxies, M_{peak} , and re-examine these radial trends. Using M_{peak} also allows us to directly compare to observational results that use stellar mass. We compare the radial trends using both mass definitions and find that they both produce the same results within the mass range of interest. However, the two mass definitions select significantly different populations of galaxies – the $M_{z=0}$ -selected sample consisted of high-peak-mass galaxies that had undergone a lower amount of mass-loss and the M_{peak} -selected sample consisted of intermediate-peak-mass galaxies that had undergone a higher amount of mass loss. This is apparent in Figs 3.1(c) and (d), where the $M_{z=0}$ -selected sample has values of $M_{z=0}/M_{\text{peak}}$ that are consistently higher than for the M_{peak} -selected sample at all radii and irrespective of galaxy mass. The results in Figs 3.1(a) and (b) are broadly in agreement with van den Bosch et al. (2016), who found mild segregation in both $M_{z=0}$ and M_{peak} , although note that they explicitly removed any dependence on central halo mass by normalizing these masses by M_{central} . Their sample selection is also based on $M_{z=0}/M_{\text{central}}$ as well as mass at accretion, so that our results are not directly comparable.

In our previous study, we concluded that while the results do not rule out the effect of dynamical friction, it was not the most important factor driving the mass segregation trends. The results in Figs 3.1(c) and (d) show that the galaxies undergo a significant amount of mass-loss from peak mass and that there is a strong radial trend in the amount of mass lost. Thus, even if dynamical friction does act on these galaxies, its effects would gradually be diminished with time as the galaxies lose mass due to tidal stripping. We investigated these results in bins of central halo mass and found the same trends as in our previous work. Although not presented here, the mass-segregation trends are strongest in low mass groups with $\log M_{\text{central}} = [12.5, 13]$ and grow weaker with increasing central halo mass. This already suggests that the galaxies are preprocessed in smaller groups before the groups are accreted on to larger

clusters, where the infall of groups would destroy any segregation trends that may have existed in the clusters.

3.5.2 Preprocessing

Fig. 3.4(a) shows that there is clear evidence for galaxies being preprocessed in smaller groups before being accreted into larger host haloes. We examined the dependence of these results on M_{peak} , M_{central} , z_{peak} and z_{cross} . We did find a mild correlation with host halo mass for the grouped sample where galaxies in the most massive (present-day) haloes had lost *more* mass before crossing than those in the least massive haloes; the opposite trend is seen for mass lost after crossing. We also found that the crucial variable determining the amount of mass lost by the galaxies is the amount of time they spend in a particular environment. Figs 3.5 and 3.6 show that the amount of mass lost after crossing is strongly correlated with time since crossing for both the single and grouped sample. In the case of mass-loss from peak to crossing, however, only the grouped sample has a similar strong trend with time between peak and crossing; the single galaxies appear to lose $\sim 10\%$ of their peak mass regardless of the time interval (provided it is not too short). One factor to keep in mind is that all these results are dependent on the halo finder’s ability to consistently detect the galaxies at each time-step and reliably determine their masses and sizes, especially in these dense environments. ROCKSTAR is able to detect substructure near host halo centres due to its use of phase-space information, although it can overpredict or underpredict the subhaloes’ masses in such high-density environments (Knebe et al., 2011). Using CONSISTENT TREES has the advantage of not only consistently following subhaloes, but also, to some degree, repairing artificial mass fluctuations (Behroozi et al., 2013b). Hence, although this is an issue to consider, especially if comparing to results from different halo finders, the results presented here are mostly physical and not artefacts produced by the halo finders.

One crucial aspect of this analysis is the radius we chose to define crossing. While a virial radius seems a natural choice, there is evidence that the host halo’s influence can begin at a larger distance. In Fig. 3.7, we show tracks of virial mass as a function of distance from the present-day central halo for individual galaxies. We randomly choose three galaxies each from the single and grouped populations in narrow bins of $\log M_{\text{peak}} = [10.9-11]$ and $\log M_{\text{central}} = [13.5-13.6]$. This ensures that the chosen galaxies have nearly identical starting points and eventual host environments. Despite

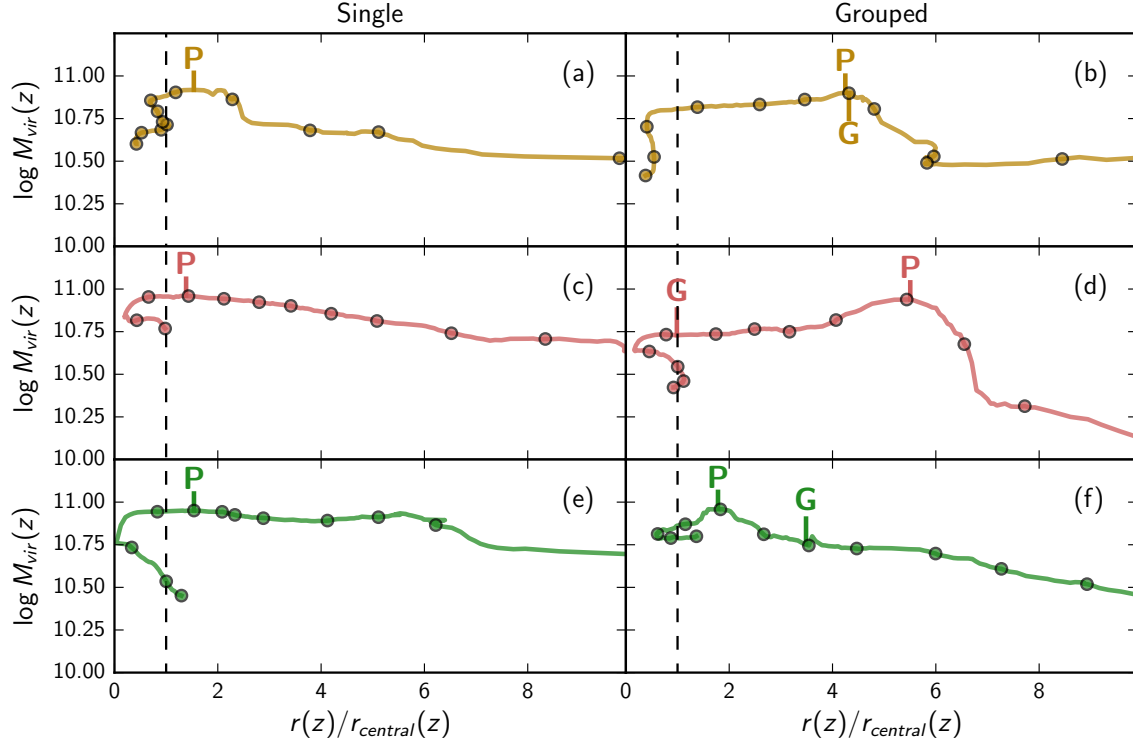


Figure 3.7: Tracks of individual galaxies showing virial mass as a function of distance to the present-day central halo normalized by the central halo’s virial radius at that redshift. Three galaxies were chosen randomly within a narrow range in galaxy peak mass and central halo mass ($\log M_{\text{peak}} = [10.9\text{--}11]$ and $\log M_{\text{central}} = [13.5\text{--}13.6]$), shown in different colours. The left-hand panel contains galaxies from the single sample and the right-hand panel contains galaxies from the grouped sample. The black points mark roughly 1 Gyr intervals (15 timesteps). The vertical black dashed lines mark r_{vir} for clarity. We have also marked the peak mass with the letter ‘P’, and for the grouped analogues, the point at which they first become part of a larger halo, marked with the letter ‘G’.

this, Fig. 3.7 shows that the galaxies can have varied histories and can reach very different present-day masses. Although the single galaxies appear to reach their peak mass close to the virial radius of the host halo, they do not appear to grow significantly in mass from a distance of a few virial radii. The grouped galaxies have more diverse histories. In Fig. 3.7(b), the galaxy appears to peak at the same time it becomes part of a group and then steadily loses mass, which is consistent with the scenario discussed in Section 3.4, whereby the galaxy continues to grow in mass until it becomes part of a group, after which it steadily loses mass before, as well as after, crossing within a virial radius of its final host halo. In Fig. 3.7(d), however, the galaxy starts losing mass long before it becomes part of a group, suggesting the influence of another halo at distances larger than a virial radius. Fig. 3.7(f) shows a rare scenario where the galaxy continues to grow in mass even after becoming part of a group, although note that such a track is not representative of the sample, rather an interesting outlier. Once the haloes cross a virial radius, regardless of whether they are single or grouped, they steadily lose mass as they spiral towards the host centre. While this analysis is preliminary, it does imply that defining crossing at a virial radius does not adequately capture the effects of the central halo. The degree to which this is important and what the ideal crossing radius definition is will be explored in future work, but it does indicate that any studies involving environmental effects must be careful in defining the radius of accretion as it can significantly alter their results.

3.6 Summary

We use N -body simulations and define a sample of galaxy analogues to explore mass segregation in groups and clusters as well as the role of preprocessing in determining mass-loss trends for these analogues:

1. Consistent with our results in Joshi et al. (2016), we find weak mass segregation within $0.5 r_{\text{vir}}$, with average mass decreasing with halocentric radius. The results are largely independent of the mass definition used – $M_{z=0}$ or M_{peak} . We also find a strong radial trend in the amount of mass lost since peak and a significant difference in these trends for the two samples. The M_{peak} -selected galaxies appear to have lost more mass since peak at all radii.

2. We find that grouped galaxies that first cross within a virial radius of their present-day central halo as part of a group lose $\sim 35\text{--}45\%$ of their peak mass, compared to single galaxies that cross as distinct haloes, which lose $\sim 12\%$. This is clear evidence for preprocessing in smaller haloes before accretion on to the present-day central halo.
3. The fraction of mass lost does not depend on galaxy mass and only weakly depends on the central halo mass. However, we find a strong correlation between the degree of mass-loss and the amount of time the galaxies spend in a specific environment.

This study shows that there is clear preprocessing in the mass lost by DM haloes. We look forward to including baryonic physics in our simulations that could have additional preprocessing effects. Our future work will focus on following the galaxies along their halo tracks and determining if these results extend beyond a virial radius of the central halo, as well as studying how baryonic processes affect our current results.

Acknowledgements

We thank the anonymous referee for their comments and insights that were very useful in improving the manuscript. We thank the National Science and Engineering Research Council of Canada for their funding. Computations were performed on the *gpc* supercomputer at the SciNet HPC Consortium ([Loken et al., 2010](#)). SciNet is funded by the following: the Canada Foundation for Innovation under the auspices of Compute Canada; the Government of Ontario; Ontario Research Fund – Research Excellence; and the University of Toronto. This work was made possible by the facilities of the Shared Hierarchical Academic Research Computing Network (SHARCNET: www.sharcnet.ca) and Compute Canada.

References

- Abadi M. G., Moore B., Bower R. G., 1999, [MNRAS](#), **308**, 947
- Abazajian K. N., et al., 2009, [ApJS](#), **182**, 543

- Angulo R. E., Lacey C. G., Baugh C. M., Frenk C. S., 2009, [MNRAS](#), **399**, 983
- Bahé Y. M., McCarthy I. G., Balogh M. L., Font A. S., 2013, [MNRAS](#), **430**, 3017
- Balogh M. L., Navarro J. F., Morris S. L., 2000, [ApJ](#), **540**, 113
- Balogh M. L., Baldry I. K., Nichol R., Miller C., Bower R., Glazebrook K., 2004, [ApJ](#), **615**, L101
- Behroozi P. S., Wechsler R. H., Wu H.-Y., 2013a, [ApJ](#), **762**, 109
- Behroozi P. S., Wechsler R. H., Wu H.-Y., Busha M. T., Klypin A. A., Primack J. R., 2013b, [ApJ](#), **763**, 18
- Behroozi P. S., Wechsler R. H., Conroy C., 2013c, [ApJ](#), **770**, 57
- Blanton M. R., Berlind A. A., 2007, [ApJ](#), **664**, 791
- Blanton M. R., Eisenstein D., Hogg D. W., Schlegel D. J., Brinkmann J., 2005, [ApJ](#), **629**, 143
- Bryan G. L., Norman M. L., 1998, [ApJ](#), **495**, 80
- Budzynski J. M., Kuposov S. E., McCarthy I. G., McGee S. L., Belokurov V., 2012, [MNRAS](#), **423**, 104
- Chandrasekhar S., 1943, [ApJ](#), **97**, 255
- Colless M., et al., 2001, [MNRAS](#), **328**, 1039
- Contini E., Kang X., 2015, [MNRAS](#), **453**, L53
- Dressler A., 1980, [ApJ](#), **236**, 351
- Driver S. P., et al., 2011, [MNRAS](#), **413**, 971
- Gabor J. M., Davé R., 2015, [MNRAS](#), **447**, 374
- Gao L., De Lucia G., White S. D. M., Jenkins A., 2004, [MNRAS](#), **352**, L1
- Girardi M., Rigoni E., Mardirossian F., Mezzetti M., 2003, [A&A](#), **406**, 403

- Gonzalez-Perez V., Lacey C. G., Baugh C. M., Lagos C. D. P., Helly J., Campbell D. J. R., Mitchell P. D., 2014, *MNRAS*, **439**, 264
- Gunn J. E., Gott III J. R., 1972, *ApJ*, **176**, 1
- Hahn O., Abel T., 2013, MUSIC: MUlti-Scale Initial Conditions, Astrophysics Source Code Library (ascl:1311.011)
- Hogg D. W., et al., 2004, *ApJ*, **601**, L29
- Hou A., Parker L. C., Harris W. E., 2014, *MNRAS*, **442**, 406
- Hudson M. J., et al., 2015, *MNRAS*, **447**, 298
- Jetley P., Gioachin F., Mendes C., Kale L. V., Quinn T., 2008, in Parallel and Distributed Processing, 2008. IPDPS 2008. IEEE International Symposium on. pp 1–12, doi:10.1109/IPDPS.2008.4536319
- Jetley P., Wesolowski L., Gioachin F., Kal L. V., Quinn T. R., 2010, in 2010 ACM/IEEE International Conference for High Performance Computing, Networking, Storage and Analysis. pp 1–11, doi:10.1109/SC.2010.49
- Joshi G. D., Parker L. C., Wadsley J., 2016, *MNRAS*, **462**, 761
- Kaffe P. R., et al., 2016, *MNRAS*, **463**, 4194
- Kauffmann G., White S. D. M., Heckman T. M., Ménard B., Brinchmann J., Charlot S., Tremonti C., Brinkmann J., 2004, *MNRAS*, **353**, 713
- Kawata D., Mulchaey J. S., 2008, *ApJ*, **672**, L103
- Knebe A., et al., 2011, *MNRAS*, **415**, 2293
- Knollmann S. R., Knebe A., 2009, *ApJS*, **182**, 608
- Lares M., Lambas D. G., Sánchez A. G., 2004, *MNRAS*, **352**, 501
- Larson R. B., Tinsley B. M., Caldwell C. N., 1980, *ApJ*, **237**, 692
- Loken C., et al., 2010, Journal of Physics: Conference Series, 256, 012026
- Makino J., Hut P., 1997, *ApJ*, **481**, 83

- McGee S. L., Balogh M. L., Bower R. G., Font A. S., McCarthy I. G., 2009, [MNRAS](#), **400**, 937
- Menon H., Wesolowski L., Zheng G., Jetley P., Kale L., Quinn T., Governato F., 2015, [Computational Astrophysics and Cosmology](#), **2**, 1
- Moore B., Katz N., Lake G., Dressler A., Oemler A., 1996, [Nature](#), **379**, 613
- Moore B., Lake G., Katz N., 1998, [ApJ](#), **495**, 139
- Oemler Jr. A., 1974, [ApJ](#), **194**, 1
- Ostriker J. P., Tremaine S. D., 1975, [ApJ](#), **202**, L113
- Peñarrubia J., Navarro J. F., McConnachie A. W., 2008, [ApJ](#), **673**, 226
- Planck Collaboration et al., 2014, [A&A](#), **571**, A16
- Roberts I. D., Parker L. C., Joshi G. D., Evans F. A., 2015, [MNRAS](#), **448**, L1
- Schaye J., et al., 2015, [MNRAS](#), **446**, 521
- Smith R., Choi H., Lee J., Rhee J., Sanchez-Janssen R., Yi S. K., 2016, preprint, ([arXiv:1610.04264](#))
- Springel V., et al., 2008, [MNRAS](#), **391**, 1685
- Tremaine S. D., Ostriker J. P., Spitzer Jr. L., 1975, [ApJ](#), **196**, 407
- Wetzel A. R., Tinker J. L., Conroy C., 2012, [MNRAS](#), **424**, 232
- White S. D. M., 1977, [MNRAS](#), **179**, 33
- Ziparo F., et al., 2013, [MNRAS](#), **434**, 3089
- van den Bosch F. C., Pasquali A., Yang X., Mo H. J., Weinmann S., McIntosh D. H., Aquino D., 2008, preprint, ([arXiv:0805.0002](#))
- van den Bosch F. C., Jiang F., Campbell D., Behroozi P., 2016, [MNRAS](#), **455**, 158
- von der Linden A., Wild V., Kauffmann G., White S. D. M., Weinmann S., 2010, [MNRAS](#), **404**, 1231

CHAPTER 4

THE TRAJECTORIES OF GALAXIES
IN GROUPS: MASS LOSS AND
PREPROCESSING

Joshi, Gandhali J., Parker, Laura C., Wadsley, James W., Keller, Benjamin, W., 2017, in preparation for submission to MONTHLY NOTICES OF THE ROYAL ASTRONOMICAL SOCIETY

Abstract

We present a study of a group of galaxies in a high-resolution zoom-in hydrodynamical simulation using the SPH code GASOLINE2. This study extends our previous work on mass loss and preprocessing of dark matter haloes by now incorporating key baryonic processes in galaxy evolution, allowing us to investigate the dark matter, gas and stellar components separately. At the final redshift, we select galaxies within $3 r_{\text{vir}}$ of the group centre and separate them into three subsamples: unaccreted galaxies that have never crossed within the group’s virial radius, single galaxies that were always distinct before crossing, and grouped galaxies that were in an external group before crossing. We find that while unaccreted galaxies continue to grow in mass until the final redshift, single and grouped galaxies lose mass in dark matter and gas, but not in stars, after $z \sim 2$. Tracking single and grouped galaxies individually as a function of their distance from the group centre, we find that both sets of galaxies reach their peak total mass well outside the group’s virial radius, as far out as $\sim 8 - 10 r_{\text{vir}}(z)$. Single galaxies begin losing dark matter and gas mass just outside the group’s virial radius whereas galaxies that infall as part of a smaller group start losing mass at much larger radii, roughly coinciding with when they first become part of an external group. This pattern of mass loss is evidence of the grouped galaxies being preprocessed before being accreted onto the main group. We also examine the role of tidal interactions and ram pressure stripping in driving this mass loss. The consequence of these trends in mass loss is that the unaccreted, single and grouped galaxies each occupy a distinct region of a stellar mass-to-halo mass (SMHM) relation. Our results suggest that preprocessed galaxies may be a key source of scatter in SMHM relations derived using a mix of galaxy populations.

4.1 Introduction

The fate of galaxies as they evolve over time is strongly tied to their environment. Galaxies in dense environments ranging from groups of a few galaxies to clusters of 100s-1000s of galaxies exhibit different properties compared to isolated field galaxies. Group and cluster populations have higher numbers of red, elliptical and quenched galaxies, whereas field populations contain more blue, spiral, star forming galaxies (see e.g. Oemler, 1974; Dressler, 1980; Balogh et al., 2004; Hogg et al., 2004; Kauffmann et al., 2004; Blanton et al., 2005). According to the hierarchical model of the growth of structure in the Universe, larger objects such as groups and clusters are built by the coalescence of smaller objects such as galaxies. As larger and larger structures form, galaxies continue evolving in these environments. Understanding how these galaxies are transformed in larger, denser structures is an important aspect of studying galaxy evolution.

There are several processes by which field galaxies can be transformed as they approach, and are eventually accreted onto, groups and clusters. Some of these processes are the result of a higher frequency of galaxy-galaxy interactions, such as mergers (Makino & Hut, 1997; Angulo et al., 2009) and harassment (Moore et al., 1996, 1998). Others are due to the group/cluster halo itself and the surrounding intra-group or intra-cluster medium (IGM and ICM respectively), which can cause tidal truncation (Toomre & Toomre, 1972; Barnes & Hernquist, 1992; Bournaud et al., 2004), ram pressure stripping (Gunn & Gott, 1972; Abadi et al., 1999) and starvation (Larson et al., 1980; Balogh et al., 2000; Kawata & Mulchaey, 2008). Mergers can cause starbursts where a short period of intense star formation (SF) activity can rapidly deplete the galaxy’s fuel for forming future stars. Harassment results in the heating of the galaxy’s gas, making it less bound and therefore more easily stripped. Tidal truncation due to the group/cluster’s stronger gravitation restricts the galaxy’s own accretion and may also remove mass from the galaxy. Ram pressure stripping is the result of the interaction between the galaxy’s gas content and the surrounding IGM or ICM, which can remove even the more strongly bound cold gas from galaxy. Each of these processes acts on different timescales and is efficient at different positions within the group/cluster halo. These processes also affect the various components of the galaxies differently, and therefore, can lead to signature features in the proportions of dark matter, gas and stellar content in a galaxy.

Galaxies are expected to lose mass in more massive haloes due to some of these environmental effects. Previous studies have examined the degree of halo mass loss of group and cluster galaxies. [Knebe et al. \(2006\)](#) used a suite of zoom-in dark matter simulations of galaxy clusters to show how tidal interactions amongst subhaloes, with each other, can account for $\sim 30\%$ of the mass loss experienced by cluster members. [van den Bosch et al. \(2016\)](#) carried out an extensive study of radial segregation in various properties of subhaloes in the Bolshoi and Chinchilla N-body simulations. They found a significant correlation between the $z = 0$ distance of the subhaloes from the host centre and the amount of mass loss from the time of accretion. [Behroozi et al. \(2014\)](#) also examined the trajectories of galaxy haloes in the Bolshoi simulation and found that haloes can begin losing mass well outside the final host halo, the median distance being $\sim 2 r_{\text{vir}}$ and going as far out as $\sim 4 r_{\text{vir}}$.

Larger clusters are gradually built up through the accretion of smaller groups of galaxies. These galaxies may have already been affected by their group environment, i.e. they may have been preprocessed, before they become a part of the final cluster. Being able to separate the effects of the final cluster from those of the early groups that the galaxies may have been a part of is crucial in determining the efficiency of the various environmental effects. [McGee et al. \(2009\)](#) studied clusters in the Millennium simulation using semi-analytical modelling and found that a large fraction of their galaxies had been accreted as part of smaller groups and were therefore, potentially preprocessed. They also found that the degree of preprocessing was dependent on the galaxies' stellar mass, with more massive galaxies having a higher probability of being preprocessed. [Bahé et al. \(2013\)](#) examined several galaxy properties, and radial trends in such properties, in the GIMIC suite of simulations. They found strong radial trends, in massive clusters, in the fractions of galaxies containing significant amounts of cold and hot gas, as well as in the star-forming fraction. However, they also found that $\sim 50\%$ of the galaxies within such massive clusters had been accreted as part of smaller groups and when these were excluded, the radial trends were significantly weaker. Note however that the degree of preprocessing was lower in smaller groups. [Hou et al. \(2014\)](#) studied groups and clusters using SDSS data and found that galaxies in 'subhaloes', i.e. galaxies in smaller clumps within the group or cluster, had higher quenched fractions beyond $\sim 1.5 - 2 r_{200}$ and that this preprocessing was more important for massive clusters than for smaller groups. [Gabor & Davé \(2015\)](#) used simulations to study galaxy clusters and found that roughly 1/3 of galaxies had

already been quenched in groups of mass $> 10^{12} M_{\odot}$. [Wetzel et al. \(2015\)](#) studied galaxies in the ELVIS suite of dark-matter simulations of the Local Group along with semi-analytical modelling and found that $\sim 25\%$ of all satellites at $z = 0$ had been preprocessed in groups of masses $M_{\text{vir}} > 10^{11} M_{\odot}$ for $0.5 - 3.5$ Gyr. They also showed that preprocessing was more important for faint, low-mass satellites and that satellites closer to the group centre at $z = 0$ were more likely to have been preprocessed.

In our previous work ([Joshi et al., 2017](#)), we investigated the halo mass loss of galaxy analogues in a dark matter simulation. We found that galaxy analogues that had been in a group prior to accretion had lost $\sim 30\%$ more mass, relative to their peak mass, compared to galaxy analogues that were distinct before accretion. After accretion however, both samples of galaxy analogues lost mass with the single galaxies ‘catching up’ by the time they got to within $\sim 0.2 r_{\text{vir}}$. The mass loss was found to strongly correlate with the time spent in a dense environment, be it the final host halo or any previous group halo in which the galaxies may have been preprocessed. In this work, we focus on simulating a single group of galaxies and studying in detail the accretion histories of individual galaxies within and around the group. We specifically examine the mass loss experienced by each galaxy as a result of being part of a group, the impact on star formation, and whether there is evidence for preprocessing of these galaxies. The details of the simulation and selection of galaxies are provided in [Section 4.2](#). In [Section 4.3](#), we examine the average trends in mass loss over cosmic time for galaxies that were accreted onto the main group as single galaxies vs. those that had previously been part of a group. In [Section 4.4](#), we follow the galaxies individually as they approach the group and explore what differences there are in their dark matter, gas and stellar content. We discuss what may be the dominant processes driving the mass evolution of these galaxies in [Section 4.5](#). Finally, we explore the consequences of such evolution on the final properties of our galaxy samples in [Section 4.6](#). We summarize our findings in [Section 4.7](#).

4.2 Methods

4.2.1 Simulation

We ran a high-resolution hydrodynamical zoom-in simulation of a galaxy group using the code GASOLINE2 ([Wadsley et al., 2017](#)). GASOLINE2 is a smoothed particle

hydrodynamics (SPH) code that includes prescriptions for star formation, radiative and metal line gas cooling, supernovae and stellar winds. It also employs the superbubble feedback model of Keller et al. (2014). The group was selected from a lower resolution cosmological N-body simulation run using CHANGA (Jetley et al., 2008, 2010; Menon et al., 2015) in gravity-only mode. This first simulation was comprised of a $(100 \text{ Mpc})^3$ comoving volume containing 1024^3 particles, resulting in a particle mass of $3.7 \times 10^7 M_\odot$. The initial conditions (ICs) were generated at $z = 100$ using the code MUSIC, (Hahn & Abel, 2013) assuming a flat standard Λ CDM cosmology with $\Omega_\Lambda = 0.6914$, $\Omega_m = 0.3086$, $h = 0.6777$, $n_s = 0.9611$ and $\sigma_8 = 0.8288$ (Planck Collaboration et al., 2014). The simulation was run over 1000 timesteps, linear in time, to $z = 0$. We identified haloes in the simulation at $z = 0$ using the phase-space friends-of-friends (FOF) algorithm ROCKSTAR (Behroozi et al., 2013a). One of these final haloes was then chosen for the zoom-in simulation.

As we are interested in the galaxy group regime, we restricted ourselves to distinct isolated haloes with masses within a narrow range of $(2 - 3) \times 10^{13} M_\odot$. This selection resulted in a few tens of groups, of which we excluded those with fewer than three subhaloes. The final group was then selected at random, although we visually confirmed that the group had at least a few subhaloes that were distinct from the group halo and could host galaxies.. The group has a virial mass of $2.7 \times 10^{13} M_\odot$ and a virial radius of 788.6 kpc at $z = 0$. In order to generate ICs for the zoom-in simulation, all particles within $3 r_{vir}$ of the group centre at $z = 0$ were selected and tracked back to their positions in the ICs of the original simulation. Cosmological zoom-in simulations work by identifying the high-redshift Lagrangian progenitor volume of a halo identified at late times. The region that must be refined often has a complex geometry, making the choice of refining volumes non-trivial. Simple spherical regions or convex hulls will often include a factor of 2-5 times more material in the high-resolution volume than actually ends up within the halo, resulting in simulations that are more expensive both in terms of computing time and storage requirements. For this study, we have used a simple, efficient new algorithm for generating zoom-in initial conditions. First, we generate a grid at the lowest refinement/resolution level. Next, grid cells which contain any particles identified as part of the zoom region are set to the highest resolution. Finally, we iterate from the next highest resolution region (a factor of 2 times lower than the previous), setting all neighbours of the higher resolution region to the resolution 2 times lower, repeating until we reach the lowest

resolution of the IC. This gives us a “voxelized” refinement region, with an optimal high-resolution volume surrounded by increasingly lower-resolution shells. We have found this algorithm produces smaller ICs than convex hulls by a factor of 2-3 depending on the IC, and have implemented it in MUSIC. Within the high-resolution region, the dark-matter particle mass is $3.9 \times 10^6 M_\odot$ and the maximum baryon particle mass is $7.2 \times 10^5 M_\odot$. These initial conditions were then used to run the zoom-in hydrodynamical simulation from redshift $z = 100$ to $z = 0.4$ in 696 timesteps, with every eighth snapshot saved. This gives us 87 snapshots equally spaced in time, with consecutive snapshots separated by 107.64 Myr. At the final redshift of 0.4, the group has a virial mass of $1.49 \times 10^{13} M_\odot$ and a virial radius of 486.7 kpc. Its mass in dark matter, gas and stars is $1.23 \times 10^{13} M_\odot$, $1.48 \times 10^{12} M_\odot$ and $1.09 \times 10^{12} M_\odot$ respectively.

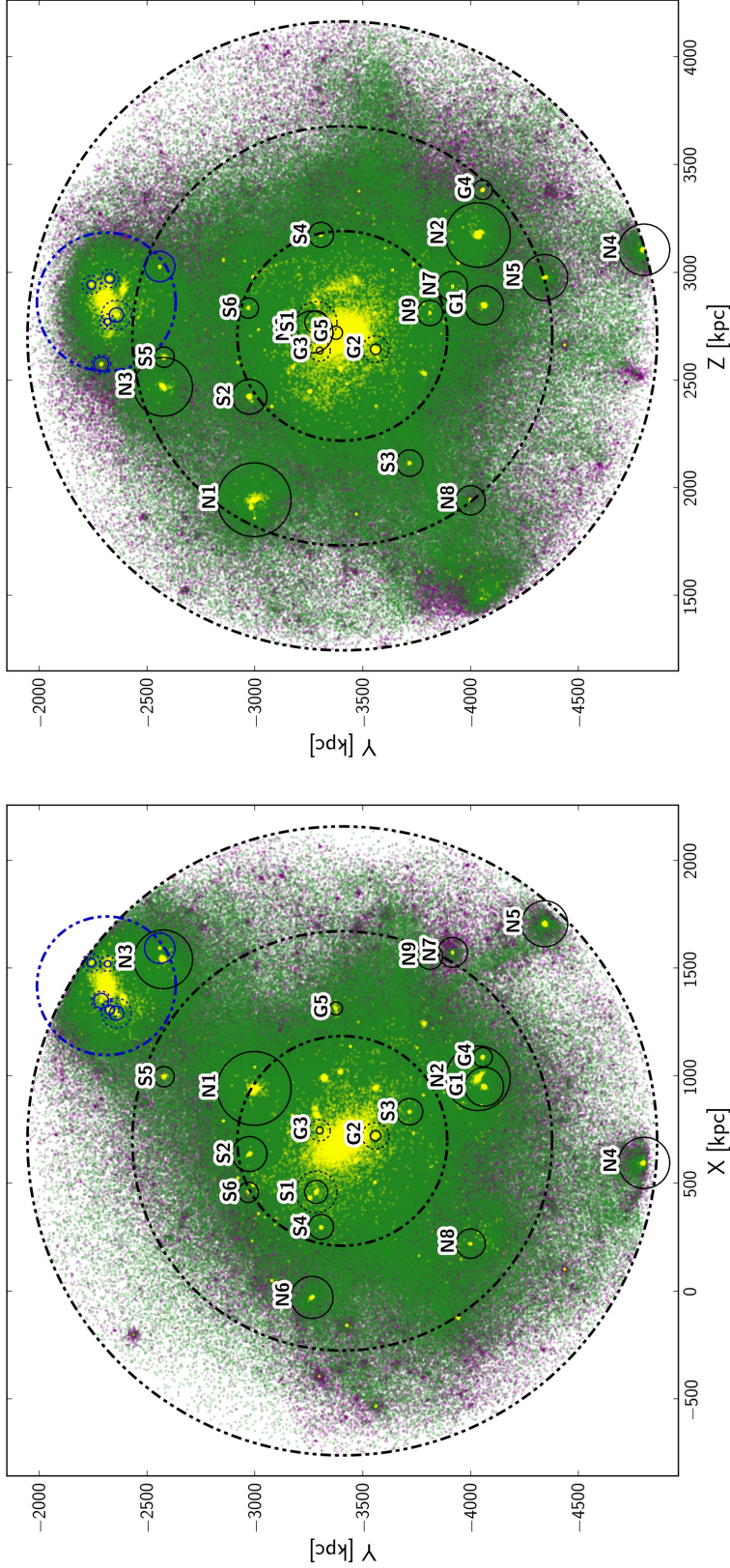


Figure 4.1: Two projections of the group showing its mass distribution and positions of our galaxy samples. The coloured points are particles within $3 r_{\text{virial}}$ of the group; dark matter particles are shown in purple, gas particles in green and star particles in yellow (we only plot every tenth particle for clarity). The black dash-dot lines show r_{virial} , $2 r_{\text{virial}}$ and $3 r_{\text{virial}}$ of the main group. The tidal radius of each galaxy is shown by the black solid circles and their original halo radius is shown by the black dotted circles. Note that in practice, only galaxies within the group’s virial radius are truncated; for all other galaxies, the tidal and virial radii are equal, and hence the dotted and solid circles lie on top of each other. The second external group and its galaxies are shown by the blue circles. This group and its galaxies are excluded from our analysis.

4.2.2 Halo finding and galaxy properties

Haloes were identified within the simulation volume using ROCKSTAR on the dark-matter particles. We then used CONSISTENT TREES (Behroozi et al., 2013b) to generate robust merger trees for the haloes. ROCKSTAR has been shown to be successful at tracking haloes even in dense environments due to its use of particle velocities (Knebe et al., 2011; Behroozi et al., 2013a; Joshi et al., 2016, e.g.), and therefore, we can reliably use the positions and velocities provided in the halo catalogue. Although ROCKSTAR is a FOF algorithm, it provides several spherical overdensity properties for the haloes. The halo radius, $r_{\text{halo}} \equiv r_{\text{vir}}$, is defined as the radius within which the average density is Δ_c times the critical density of the Universe. The overdensity factor Δ_c is defined as per the estimate of Bryan & Norman (1998) as:

$$\Delta_c = 18\pi^2 + 82x - 39x^2 \quad (4.1)$$

where

$$x = \frac{\Omega_{\text{m},0}(1+z)^3}{\Omega_{\text{m},0}(1+z)^3 + \Omega_\Lambda} - 1 \quad (4.2)$$

For the cosmological parameters used in this study, $\Delta_c = 133$ at $z = 0.4$ ($\Delta_c = 102$ at $z = 0$).

Following the halo finding process, we assigned baryonic particles to the haloes in a consistent manner. ROCKSTAR generates an extensive hierarchy of subhaloes, subsubhaloes etc. Each subhalo is at least partially, if not completely, contained within its host halo and even haloes at equal levels in the hierarchy can partially overlap with each other. We therefore chose to use the tidal radius to cleanly separate the volume claimed by each halo and uniquely identify particles belonging to it. The process is as follows.

- (i) We first select all haloes within the catalogue for the final snapshot with $M_{\text{halo}} > 10^9 M_\odot$, that lie within $3r_{\text{halo}}$ of the main group.
- (ii) For each of these haloes that is not a distinct halo (we use the term ‘distinct’ halo to refer to the ones that are not subhaloes of any other halo), we determine a tidal radius r_t where

$$\frac{GM_{\text{halo}}(r_t)}{r_t^2} = \frac{GM_{\text{host}}(d-r_t)}{(d-r_t)^2} - \frac{GM_{\text{host}}(d)}{d^2}. \quad (4.3)$$

Here M_{halo} and M_{host} are the mass of the halo and its host within the specified radius and d is the distance between their centres. Note that we use both the direct parent halo and the halo at the top of the hierarchy as ‘host’ and use the smaller of the two radii thus calculated. For distinct haloes, we use r_{halo} as the tidal radius. This ensures that $r_{\text{tid}} \equiv r_{\text{vir}}$ until a galaxy enters a group, after which it may be truncated.

- (iii) Next we select all particles within the tidal radius for each halo and determine which of them are bound to the halo, i.e. which of them have

$$\frac{1}{2}v^2 - \frac{GM_{\text{halo}}(r)}{r} < 0 \quad (4.4)$$

where v is the velocity of the particles relative to the halo. These bound particles are then assigned to the halo.

- (iv) Finally, we resolve any cases where haloes at the same level in the hierarchy have particles in common. In such cases, we calculate each common particle’s energy as in eq. 4.4 w.r.t. to both haloes and assign it to the halo w.r.t. which its energy is lower.
- (v) We then use these final assigned particles to measure all properties such as total mass and mass in dark matter, gas and stars.

The tidal radii we calculate can fluctuate substantially within the group, since nearby haloes in the group can cause the radii to change sharply from step to step. This in turn would cause the total mass within the tidal radius to fluctuate significantly. By only using bound particles to calculate galaxy masses, we avoid this problem to a large degree. Note that this process results in the central galaxy in the group being assigned to the group halo itself and not treated as a separate subhalo within the group. Starting with 400 haloes within the halo catalogue that met criterion (i), we then select haloes that have a stellar mass $M_* > 10^7 M_\odot$ for a total of 83 galaxy candidates. We initially use this lower limit of $10^7 M_\odot$ to ensure we do not miss any galaxies. A stellar mass of $10^7 M_\odot$ is resolved by at least 14 star particles.

The next stage is to track these galaxies through all of the previous snapshots. In order to do so, we first carry out a similar process to determine tidal radii for the haloes at each of the previous snapshots. Instead of criterion (i) above, for each

galaxy candidate in snapshot $(n + 1)$, we consider every progenitor in snapshot n with $M_{\text{halo}} > 10^8 M_{\odot}$. We then carry out steps (ii)-(v) on these progenitors. Finally, we keep any galaxies with a total mass of $M_{\text{tot}} > 10^8 M_{\odot}$, since this limit ensures that the galaxies are resolved by > 100 star particles. Once the tidal radii and other galaxy properties have been calculated for each snapshot, we generate galaxy histories for each of the galaxy candidates at $z = 0.4$ by following their most massive progenitor at every step. For our final sample of galaxies, we keep those galaxies that had a stellar mass of $M_* > 10^8 M_{\odot}$ at some point along their history. This gives us a total of 27 galaxies, including the central galaxy in the main group, as well as the central galaxy within a nearby group.

Since we are interested in the effects of preprocessing, we separate the galaxies into three categories.

1. **Never accreted:** Galaxies that have been distinct haloes for their entire history (hereafter referred to as ‘unaccreted’ galaxies). 11 galaxies fall into this category.
2. **Single accretion:** Galaxies that were distinct haloes for their entire history before they were accreted by the main group (hereafter referred to as ‘single’ galaxies). 5 galaxies fall into this category.
3. **Grouped accretion:** Galaxies that were part of a different group for some time before they were accreted by the main group (hereafter referred to as ‘grouped’ galaxies). 5 galaxies fall into this category.

6 other galaxies were never accreted by the main group, but were part of a different group at some point in their history. These galaxies, as well as the main group central, were not the focus of this study and are therefore not included in further analysis. Fig. 4.1 shows the distribution of particles in the group as well as the galaxies in our sample. Table 4.1 provides key details regarding our galaxy sample.

Table 4.1: Galaxy properties for the never accreted, singly-accreted and group-accreted samples. The reported radii and masses [cols 2-6] are at the final redshift of $z = 0.4$. r_{\min} is the closest distance to the main group that the galaxy reaches (normalized by the group’s tidal radius at the time). z_{cross} is the redshift at which the single and grouped galaxies first cross within the tidal radius of the group and z_{group} is the redshift at which the grouped galaxies first become part of a group (that is not part of the main group’s subhalo hierarchy).

Label	r_{tidal} [kpc]	M_{tot} [$10^{10} M_{\odot}$]	M_{dm} [$10^{10} M_{\odot}$]	M_{gas} [$10^8 M_{\odot}$]	M_{star} [$10^8 M_{\odot}$]	r_{\min} [r_{central}]	z_{cross}	z_{group}
Never accreted								
N1	171.2	58.84	48.78	903.36	102.75	1.84	-	-
N2	150.0	37.57	31.85	539.22	32.66	1.72	-	-
N3	136.3	28.93	24.63	395.99	34.02	2.48	-	-
N4	118.9	18.02	15.77	208.63	15.57	3.00	-	-
N5	106.8	12.85	11.46	127.82	10.39	2.88	-	-
N6	97.7	9.01	8.16	79.12	5.76	1.46	-	-
N7	69.2	3.48	3.24	23.49	1.01	2.14	-	-
N8	68.1	3.19	2.97	20.35	1.80	2.21	-	-
N9	59.1	2.19	1.94	23.41	1.11	1.96	-	-
Single accretion								
S1	53.5	5.79	5.24	44.10	10.71	0.34	0.5	-
S2	81.0	5.47	4.95	46.72	5.69	0.59	0.6	-
S3	61.3	2.20	2.16	1.44	1.86	0.54	0.8	-
S4	57.8	1.83	1.76	5.33	1.61	0.36	0.8	-
S5	47.4	1.07	1.01	3.70	2.39	0.21	1.0	-
Grouped accretion								
G1	90.3	7.61	6.93	40.39	27.53	0.77	0.9	1.2
G2	24.3	1.99	1.76	6.26	16.74	0.30	1.4	1.6
G3	15.8	0.81	0.76	0.00	5.20	0.24	0.9	2.5
G4	44.6	0.87	0.82	1.42	3.69	0.42	0.9	1.7
G5	30.5	0.24	0.23	0.00	1.25	0.65	0.8	1.3

Table 4.2: Galaxy properties at z_{peak} , the redshift at which the galaxy’s total mass is at its peak value. r_{peak} is the galaxy’s distance from the main group (normalized by the group’s tidal radius at the time).

Label	z_{peak}	r_{peak} [r_{central}]	r_{tidal} [kpc]	M_{tot} [$10^{10} M_{\odot}$]	M_{dm} [$10^{10} M_{\odot}$]	M_{gas} [$10^8 M_{\odot}$]	M_{star} [$10^8 M_{\odot}$]
Never accreted							
N1	0.4	1.84	171.2	58.84	48.78	903.36	102.75
N2	0.5	2.29	142.6	38.01	32.19	550.84	31.43
N3	0.4	2.48	136.3	28.93	24.63	395.99	34.02
N4	0.6	3.44	109.9	18.44	16.13	220.13	11.03
N5	0.4	2.88	106.8	12.85	11.46	127.82	10.39
N6	0.4	1.51	97.6	9.11	8.25	79.94	6.13
N7	1.1	3.25	55.3	4.01	3.57	43.59	0.68
N8	0.8	3.61	56.2	3.34	2.99	34.14	1.26
N9	0.4	1.96	59.1	2.19	1.94	23.41	1.11
Single accretion							
S1	0.6	1.38	88.1	9.61	8.35	118.75	7.93
S2	0.8	1.59	71.9	7.19	6.22	93.77	4.16
S3	0.9	1.50	52.0	3.07	2.96	8.95	1.95
S4	1.0	2.16	50.2	2.99	2.71	27.18	1.30
S5	1.0	1.30	49.6	3.31	2.96	33.07	2.37
Grouped accretion							
G1	1.2	2.30	73.6	13.98	12.27	149.74	20.65
G2	2.3	4.86	51.8	12.08	9.80	219.50	8.37
G3	2.5	11.49	34.2	4.84	4.17	63.71	2.78
G4	2.9	13.79	30.6	3.06	2.46	57.98	2.08
G5	1.3	2.61	43.3	3.25	2.81	42.96	1.42

4.3 Evolution of galaxy properties

We first examine the average evolution of galaxy properties for the unaccreted, singly accreted and group accreted galaxy samples. Fig. 4.2 shows the average (physical) tidal radius of galaxies in each sample as a function of the age of the Universe. According to our definition, unaccreted galaxies are never truncated; single and grouped galaxies, however, show significant tidal truncation, roughly coinciding with when they become part of the main group (indicated by the grey shaded regions). Grouped galaxies appear to be mildly more truncated than single galaxies, most likely due to the smaller external groups they were a part of.

In Fig. 4.3, we show the evolution of the galaxies’ mass in dark matter, gas and stars. Unaccreted galaxies continue to grow in mass in all three components with time. By comparison, in dark matter and gas, single galaxies maintain a roughly constant mass after $z \sim 2$, with some mass loss seen in the last ~ 1 Gyr; grouped galaxies are seen to lose mass after reaching a peak value at $z \sim 2$. The same trend is not seen in stellar mass however; in fact, single galaxies continue to grow in stellar mass whereas grouped galaxies have a nearly constant stellar mass (i.e. at least not decreasing) after $z \sim 2$. These results indicate that while tidal stripping is efficient at removing the dark matter and gas content of galaxies, it does not affect the stellar content to the same degree. This is to be expected since tidal stripping is a process that works outside-in, first affecting the outskirts of the galaxy, and gradually moving inwards. It will therefore remove the more extended dark matter and gas components before reaching the more compact and tightly bound stellar component. Additionally, grouped galaxies appear to lose relatively more mass in gas than in dark matter, which could indicate which of the evolutionary processes is important for these galaxies (see Section 4.5). One other feature seen in each panel of Fig. 4.3 is that the grouped galaxies appear to build their mass early, compared to both the single and unaccreted galaxies. The rapid growth of the grouped galaxies seen in the first ~ 1.2 Gyr is simply a consequence of their being in larger overdensities. As we show in Section 4.4, our sample of grouped galaxies is more massive compared to the single galaxy sample at early times ($z \sim 5$) by nearly an order of magnitude.

We next look at the details of the galaxies’ gas content and star formation. Fig. 4.4 shows the average mass in cold and hot gas, where we use 10^5K as the temperature at which we separate the two components. Note that the ‘cold’ gas includes what might

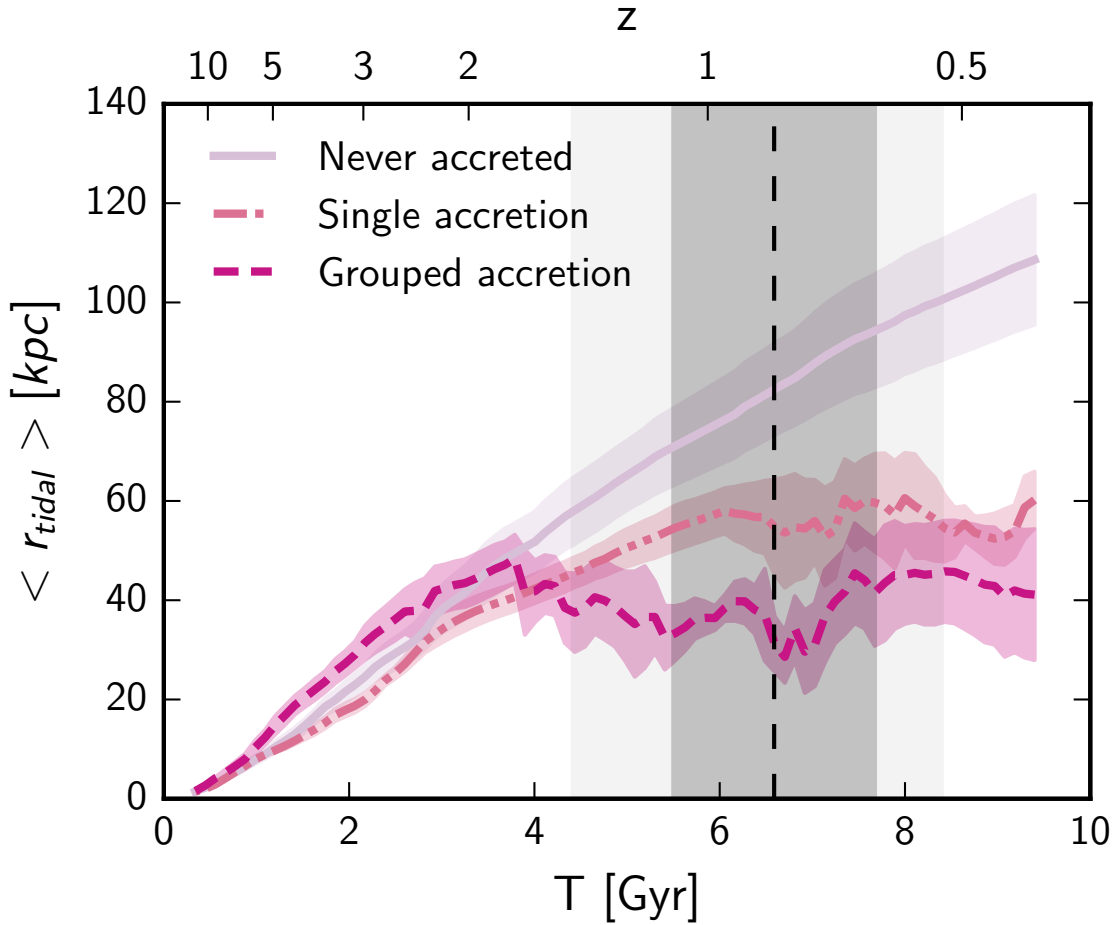


Figure 4.2: Average galaxy tidal radius as a function of time for each category. The pink shaded regions show the standard uncertainty in the mean (note that the spread of the data is larger). The grey shaded regions indicate the time when the single and grouped galaxies first crossed within r_{tidal} of the main group – the black dashed line is the average time of crossing, the darker grey region is the 1σ range and the lighter region is the full range.

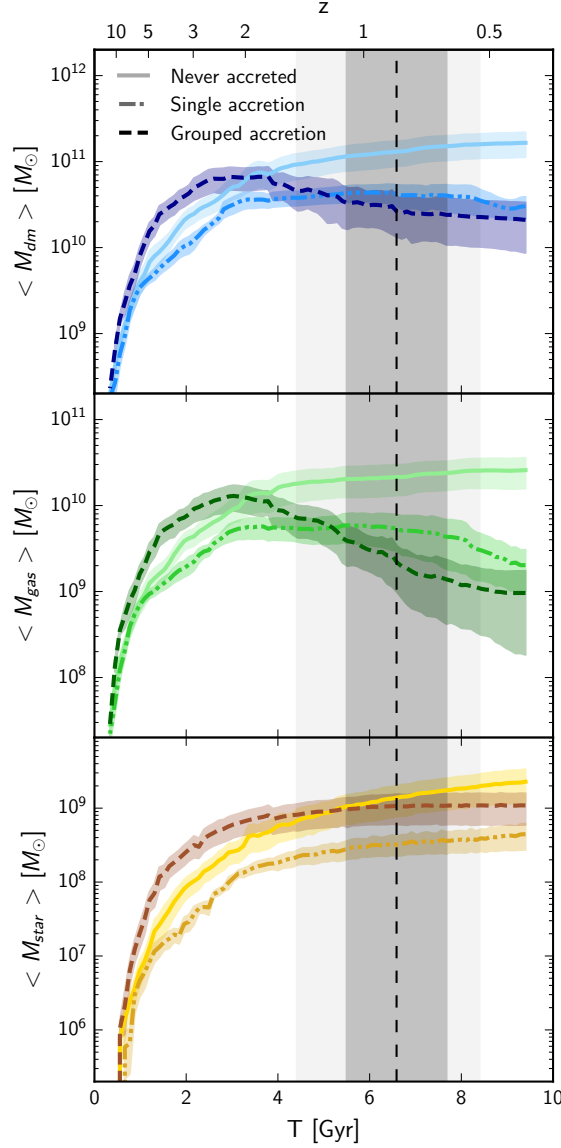


Figure 4.3: Average mass in dark matter (top), gas (middle) and stars (bottom) as a function of time for each category. In each panel, the darkest colour shows the grouped galaxies, the intermediate colour shows the single galaxies and the lightest colour shows the unaccreted galaxies. The coloured shaded regions show the standard uncertainty in the mean (note that the spread of the data is larger). The grey shaded regions indicate time of crossing for the single and grouped galaxies as in Fig. 4.2. While the single and grouped galaxies lose mass in gas and dark matter after reaching a peak value, their stellar mass is not affected.

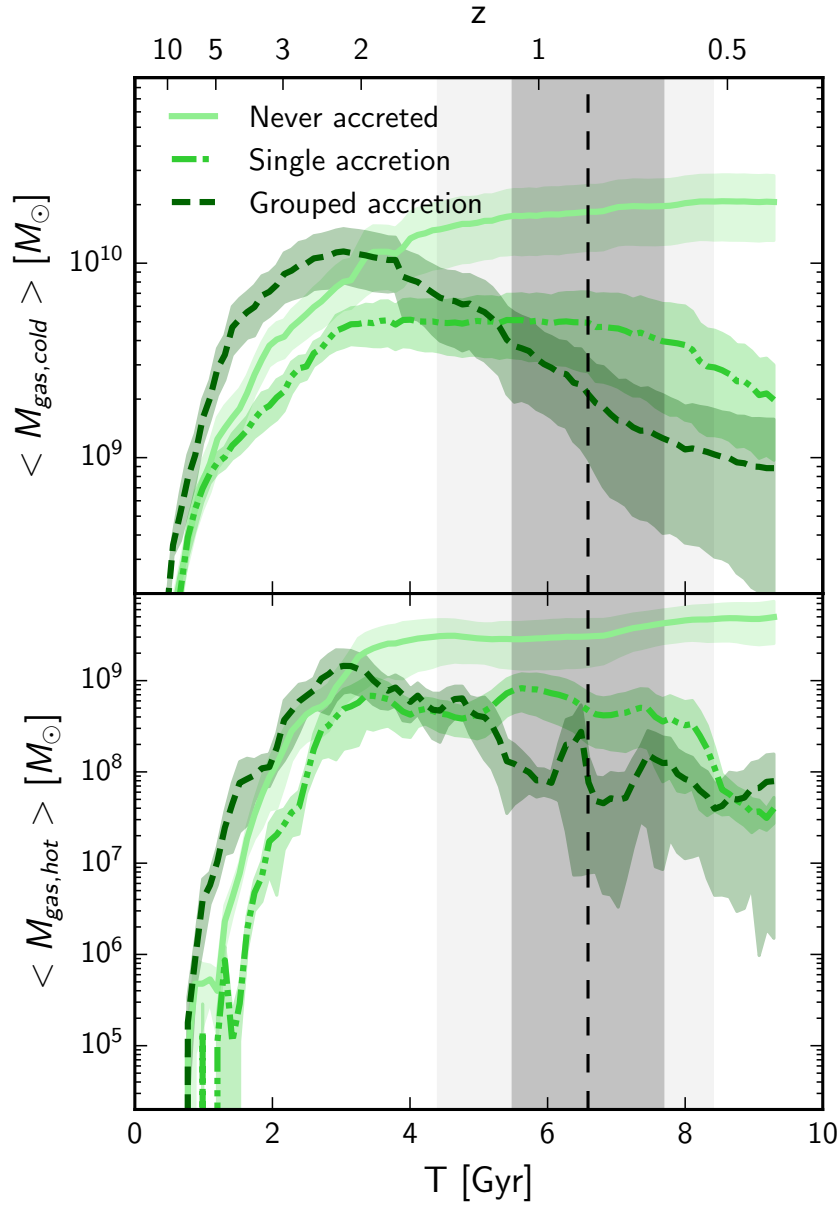


Figure 4.4: Average mass in cold gas (top) and hot gas (bottom) as a function of time for each category. The coloured shaded regions are standard uncertainty in the mean. The grey shaded regions indicate time of crossing for the single and grouped galaxies as in Fig. 4.2. Note that the hot gas masses span a larger range than the cold gas masses.

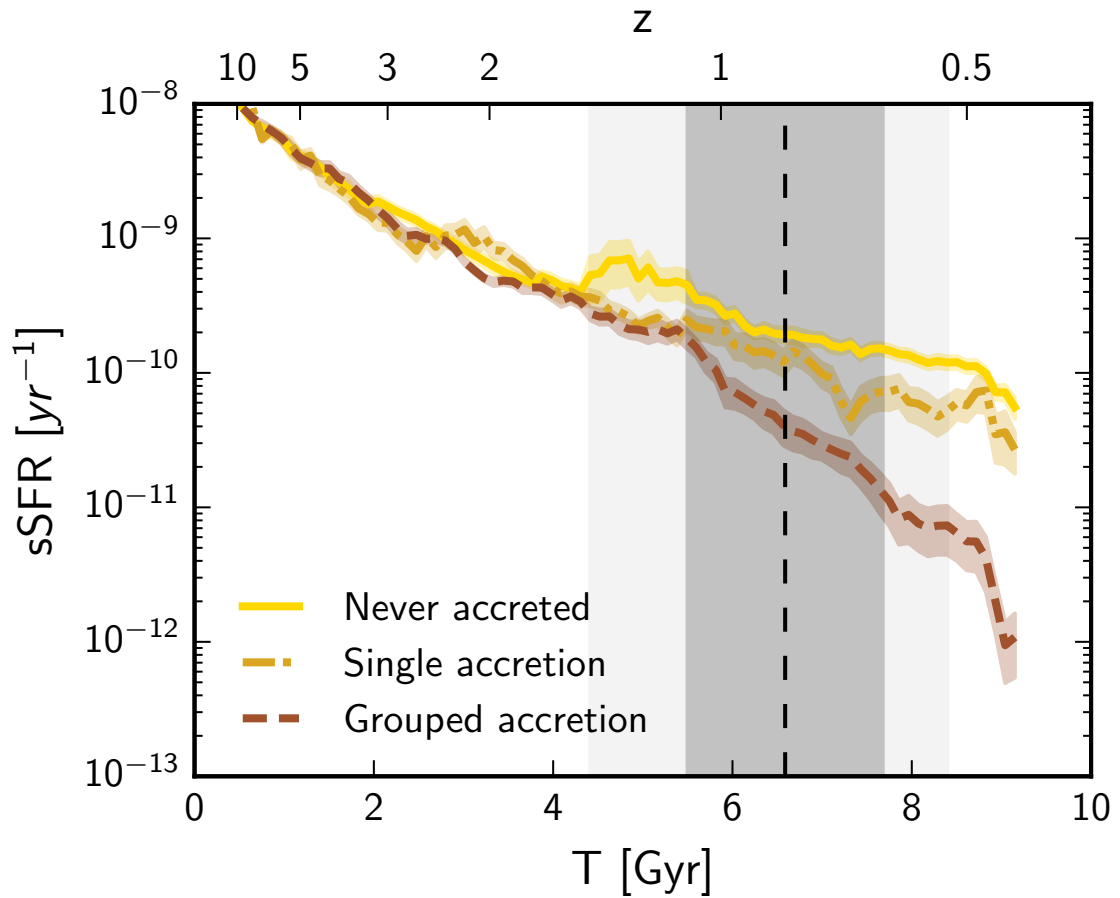


Figure 4.5: Average sSFR as a function of time for each category. The coloured shaded regions are standard uncertainty in the mean. The grey shaded regions indicate time of crossing for the single and grouped galaxies as in Fig. 4.2. The data have been smoothed using a moving average of width 5 for clarity.

be considered the warm ISM component of a galaxy along with the truly cold neutral medium. The cold gas is the larger gas component by mass, accounting for nearly all of the gas content of the galaxies, and hence its evolution is effectively the evolution of the total gas mass. This means that the galaxies are gradually being depleted of their fuel for star formation on fairly long timescales. The hot gas component also shows the same qualitative trends – unaccreted galaxies continue to grow in mass (at a lower rate in hot gas than in cold); grouped galaxies lose mass rapidly after $z \sim 2$, while single galaxies have a roughly constant mass after $z \sim 2$ with some mass loss in the final ~ 1 Gyr.

This naturally leads us to the evolution of the average star formation rate (SFR) of the galaxies. We examined the trends in average SFR (not shown) and similarly found that unaccreted galaxies maintain an approximately constant SFR after $z \sim 2$ while single galaxies show a mild and gradual decrease in SFR after $z \sim 2$. Grouped galaxies initially rise to a slightly higher SFR than either of the other two categories, but show a more rapid and larger decrease compared to single galaxies after $z \sim 2$. We have a large range in galaxy masses and since the grouped galaxies are more massive than the single galaxies at early times, the specific star formation rate (sSFR) is a better indicator of the relative star formation in these galaxies. In Fig. 4.5, we can see that all three galaxy samples begin with the same sSFR of $\sim 5 \times 10^{-9} \text{ yr}^{-1}$ at $z \sim 5$ and show similar rates of decline, consistent with the cosmic decline in star formation until $z \sim 1.5$ (e.g. see Behroozi et al., 2013c; Madau & Dickinson, 2014). The sSFR of unaccreted galaxies then continues to decline at a similar rate, while the single galaxies' sSFR is consistently lower than that of unaccreted galaxies and the grouped galaxies sSFR declines at a significantly more rapid rate. Interestingly, we do not see any sudden discontinuities in sSFR for either single or grouped galaxies, though this is partly a consequence of averaging over galaxies that have been accreted at different redshifts (see Section 4.4).

We have investigated the cause for the overall trend of steadily declining sSFRs for all three populations. The SFR and stellar mass for all three populations show a similar evolution until $z \sim 2$ – both quantities rise rapidly with the increase in stellar mass steeper than in SFR, leading to a steadily declining sSFR. After $z \sim 2$, the stellar mass continues to grow at a much slower rate, eventually flattening to a nearly constant value for all three populations; the SFR on the other hand gradually declines, with the rates of decline steepest for grouped galaxies and shallowest for

unaccreted galaxies. This explains the continuing decline in sSFR and the differences seen between the rates of decline for the three populations after $z \sim 2$. Note that the slight bump in sSFR at $z \sim 1.5$ was found to be caused by a single galaxy, N7, which was found to have started star formation much later than any of the unaccreted, single or grouped galaxies in our sample. While we can trace its dark matter and gas content to ~ 0.5 Gyr from the beginning of the simulation, it only begins star formation at ~ 4 Gyr. It therefore has a much higher sSFR for $\sim 1 - 2$ Gyr after the beginning of star formation, when its stellar mass is low.

Since we explicitly define tidal radii to determine the masses of our galaxies, the mass loss we see, especially in the case of dark matter, is predominantly due to tidal stripping. Any additional mass loss can partly be explained as the consumption of gas by star formation, while the rest may be due to other processes such as ram pressure stripping, which we explore in Section 4.5. Figs. 4.3, 4.4 and 4.5 indicate that tidal stripping causes significant mass loss for single and grouped galaxies due to their dense environment and that while this tidal stripping does not cause stellar mass loss, the reduced overall mass does appear to affect the grouped galaxies' sSFRs.

4.4 Radial trajectories

The efficiency of each of the processes that can affect the single and grouped galaxies within the main group is dependent on their position with respect to the group halo. Therefore, following the trajectories of these galaxies can shed light on how their properties are affected by their proximity to the group.

In Fig. 4.6, we show the evolution of the galaxies' mass in dark matter (top panels), gas (middle panels) and stars (bottom panels) as a function of their distance from the main group centre, normalized by the group radius at the time, r_{central} . The top panels show how single galaxies (left) grow in dark matter mass at early times, then remain at a nearly constant mass starting from $(1 - 3)r_{\text{central}}$ and occasionally as far out as $(8 - 10)r_{\text{central}}$, eventually beginning to lose some mass after they cross within r_{central} (see Section 1.3.2.1). Grouped galaxies (right), in contrast, begin losing mass well outside the group, roughly coinciding with when they first become part of an external group. Since tidal truncation is the primary mode for loss of dark matter, this result suggests that it is an important process. The middle panels show mass in gas for the galaxies and qualitatively, we see similar results, although there

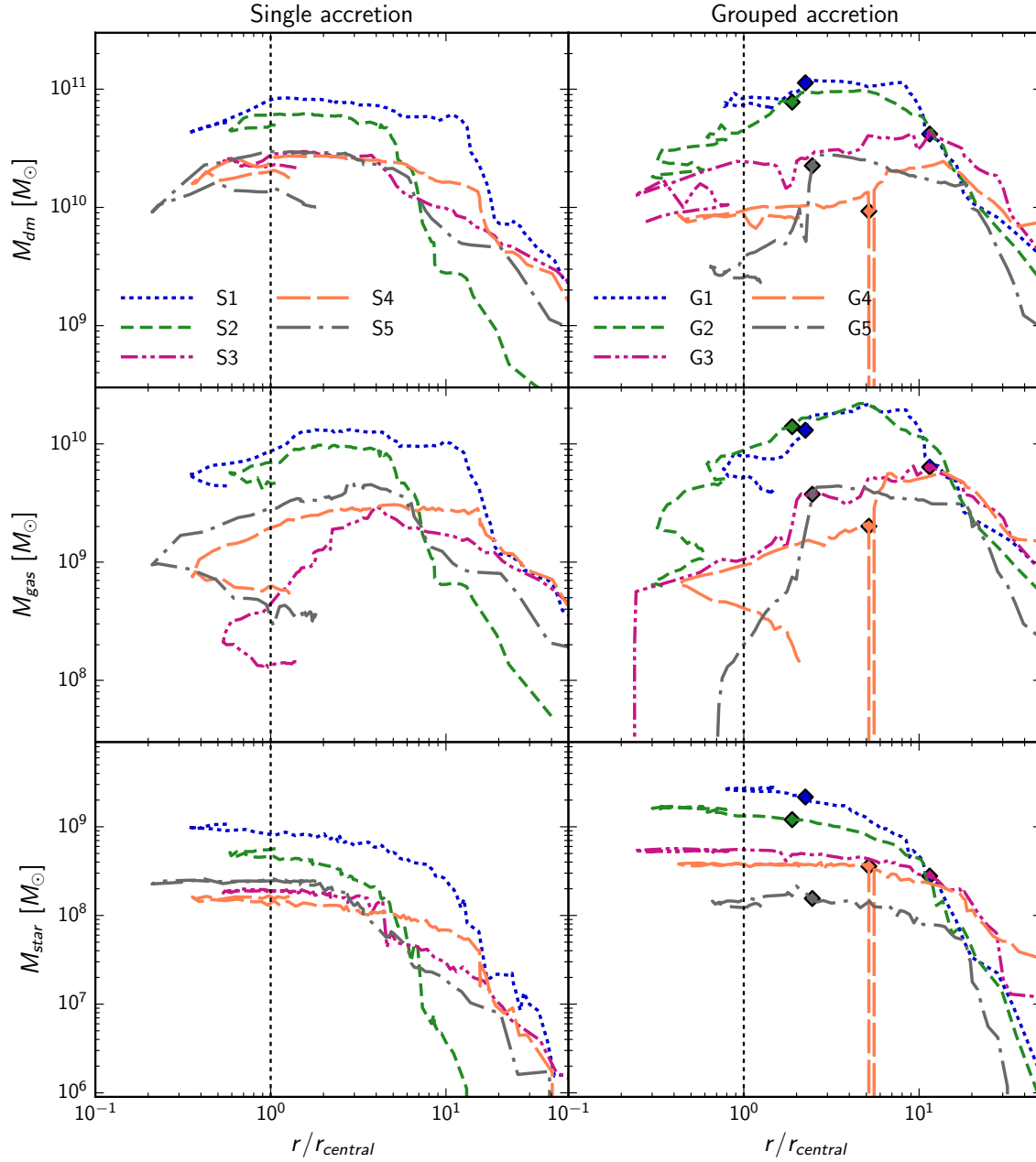


Figure 4.6: Mass in dark matter (top), gas (middle) and stars (bottom) for each of the galaxies as a function of their distance from the main group’s centre, normalized by the group’s tidal radius at the time. Different linestyles and colours are used to differentiate each galaxy. The black dashed line indicates $r = r_{central}$. For the grouped galaxies, we also indicate the first time they become part of a group with diamond symbols.

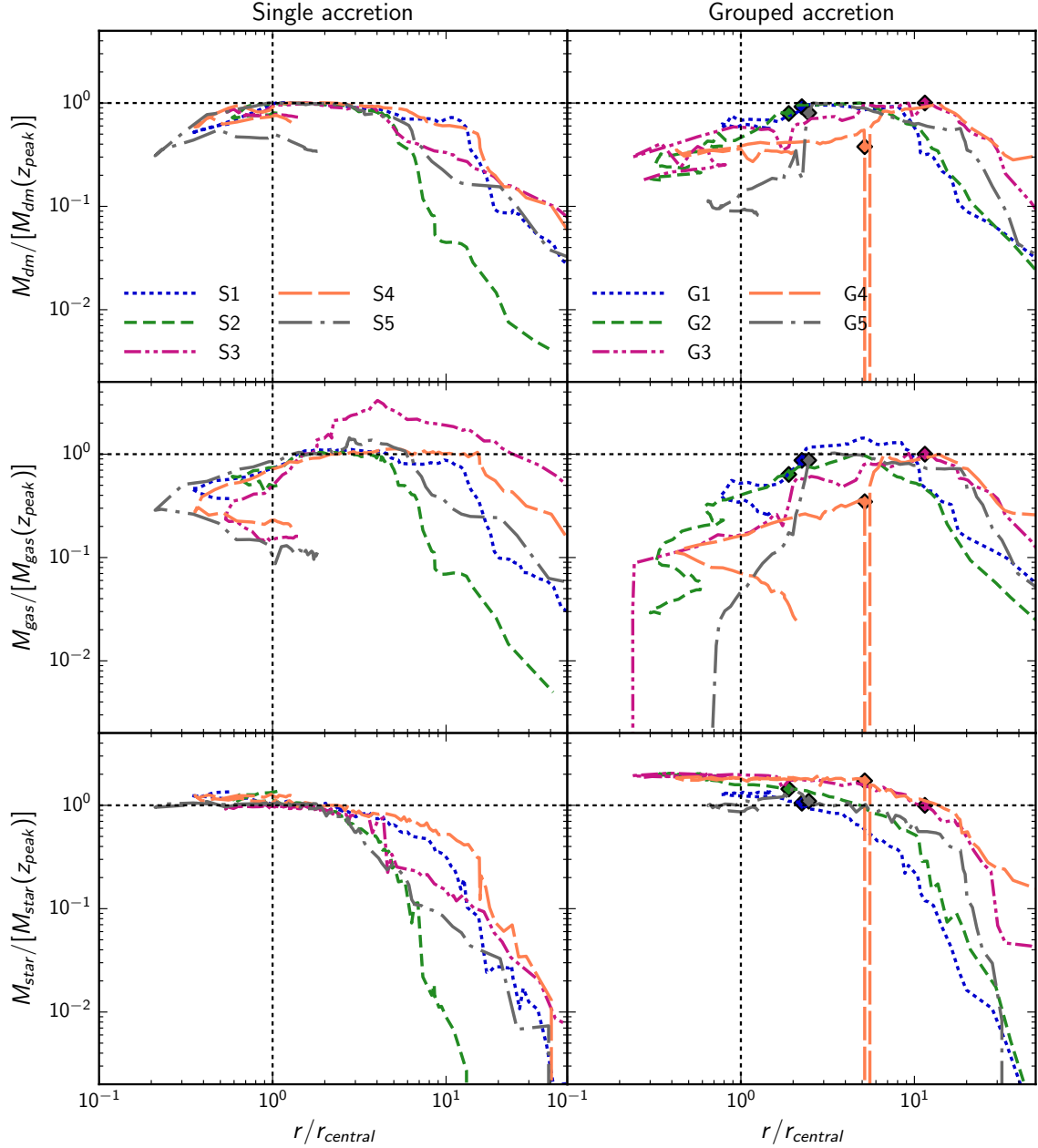


Figure 4.7: Mass in dark matter (top), gas (middle) and stars (bottom), normalized by the corresponding value at z_{peak} , for each of the galaxies as a function of their distance from the main group’s centre, normalized by the group’s tidal radius at the time. Colours and linestyles are the same as in Fig. 4.6. The black dashed line indicates r_{central} . For the grouped galaxies, we also indicate the first time they become part of a group with diamond symbols.

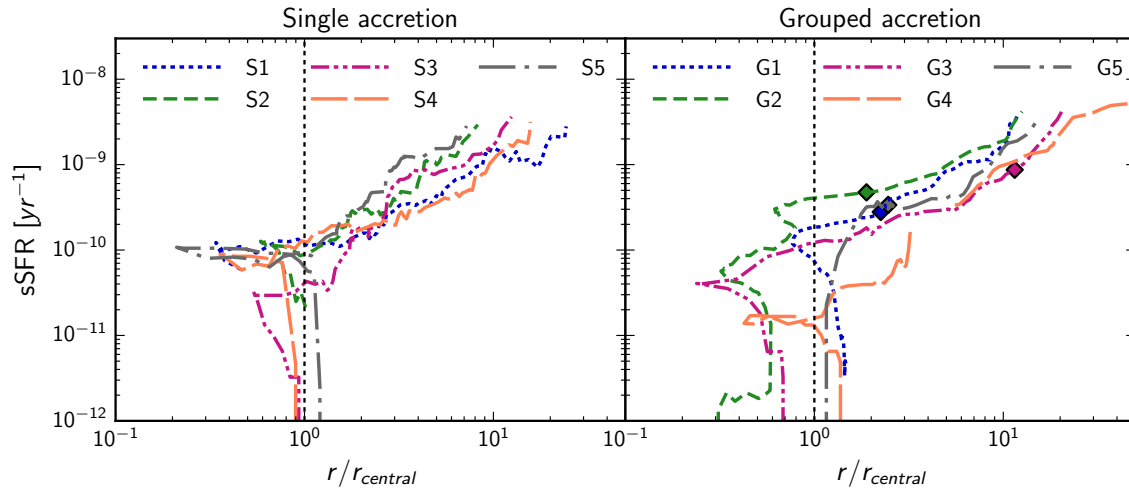


Figure 4.8: sSFR of each of the galaxies as a function of their distance from the main group’s centre, normalized by the group’s tidal radius. Colours and linestyles are the same as in Fig. 4.6. The data have been smoothed using a moving average of width 10 for clarity.

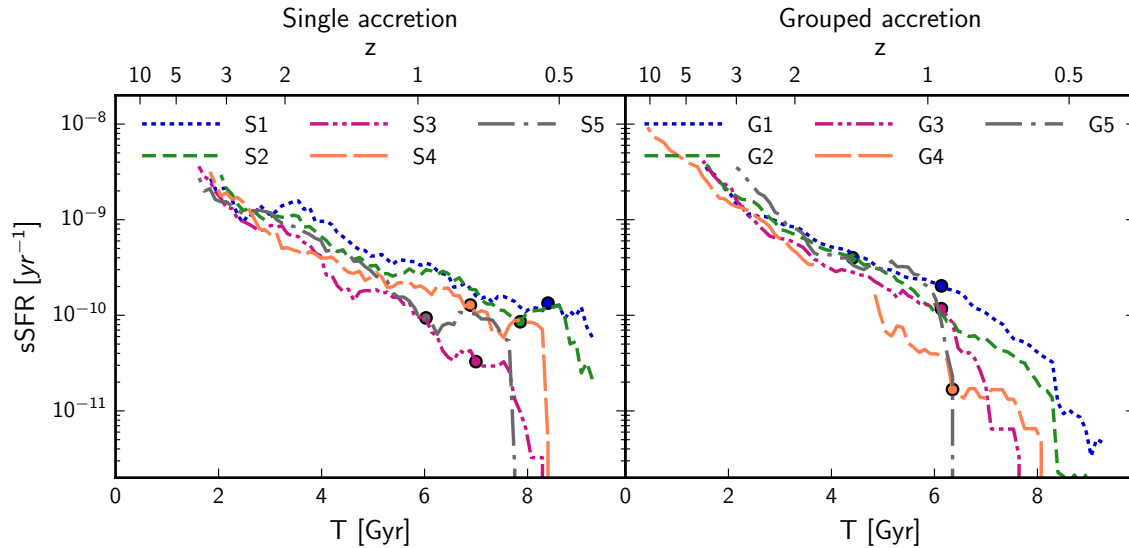


Figure 4.9: sSFR of each galaxy as a function of cosmic time. Colours and linestyles are the same as in Fig. 4.6. The circular symbols indicate when the galaxies first crossed within the main group’s tidal radius. The data have been smoothed using a moving average of width 10.

is significant mass loss seen even for single galaxies starting beyond r_{central} . Again, grouped galaxies lose relatively more mass compared to single galaxies. The bottom panels show explicitly what was found in Fig. 4.3, i.e. the galaxies retain their stellar mass even after crossing r_{central} or being accreted by an external group, and some even show a modest growth in stellar mass. Note that the sharp drop in mass seen for galaxy G4 is unphysical – at that point in its trajectory, the galaxy is nearly coincident with the centre of the external group it is a part of, and the tidal radius we calculate for the galaxy is very small. At later timesteps, the galaxy’s tidal radius returns to roughly the value it had prior to passing through the group centre. The galaxy can be tracked before and after this time by ROCKSTAR and CONSISTENT TREES.

Since the masses in our galaxy sample span a large range, normalizing them by a particular mass helps highlight these trends. One choice for this normalization mass is the peak mass. We choose to define ‘peak’ as the time at which the galaxy’s total mass is at its highest value. Table 4.2 provides key properties of the galaxies at z_{peak} . Fig. 4.7 shows the same trajectories as Fig. 4.6, with the masses now normalized by their respective values at z_{peak} . The top panels now show more clearly how the single galaxies’ dark matter masses remain nearly constant after peak until they cross within r_{central} . Grouped galaxies are accreted by external groups soon after they reach their peak mass, and begin mass loss soon after this. The degree of total mass loss since peak is higher for grouped galaxies than for single galaxies. The middle panels of Fig. 4.7 show qualitatively the same trends for gas mass. They also confirm that the peak in total mass (which is dominated by dark matter) is the approximate peak in gas mass as well, since there is little to no increase in gas mass after this point. The bottom panels show that both galaxy samples continue growing in stellar mass after peak. While it appears that the stellar mass of grouped galaxies grows more than that of single galaxies, this is only due to the fact that the grouped galaxies have higher z_{peak} values. Thus, the time interval between z_{peak} and the final snapshot, during which the galaxies continue growing in stellar mass, is longer for the grouped galaxies.

We show the sSFRs of these galaxies in Fig. 4.8, which confirms explicitly some of the findings from results shown in Fig. 4.5. The sSFRs for both sets of galaxies gradually decline as they approach the main group. Grouped galaxies do not show a sudden drop in sSFR when they are accreted by external groups. Contrary to what was seen in Fig. 4.5 however, several of the galaxies do show a sharp decline in sSFR

some time after entering the main group. It must be kept in mind that there is no one-to-one correlation between the galaxies' distance from the group and cosmic time and what appears as a rapid decline could be occurring over a larger time interval. We therefore also show the sSFRs as a function of time in Fig. 4.9. The sSFRs for both single and grouped galaxies show a sharp decline, indicating rapid quenching, after a delay ranging from $\sim (0.5 - 2)$ Gyr after accretion onto the main group. Although this is only a small sample of galaxies in one group, these results are consistent with recent proposed models of quenching after a delay of $(2 - 3)$ Gyr after accretion. (e.g. [Wetzel et al., 2013](#); [Schawinski et al., 2014](#); [Balogh et al., 2016](#); [Oman & Hudson, 2016](#)). It is important to note that the grouped galaxies do not quench in their external groups, implying that the mass of the group is a significant factor in determining whether or not a galaxy is quenched in that environment.

4.5 Mass loss mechanisms

As mentioned in the introduction, several environmental mechanisms can result in the evolution of properties we see for both single and grouped galaxies. While the loss of dark matter can largely be attributed to tidal truncation, the loss of gas mass could be the result of a combination of processes. In order to disentangle which of these mechanisms is active in this system, we examine the differences between the dark matter and gas components of our galaxies. In Fig. 4.10, we show the ratio of gas mass to dark matter mass for each galaxy. Note that at all times, at least 80% and often 90% of the gas content of all galaxies in our sample is in cold gas. We therefore do not show the two components separately, since the results for cold gas are similar to the results in Fig. 4.10 and while there is significant loss of hot gas, it is a small contribution to the overall loss of gas mass. In all cases, we find that the gas to dark matter ratio remains nearly constant or shows a mild decrease as the galaxies approach the main group until they are within $\sim (3 - 5) r_{\text{central}}$, after which the decrease is steeper. With the exception of galaxy S3, there is little difference between the single and grouped galaxies and we see no significant change when the grouped galaxies are first accreted onto external groups. Some of this decrease can be attributed to star formation, but the region where the gas to dark matter ratio decreases most severely, around $(2 - 3) r_{\text{central}}$ from the group centre, is also where

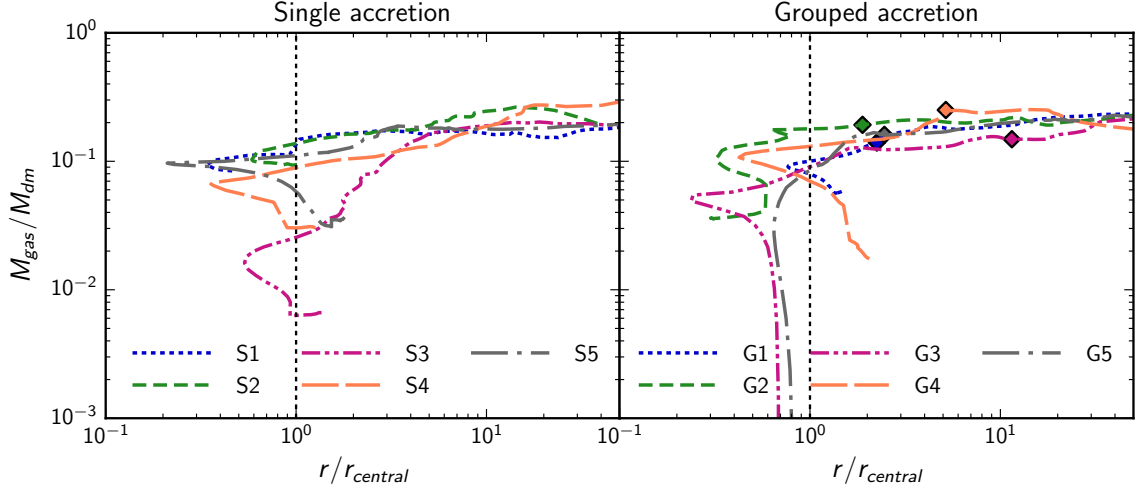


Figure 4.10: Ratio of gas mass to dark matter mass, as a function of distance from the main group. Colours and linestyles are the same as in Fig. 4.6. The data have been smoothed using a moving average of width 10.

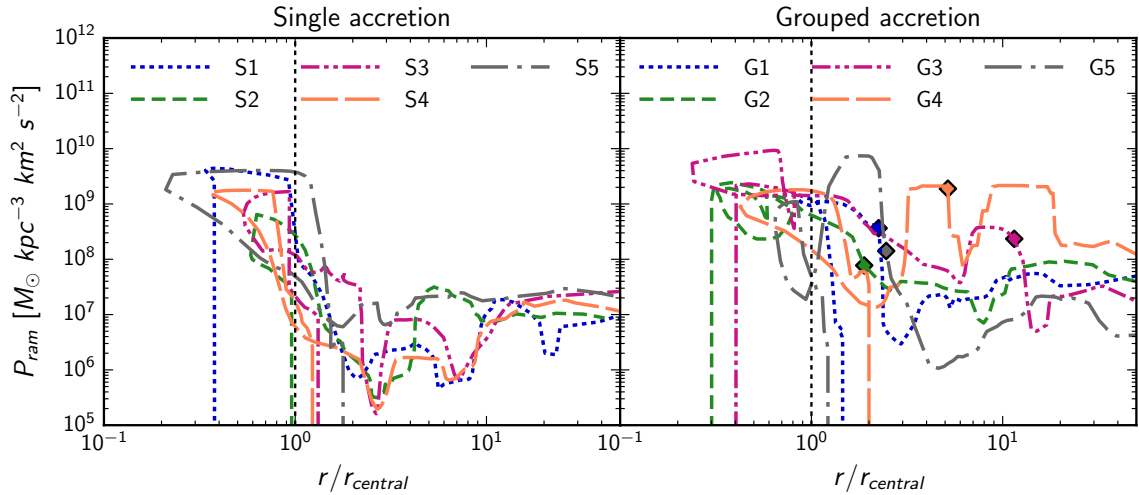


Figure 4.11: Ram pressure acting on each galaxy as a function of distance from the main group. Colours and linestyles are the same as in Fig. 4.6. The data have been smoothed using a moving average of width 10.

the galaxies' sSFRs are declining significantly and hence, star formation is not the dominant source of the decrease.

Another process that can preferentially remove gas from a galaxy without removing dark matter is ram pressure stripping. Fig. 4.11 shows the ram pressure experienced by the galaxies as they approach the group. We calculate ram pressure as

$$P_{\text{ram}} = \rho \bar{v}^2 \quad (4.5)$$

where ρ is the gas density within a 10 kpc wide shell outside the tidal radius of the galaxy and \bar{v} is the average velocity of the gas particles within this shell relative to the galaxy. For the single galaxies, ram pressure is significantly higher once they are within $(2 - 3)r_{\text{central}}$ of the group. This coincides with when they experience the highest decrease in gas fraction, suggesting that they are significantly affected by ram pressure due to the main group.

The grouped galaxies experience similar ram pressure as the single galaxies within r_{central} ; outside r_{central} , however, the ram pressure out to $\sim 3 - 5 r_{\text{central}}$ is higher than that experienced by the single galaxies, which is also when the grouped galaxies are within their external groups. However, these galaxies do not show a steeper decrease in gas fraction at the same time. In order for ram pressure to remove gas from a galaxy, it must overcome the gravitational force exerted by the galaxy. The galaxies in our grouped sample were all more massive than in our single sample at early times, which may explain why ram pressure was inefficient in removing gas mass from the grouped galaxies at that time.

Combining these results with those from Sections 4.3 and 4.4, we can infer the following:

- Tidal truncation plays the biggest role in the removal of mass from these galaxies. It does not affect the stellar mass of the galaxies, which is tightly bound near the centres of the galaxies. However, both the dark matter and gas components are affected significantly, as seen in Figs. 4.3, 4.6 and 4.7.
- The galaxies preferentially lose more gas mass than dark matter mass. While it is difficult to precisely determine how much of the gas lost is due to ram pressure stripping, the times when this decrease in gas to dark matter ratio is highest coincides with when the galaxies experience the highest ram pressure.

Therefore, ram pressure is at least an important mechanism for gas mass loss, though it is unclear if it is the dominant one.

4.6 Implications for galaxy properties

Finally, we show the consequences of these environmental processes on the final properties of our galaxy sample. In Fig. 4.12, we show the stellar fraction $M_{\text{star}}/M_{\text{tot}}$ versus M_{tot} for our galaxies, where M_{tot} is the value at the final redshift (top panel) and at z_{peak} (bottom panel), while M_{star} is always the value at the final redshift. In Fig. 4.12(a), unaccreted galaxies show a strong correlation between stellar fraction and total mass at the final redshift as expected. However, there is a clear difference between unaccreted, single and grouped galaxies. As we have shown in Figs. 4.6 and 4.7, as galaxies are accreted onto a group, they lose dark matter mass, but not stellar mass. This results in single galaxies of the same total mass having higher stellar fractions on average compared to unaccreted galaxies; grouped galaxies have even higher stellar fractions, nearly an order of magnitude higher than the unaccreted galaxies. Thus all three galaxy samples occupy distinct regions on this diagram. This is then a significant source of scatter for any stellar mass-halo mass relation that is derived without removing group/cluster galaxies, including backsplash galaxies, whether observationally, semi-analytically or through simulations.

Previous studies have suggested a strong correlation between the stellar mass and peak mass of galaxies (e.g. Peñarrubia et al., 2008; Smith et al., 2016). As we have found in this study, most of the single and grouped galaxies attained their peak total mass around the time they first became part of any group. Before accretion, their stellar fractions should evolve in the same way as that of unaccreted galaxies. In Fig. 4.12(b), we find that all three categories of galaxies adhere to a single trend in stellar fraction versus total mass at z_{peak} . In fact, this trend is nearly identical to the trend seen for unaccreted galaxies at $z = 0.4$, which indicates that there is indeed a strong correlation between current stellar mass and halo mass at z_{peak} .

We also investigated the relation between gas fraction and total mass. The gas fraction was well correlated with M_{tot} at both z_{peak} and the final redshift and there was no obvious separation between the three samples of galaxies. Observationally, the total mass of galaxies is often difficult to measure, making it challenging to compare our results to observations; the stellar and gas mass are more easily obtained, however.

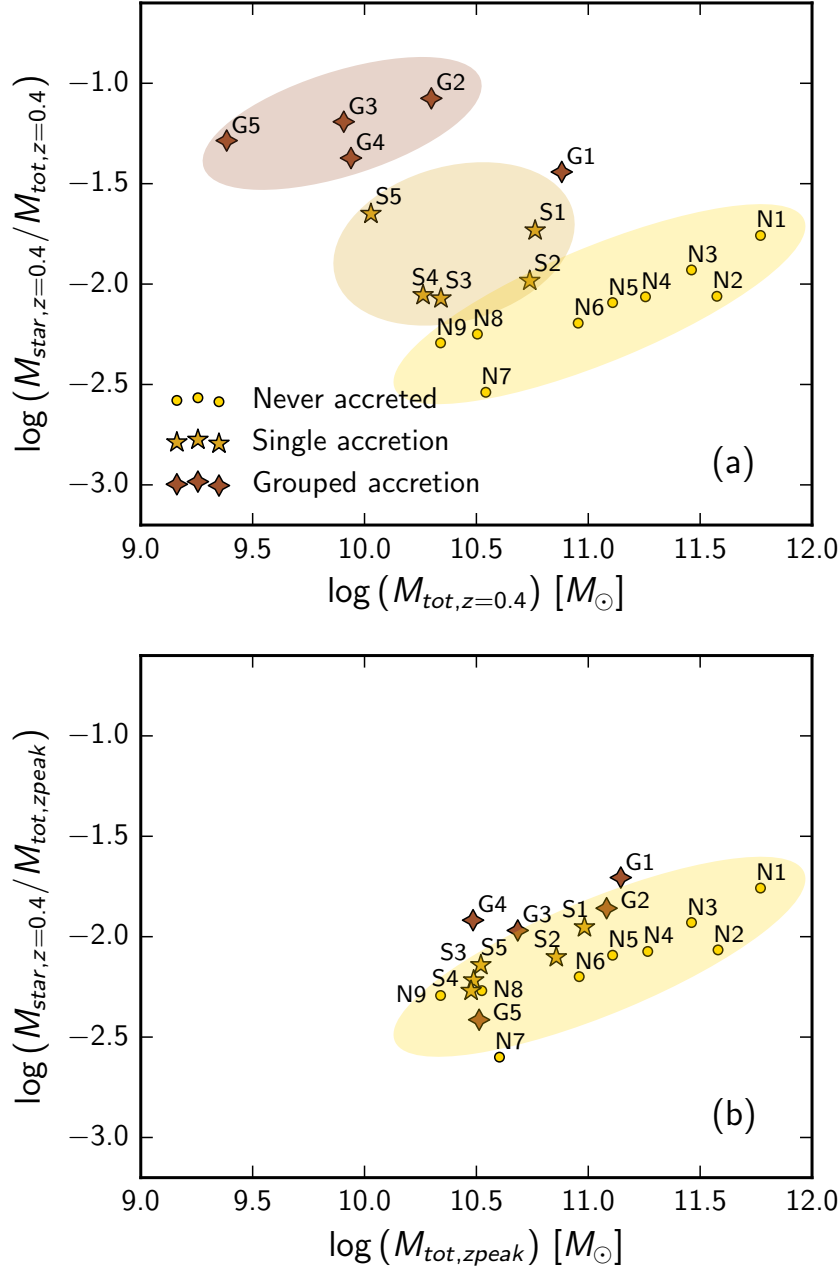


Figure 4.12: Stellar fraction w.r.t. total mass at the final redshift (top) and at z_{peak} (bottom) for galaxies in all three categories. The different colours and symbols are used to distinguish between the categories. Elliptical regions have been added in the top panel to approximately show the regions occupied by each category. The elliptical region in the bottom panel is identical to the one above for unaccreted galaxies. The figures show explicitly that the current stellar mass of the galaxies is better correlated with their peak total mass rather than present day mass.

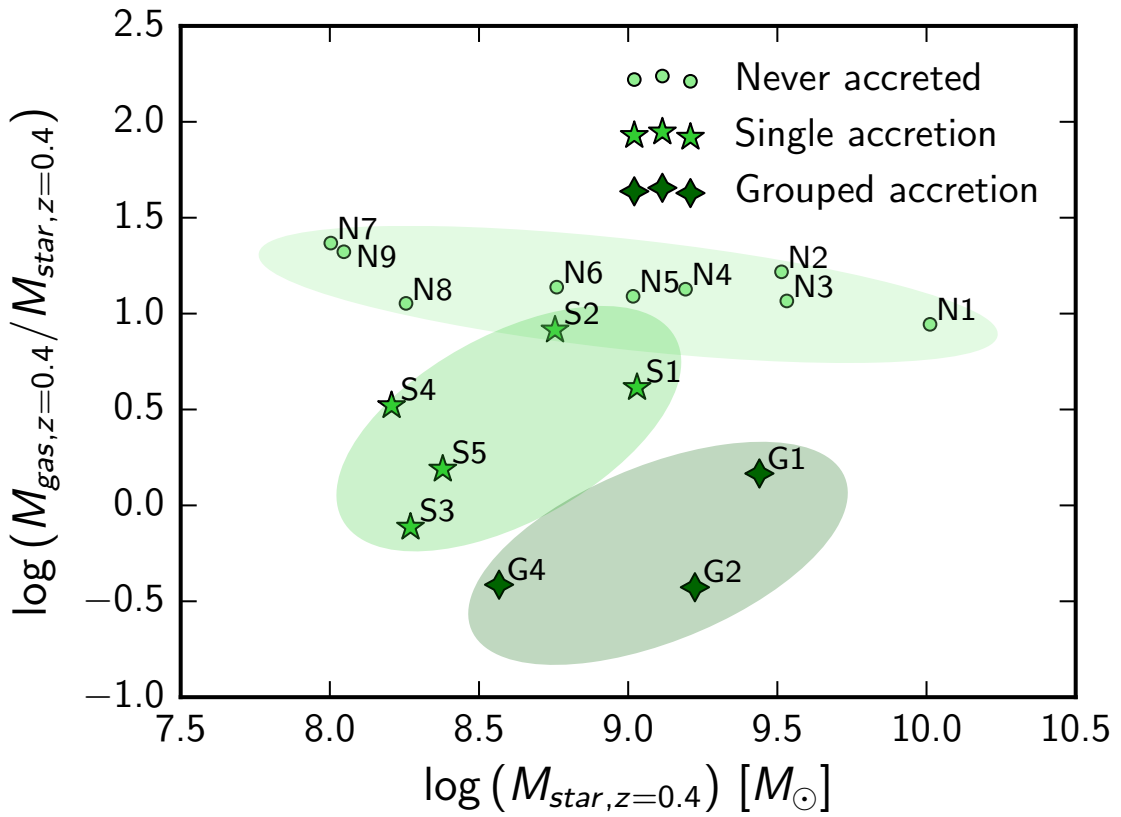


Figure 4.13: Gas fraction as a function of stellar mass at the final redshift for galaxies in all three categories. The different colours and symbols are used to distinguish between the categories. Elliptical regions have been added to approximately show the regions occupied by each category.

Therefore, in Fig. 4.13, we show the gas fraction w.r.t. stellar mass $M_{\text{gas}}/M_{\text{star}}$ as a function of M_{star} at the final redshift. Here again, the three samples of galaxies occupy distinct regions in this space, which shows that the gas fraction is significantly affected by environment.

4.7 Summary

We use a zoom-in hydrodynamical simulation of a galaxy group out to $3r_{\text{vir}}$ to study the mass loss histories of its member galaxies and the degree to which they have been preprocessed.

- Both singly-accreted and group-accreted galaxies lose considerable amounts of mass in dark matter and gas due to their accretion onto a group. The mass loss is primarily due to tidal truncation which does not affect the stellar content of the galaxies.
- Single and grouped galaxies both reach their peak total mass before becoming part of the main group. Single galaxies have a nearly constant mass in dark matter and gas after this peak, which can occur as far out as $(8-10)r_{\text{central}}$ from the group, until they begin losing mass just outside r_{central} . Grouped galaxies begin losing mass well outside r_{central} of the main group due to the external groups they are in. Due to this preprocessing, their total mass loss from peak to end is higher than that of single galaxies.
- Both single and grouped galaxies have gradually declining sSFRs as they approach the main group – following a delay of $\sim (0.5 - 2)$ Gyr after accretion onto the *main* group, we find evidence for rapid quenching for both samples of galaxies.
- In all cases, galaxies lose relatively more mass in gas than in dark matter and this cannot be accounted for with star formation alone. The higher mass loss in gas often coincides with high ram pressure experienced by the galaxies. Although we cannot determine precisely how much of an effect ram pressure stripping has on these galaxies, it appears to be an important mechanism for gas removal.
- The cumulative effect of this mass evolution is that at the final redshift, unaccreted, single and grouped galaxies occupy distinct regions on a SMHM relation.

In fact, preprocessed galaxies are likely to be an important source of scatter in any SMHM that does not exclude group and cluster galaxies. At peak mass, however, all three categories adhere to a single SMHM relation and therefore, peak masses can be reliably used to assign stellar masses to haloes in dark matter simulations, regardless of their accretion histories.

This study examines the mass loss of galaxies in a group environment and the role preprocessing plays in affecting mass loss and star formation. We look forward to expanding this study to more groups, in order to build a statistical understanding of galaxy evolution in groups. Our future work will focus not only on expanding our sample, but also extending this analysis to observable properties that can be directly compared to observations of galaxies in groups.

Acknowledgements

We thank the National Science and Engineering Research Council of Canada for their funding. Computations were performed on the *gpc* supercomputer at the SciNet HPC Consortium (Loken et al., 2010). SciNet is funded by the following: the Canada Foundation for Innovation under the auspices of Compute Canada; the Government of Ontario; Ontario Research Fund – Research Excellence; and the University of Toronto. This work was made possible by the facilities of the Shared Hierarchical Academic Research Computing Network (SHARCNET:www.sharcnet.ca) and Compute Canada.

References

- Abadi M. G., Moore B., Bower R. G., 1999, *MNRAS*, **308**, 947
- Angulo R. E., Lacey C. G., Baugh C. M., Frenk C. S., 2009, *MNRAS*, **399**, 983
- Bahé Y. M., McCarthy I. G., Balogh M. L., Font A. S., 2013, *MNRAS*, **430**, 3017
- Balogh M. L., Navarro J. F., Morris S. L., 2000, *ApJ*, **540**, 113
- Balogh M. L., Baldry I. K., Nichol R., Miller C., Bower R., Glazebrook K., 2004, *ApJ*, **615**, L101
- Balogh M. L., et al., 2016, *MNRAS*, **456**, 4364

- Barnes J. E., Hernquist L., 1992, *Nature*, **360**, 715
- Behroozi P. S., Wechsler R. H., Wu H.-Y., 2013a, *ApJ*, **762**, 109
- Behroozi P. S., Wechsler R. H., Wu H.-Y., Busha M. T., Klypin A. A., Primack J. R., 2013b, *ApJ*, **763**, 18
- Behroozi P. S., Wechsler R. H., Conroy C., 2013c, *ApJ*, **770**, 57
- Behroozi P. S., Wechsler R. H., Lu Y., Hahn O., Busha M. T., Klypin A., Primack J. R., 2014, *ApJ*, **787**, 156
- Blanton M. R., Eisenstein D., Hogg D. W., Schlegel D. J., Brinkmann J., 2005, *ApJ*, **629**, 143
- Bournaud F., Duc P.-A., Amram P., Combes F., Gach J.-L., 2004, *A&A*, **425**, 813
- Bryan G. L., Norman M. L., 1998, *ApJ*, **495**, 80
- Dressler A., 1980, *ApJ*, **236**, 351
- Gabor J. M., Davé R., 2015, *MNRAS*, **447**, 374
- Gunn J. E., Gott III J. R., 1972, *ApJ*, **176**, 1
- Hahn O., Abel T., 2013, MUSIC: MUlti-Scale Initial Conditions, Astrophysics Source Code Library (ascl:1311.011)
- Hogg D. W., et al., 2004, *ApJ*, **601**, L29
- Hou A., Parker L. C., Harris W. E., 2014, *MNRAS*, **442**, 406
- Jetley P., Gioachin F., Mendes C., Kale L. V., Quinn T., 2008, in Parallel and Distributed Processing, 2008. IPDPS 2008. IEEE International Symposium on. pp 1–12, doi:10.1109/IPDPS.2008.4536319
- Jetley P., Wesolowski L., Gioachin F., Kal L. V., Quinn T. R., 2010, in 2010 ACM/IEEE International Conference for High Performance Computing, Networking, Storage and Analysis. pp 1–11, doi:10.1109/SC.2010.49
- Joshi G. D., Parker L. C., Wadsley J., 2016, *MNRAS*, **462**, 761

- Joshi G. D., Wadsley J., Parker L. C., 2017, [MNRAS](#), **468**, 4625
- Kauffmann G., White S. D. M., Heckman T. M., Ménard B., Brinchmann J., Charlot S., Tremonti C., Brinkmann J., 2004, [MNRAS](#), **353**, 713
- Kawata D., Mulchaey J. S., 2008, [ApJ](#), **672**, L103
- Keller B. W., Wadsley J., Benincasa S. M., Couchman H. M. P., 2014, [MNRAS](#), **442**, 3013
- Knebe A., Power C., Gill S. P. D., Gibson B. K., 2006, [MNRAS](#), **368**, 741
- Knebe A., et al., 2011, [MNRAS](#), **415**, 2293
- Larson R. B., Tinsley B. M., Caldwell C. N., 1980, [ApJ](#), **237**, 692
- Loken C., et al., 2010, *Journal of Physics: Conference Series*, 256, 012026
- Madau P., Dickinson M., 2014, [ARA&A](#), **52**, 415
- Makino J., Hut P., 1997, [ApJ](#), **481**, 83
- McGee S. L., Balogh M. L., Bower R. G., Font A. S., McCarthy I. G., 2009, [MNRAS](#), **400**, 937
- Menon H., Wesolowski L., Zheng G., Jetley P., Kale L., Quinn T., Governato F., 2015, [Computational Astrophysics and Cosmology](#), **2**, 1
- Moore B., Katz N., Lake G., Dressler A., Oemler A., 1996, [Nature](#), **379**, 613
- Moore B., Lake G., Katz N., 1998, [ApJ](#), **495**, 139
- Oemler Jr. A., 1974, [ApJ](#), **194**, 1
- Oman K. A., Hudson M. J., 2016, [MNRAS](#), **463**, 3083
- Peñarrubia J., Navarro J. F., McConnachie A. W., 2008, [ApJ](#), **673**, 226
- Planck Collaboration et al., 2014, [A&A](#), **571**, A16
- Schawinski K., et al., 2014, [MNRAS](#), **440**, 889
- Smith R., Choi H., Lee J., Rhee J., Sanchez-Janssen R., Yi S. K., 2016, [ApJ](#), **833**, 109

Toomre A., Toomre J., 1972, [ApJ](#), **178**, 623

Wadsley J. W., Stadel J., Quinn T., 2004, [New A](#), **9**, 137

Wadsley J. W., Keller B. W., Quinn T. R., 2017, preprint, ([arXiv:1707.03824](#))

Wetzel A. R., Tinker J. L., Conroy C., van den Bosch F. C., 2013, [MNRAS](#), **432**, 336

Wetzel A. R., Deason A. J., Garrison-Kimmel S., 2015, [ApJ](#), **807**, 49

van den Bosch F. C., Jiang F., Campbell D., Behroozi P., 2016, [MNRAS](#), **455**, 158

CHAPTER 5

SUMMARY AND FUTURE WORK

5.1 Thesis summary

Dense environments have a significant impact on the evolution of galaxy populations that is not seen in field galaxies. In this thesis, we have studied the environmental impact of the galaxy group environment in terms of the mass loss experienced by their member galaxies and how galaxies are preprocessed in smaller groups before becoming part of their final host haloes.

In Chapter 2, we investigated the phenomenon of mass segregation, which is the establishment of a radial trend in average galaxy mass within groups and clusters, whereby galaxies closer to the group/cluster centres are more massive on average. The use of a dark matter cosmological simulation containing a large volume of the Universe provided us with a large sample of haloes with which to study this effect. In the absence of baryons, we first had to select from those haloes a sample of galaxy analogues that could potentially host single galaxies. The procedure outlined in Chapter 2 allowed us to explore the hierarchy of subhaloes generated by two halo finders, AHF and ROCKSTAR, and select a sample of galaxy analogues out to $3 r_{\text{vir}}$ from their host haloes. We showed that both AHF (which is a spherical overdensity algorithm that only considers spatial density) and (ROCKSTAR, which is a phase-space friends-of-friends algorithm) were able to detect nearly identical galaxy analogue samples outside $\sim 0.5 r_{\text{vir}}$ of the host halo. However, within $0.5 r_{\text{vir}}$, where the density of the host halo is high enough to mask the density of any substructure, the velocity information used by ROCKSTAR was crucial to detecting galaxy analogues. Using our sample of ROCKSTAR galaxy analogues, we showed that mass segregation was limited to within $\sim 0.5 r_{\text{vir}}$ of groups and clusters, with average analogue mass declining with increasing distance from the host halo centre, and that while the trends were statistically significant, they were also weak. Previous studies on mass segregation have either found no trend or weak trends with average mass decreasing with distance from the centre; our results are consistent with the latter.

In Chapter 3, we explored the mass loss experienced by our sample of galaxy analogues in different environments. We compared two samples, one selected based on their $z = 0$ masses which were very likely to have been affected by their environment, and one selected based on their peak mass, which has been shown to be more tightly correlated with stellar mass (e.g. Peñarrubia et al., 2008; Smith et al., 2016). Regardless of the mass definition used, we found a strong radial trend of mass loss whereby

galaxy analogues currently found closer to the host halo’s centre had lost relatively more of their peak mass than those found farther away. The trend was strong within r_{vir} , but weaker beyond this radius (although not insignificant). We also separated our sample into a ‘single’ subsample of galaxy analogues that had been distinct for their entire history before joining their final host halo, and a ‘grouped’ subsample that had been in a group (other than their current host) prior to joining their final host halo. This allowed us to directly study the effects of preprocessing.

We found that for galaxy analogues found close to the host’s centre ($\lesssim 0.2 r_{\text{vir}}$), the amount of mass loss was nearly equal for the single and grouped sample. However, as we went farther away from the host centre, the differences between the two samples got larger, at least out to the virial radius, such that grouped galaxy analogues had lost more mass than single ones. This showed that the grouped sample had been preprocessed in terms of halo mass loss. Further separating this mass loss into two stages, before and after the galaxy analogues first crossed within the host’s virial radius, provided a fuller picture. Grouped galaxy analogues had lost $\sim 25 - 35\%$ more mass than the single galaxy analogues, *before* joining the host. *After* joining the host, however, there was little difference between the single and grouped galaxy analogues found close to the virial radius of the host, but closer to the host, the single galaxy analogues had lost more mass since crossing. Thus, galaxy analogues in the grouped sample had been significantly preprocessed and had therefore experienced a large proportion of their total mass loss before joining their final host haloes. Galaxy analogues in the single sample, on the other hand, experienced most of their mass loss after joining their hosts, in essence ‘catching up’ with the mass loss of the grouped sample.

Chapters 2 and 3 allowed us to study the halo mass loss and segregation of galaxy analogues in dark matter simulations in a statistical manner. In Chapter 4, we expanded this investigation with a targeted study of one of the galaxy groups. We followed the individual histories of its member galaxies with the use of a zoom-in, fully hydrodynamical simulation. The dark matter, gas and stellar components of galaxies have distinct characteristic spatial distributions and dynamical properties. Following the fate of the each component separately enabled us to search for differential effects due to environment which could constrain the processes that are important in this regime. The group we simulated had a virial mass of $2.7 \times 10^{13} M_{\odot}$ at $z = 0$ and a virial radius of 788.6 kpc. We selected all galaxies within $3 r_{\text{vir}}$ of the group

centre at the final redshift and separated them into single and grouped galaxies as in Chapter 3; additionally, we also selected a control sample of ‘unaccreted’ galaxies that have always been distinct and never crossed within the virial radius of the group. We examined the properties of dark matter, gas and stars in the galaxies over cosmic time which showed that while the unaccreted galaxies continue growing in mass in all three components for their entire histories, the single and grouped galaxies either stop growing or begin losing mass in dark matter and gas after reaching a peak value at $z \sim 2$. Their stellar masses however keep growing, although at a lower rate for the grouped galaxies. We also studied the star formation histories of the galaxies and while all three subsamples showed a steady decline in sSFR with time, the rate of decline was higher for single galaxies compared to unaccreted galaxies and even higher for grouped galaxies after $z \sim 1.5$.

While these average trends indicate that the group has an influence on the single and grouped galaxies, studying the same properties as a function of the galaxies’ distance from the group allowed us to directly determine when and how its influence works. Individual tracks of single and grouped galaxies showed that both single and grouped galaxies reach their peak total mass outside the group, as far out as $\sim (8 - 10) r_{\text{vir}}$. While the single galaxies maintain this mass until just outside the group’s virial radius, the grouped galaxies begin losing mass around the time they first become part of a group (other than the main group). The individual tracks of sSFR suggest that there is evidence for rapid quenching of the galaxies some time after infall, which may be consistent with studies that propose a delay of $\sim (2 - 3)$ Gyr after infall before rapid quenching occurs (Wetzell et al., 2013; Schawinski et al., 2014; Balogh et al., 2016; Oman & Hudson, 2016). For our sample of galaxies, we found the range of delay times after infall to be $\sim (0.5 - 2)$ Gyr. The combined effect of these trends in mass loss is that unaccreted, single and grouped galaxies of equal total mass have significantly different stellar mass-to-halo mass (SMHM) relations at the final redshift of $z = 0.4$. However, at their peak total mass, all three categories have nearly identical SMHM values. These results suggest that the inclusion of preprocessed galaxies may be a key source of scatter when studying SMHM relations using a mix of galaxy populations.

5.2 Implications

The motivation for this thesis was to understand the role of the group environment on the evolution of galaxies. We specifically measured the amount of mass loss suffered by galaxy analogues and galaxies as they approach and are accreted into the group environment. In Chapter 2, we discussed the effects of dynamical friction in driving mass segregation. The weak trends found in that section led to the conclusion that dynamical friction may not be an important process in these systems. Moreover, the trends were nearly nonexistent when we excluded low mass galaxy analogues i.e. the more massive galaxy analogues did not preferentially gather near the centres of their host haloes, which implied that dynamical friction had not been efficient in driving them to the centres. However, Chapters 2 and 3 have shown that even within a low mass group, galaxies can lose a significant amount of mass. Since dynamical friction becomes less efficient with lower galaxy mass, it may be the case that the combined effects of dynamical friction and tidal mass loss can explain the weak segregation trends we found.

The question of what physical process is important and dominant in what environments is by no means a resolved issue. This work adds to this body of research by concentrating on the mass loss suffered by galaxies and the degree of preprocessing they experience. From Chapters 3 and 4, it appears that of the various environmental effects discussed in Section 1.3.2, tidal stripping is the dominant process in driving halo mass loss, although whether it can explain other effects such as star formation quenching and morphological transformation remains to be seen. More broadly, gravitational effects i.e. harassment, tidal stripping and mergers, appear to be the more dominant set of mechanisms affecting galaxies, with hydrodynamical processes i.e. ram pressure stripping and strangulation being a secondary force, at least in the case of low mass groups. Tidal stripping being the dominant process bears out in several different ways in our results. Tidal stripping results in the loss of dark matter and gas while leaving most of the stellar mass of the galaxies intact. It also explains why we do not see rapid quenching at accretion; the mass loss we see is gradual and outside-in, starting in the outskirts of the galaxy and making its way towards the centre. Therefore, star formation is not directly affected by it. What precisely causes the rapid quenching, $\sim (0.5 - 2)$ Gyr after accretion on to the main group, for nearly all our galaxies is yet to be determined.

A prominent theme through our investigations was the phenomenon of preprocessing. The different degrees of mass segregation in groups vs. clusters in Chapter 2 hinted that preprocessing may be important for degrading any trends that might have otherwise developed in cluster-sized haloes. In Chapters 3 and 4, we explicitly studied preprocessing in terms of halo mass loss and found that it is indeed an important process affecting galaxies well before they are accreted by their final group/cluster. This has significant implications for our understanding of environmental effects on galaxies. A large proportion of galaxies being accreted by groups and clusters have already been diverted from the path they would have taken had they been field galaxies, which means that we have to re-evaluate our initial assumptions when we measure the effects of the final group/cluster. Preprocessed galaxies can introduce significant biases in analysing the effect of cluster environments and preprocessing is not restricted to just the process of mass loss. This may significantly change our estimates of the efficiency of the various environmental processes, particularly in more massive clusters which are more likely to have a larger population of preprocessed galaxies.

This thesis was aimed at understanding the path of individual galaxies, which can only be done through simulations. The results we have obtained cannot be replicated through observations, i.e. we cannot directly observe mass loss or quenching occurring in galaxies. However, at each step, we have attempted to provide key galaxy properties that are a consequence of these processes so that they can be directly compared to observations. In particular, we have shown how the galaxies' stellar and gas masses as a fraction of their total mass are affected by the mass loss they experience. The SMHM relations were different for the unaccreted, single and grouped samples in Chapter 4, which suggests that the inclusion of preprocessed galaxies is one of the key sources of scatter in SMHM relations derived from galaxy samples that include group/cluster galaxies. The preferential loss of dark matter over stellar mass raises the SMHM values of singly-accreted galaxies compared to unaccreted galaxies, and due to preprocessing, group-accreted galaxies have higher SMHM values than either unaccreted or singly-accreted galaxies. Even if attempts have been made to exclude such galaxies, often group/cluster members are defined as being within the virial radius of the group/cluster, and we have shown that the influence of the group/cluster can extend well beyond the virial radius, as has also been found in previous studies (Balogh et al., 2000; von der Linden et al., 2010; Wetzel et al., 2012; Bahé et al., 2013). Moreover, observationally, the two population are not easy to separate. Therefore,

these disparate populations of preprocessed and single accretion, backplash and in-falling, galaxies may often be treated as one population when in fact the true picture is more complex. This work provides an explanation for some of the scatter seen in SMHM relations in other studies and a potential method to remove this scatter in future work.

5.3 Future directions

The question of what drives galaxy evolution is a broad and complicated one. This thesis has aimed at explaining one facet of this issue, but many others remain to be explored. Chapter 4 is our first step towards understanding galaxy evolution in groups, but we were limited to a sample of one group of galaxies. Whether this group is typical within its mass range, whether its merger history affected our results, are questions that remain unanswered. The next steps are to expand this study to more groups and perhaps even clusters, spanning a wider range in masses, dynamical states and merger histories. Ideally, this would be accomplished with a cosmological hydrodynamical simulation of a large volume at the same or better resolution. If this proves to be too computationally restrictive, then the next best thing would be to develop a suite of zoom-in simulations that span the range of group and cluster properties. We will then be able to explore the role of various group/cluster properties on the results presented in this thesis.

Mass loss is only one aspect of galaxy evolution. The methodology used in this work can be applied to also study properties such as stellar populations, gas properties and stellar and gas phase metallicities. Several questions may be asked regarding these properties. The stellar ages and mass distributions in different regions of the galaxies may shed light on whether environmental processes affect *where* star formation is occurring, which in turn may explain how gas is funnelled towards star forming regions in these environments and whether is it any different than what is seen for field galaxies. Similarly, stellar and gas phase metallicities may show what gas reservoir the galaxies are tapping into and whether there is any replenishment of the gas that has been stripped previously, perhaps on the outward-bound leg of the galaxies' trajectories. The answers to each of these questions takes us a step closer to fully understanding the evolution of galaxies in these environments.

Another avenue of exploration is the evolution of morphology. Mergers play an important role in shaping the morphology of galaxies even in the field. In groups and clusters, where mergers are more frequent, they will be especially important. Moreover, processes such as ram pressure stripping and tidal stripping may also affect morphology to some degree, e.g. by warping the discs of spiral galaxies, producing tidal tails etc. Tracking the morphologies of group and cluster galaxies and determining why they transform is another area of research that will determine what processes are important in these environments.

One important aspect of galaxy evolution we were not able to probe is AGN feedback. AGN feedback is not easy to implement in simulations since their immediate vicinity has to be very highly resolved, beyond the limits of most current simulations and since the effects of AGN are highly directional. While some simulations do implement AGN feedback (e.g. EAGLE (Crain et al., 2015; Schaye et al., 2015), ILLUSTRIS (Vogelsberger et al., 2014) and ROMULUS (Tremmel et al., 2017)), there is a lot more work to be done. AGN feedback is important for galaxies with halo masses of $\gtrsim 10^{12} M_{\odot}$, regardless of environment (e.g. Fabian, 2012; Dubois et al., 2013; Cicone et al., 2014; Le Brun et al., 2014; Keller et al., 2016). Our current sample of group galaxies contains a handful that are just at this critical mass, and therefore may be missing this important mechanism. In order to study a larger sample of galaxies that may include more massive galaxies, AGN feedback will be an important ingredient. Therefore, we look forward to implementing AGN feedback recipes and incorporating their effects into these results.

Finally, we must be able to compare the results from these simulations with observations. While we have attempted to study our galaxy sample using properties that are analogous to properties that can be observed, several properties such as luminosities, colours, morphologies, spectral line widths and the strength of emission lines are not directly comparable. While we can obtain these properties from our simulations, in the observed Universe, intervening matter between the galaxies and us serves to alter most of them. One way to truly compare simulation results and observations is to generate synthetic observations that mimic the effects of this intervening matter. Such synthetic observations will allow us to directly compare observed galaxies with simulated galaxies whose evolutionary histories are known and thereby help us to understand how observed galaxies evolve. Ultimately, such efforts will provide a more complete picture of galaxy evolution in dense environments.

References

- Bahé Y. M., McCarthy I. G., Balogh M. L., Font A. S., 2013, [MNRAS](#), **430**, 3017
- Balogh M. L., Navarro J. F., Morris S. L., 2000, [ApJ](#), **540**, 113
- Balogh M. L., et al., 2016, [MNRAS](#), **456**, 4364
- Cicone C., et al., 2014, [A&A](#), **562**, A21
- Crain R. A., et al., 2015, [MNRAS](#), **450**, 1937
- Dubois Y., Gavazzi R., Peirani S., Silk J., 2013, [MNRAS](#), **433**, 3297
- Fabian A. C., 2012, [ARA&A](#), **50**, 455
- Keller B. W., Wadsley J., Couchman H. M. P., 2016, [MNRAS](#), **463**, 1431
- Lares M., Lambas D. G., Sánchez A. G., 2004, [MNRAS](#), **352**, 501
- Le Brun A. M. C., McCarthy I. G., Schaye J., Ponman T. J., 2014, [MNRAS](#), **441**, 1270
- Oman K. A., Hudson M. J., 2016, [MNRAS](#), **463**, 3083
- Peñarrubia J., Navarro J. F., McConnachie A. W., 2008, [ApJ](#), **673**, 226
- Roberts I. D., Parker L. C., Joshi G. D., Evans F. A., 2015, [MNRAS](#), **448**, L1
- Schawinski K., et al., 2014, [MNRAS](#), **440**, 889
- Schaye J., et al., 2015, [MNRAS](#), **446**, 521
- Smith R., Choi H., Lee J., Rhee J., Sanchez-Janssen R., Yi S. K., 2016, [ApJ](#), **833**, 109
- Tremmel M., Karcher M., Governato F., Volonteri M., Quinn T. R., Pontzen A., Anderson L., Bellovary J., 2017, [MNRAS](#), **470**, 1121
- Vogelsberger M., et al., 2014, [MNRAS](#), **444**, 1518
- Wetzel A. R., Tinker J. L., Conroy C., 2012, [MNRAS](#), **424**, 232
- Wetzel A. R., Tinker J. L., Conroy C., van den Bosch F. C., 2013, [MNRAS](#), **432**, 336

Ziparo F., et al., 2013, [MNRAS](#), 434, 3089

van den Bosch F. C., Pasquali A., Yang X., Mo H. J., Weinmann S., McIntosh D. H., Aquino D., 2008, preprint, ([arXiv:0805.0002](#))

von der Linden A., Wild V., Kauffmann G., White S. D. M., Weinmann S., 2010, [MNRAS](#), 404, 1231